Identification and Evolution of Quantities of Interest for a Stochastic Process View of Complex Space System Development

by

GEORGE RALPH SONDECKER, IV

B.S. Mechanical Engineering
United States Air Force Academy, 2009

Submitted to the Department of Aeronautics and Astronautics
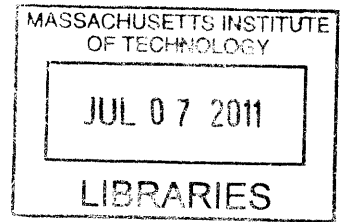in Partial Fulfillment of the Requirements for the Degree of

MASTER OF SCIENCE IN AERONAUTICS AND ASTRONAUTICS

at the

MASSACHUSETTS INSTITUTE OF TECHNOLOGY

June 2011

Signature of Author:
....

Department of Aeronautics and Astronautics
May 9, 2011

Certified by:
....

David W. Miller
Professor of Aeronautics and Astronautics
Thesis Supervisor

Accepted by:
....

Eytan H. Modiano
Associate Professor of Aeronautics and Astronautics
Chair, Committee on Graduate Students

Identification and Evolution of Quantities of Interest for a Stochastic Process View of Complex Space System Development

by

George Ralph Sondecker, IV

Submitted to the Department of Aeronautics and Astronautics
on May 9, 2011 in Partial Fulfillment of the
Requirements for the Degree of Master of Science in
Aeronautics and Astronautics

ABSTRACT

The objective of stochastic process design is to strategically identify, measure, and reduce sources of uncertainty to guide the development of complex systems. Fundamental to this design approach is the idea that system development is driven by measurable characteristics called quantities of interest. These quantities of interest collectively describe the state of system development and evolve as the system matures. This thesis provides context for the contributions of quantities of interest to a stochastic process view of complex system development using three space hardware development projects. The CASTOR satellite provides the opportunity for retrospective identification of quantities of interest and their evolution through time. As a complement to CASTOR, the preliminary design of the REXIS x-ray spectrometer provides the foundation for applying stochastic process approaches during the early phases of system development. Lastly, a spacecraft panel structural dynamics experiment is presented that illustrates analysis techniques commonly employed in stochastic process analysis.

Thesis Supervisor: David W. Miller

Title: Professor of Aeronautics and Astronautics

Acknowledgments

Table of Contents

List of Figures

List of Tables

Acronym and Notation List

ASIC- Application Specific Integrated Circuit

ASU- Arizona State University

CASTOR- Cathode Anode Satellite Thruster for Orbital Repositioning

CCD- Charge-Coupled Device

CCID- Charging Circuit Interrupting Device

CDR- Critical Design Review

CMM- Capability Maturity Model

CSA- Canadian Space Agency

CTI- Charge Transfer Inefficiency

DARPA- Defense Advanced Research Projects Agency

DCFT- Diverging Cusped Field Thruster

EAPS- MIT Earth, Atmospheric and Planetary Science Department

ETU- Engineering Test Unit

FC- Fully Coded

FNF- First Natural Frequency

FOV- Field of View

FTE- Full Time Equivalent

FWHM- Full Width Half Maximum

FWZI- Full Width Zero Intensity

GFY- Government Fiscal Year

GSFC- Goddard Space Flight Center

ISO9000- Quality assurance system developed by the International Organization for Standardization

IAP- Individual Activities Period; the month of January on the MIT academic calendar

LMCO- Lockheed Martin Corporation

META- Derived from the term "meta-representation," or "a detailed system design at varying levels of abstraction enabling the system to be verified independently of its physical manifestation" [1].

MPPT- Maximum Peak Power Tracker

MMPDS-03- *Metallic Materials Properties Development and Standardization* [16]

NEO- Near-Earth Object

OSIRIS-REx- O-Origins, SI-Spectral Interpretation, RI-Resource Identification, S-Security, REx-Regolith Explorer

PDR- Preliminary Design Review

PPU- Power Propulsion Unit

QoI- Quantity of Interest

RA- Research Assistant

RAND- Research and Development Corporation

REXIS- Regolith X-ray Imaging Spectrometer

S/C- Spacecraft

SPC- Single Point Constraint

SSL- MIT Space Systems Lab

UNP- University Nanosatellite Program

XFS- Xenon Feed System

Chapter 1 - Introduction

1.1 Motivation

"While the complexity of aerospace and defense systems has grown considerably over the past half-century, the systems engineering approach is little changed since its inception... as the duration and cost of system development has experienced rapid super-linear growth."

-DARPA in the META-II BAA [1]

The systems engineering process as it currently exists shares its origins in the development of early space and missile technologies during the mid-1900's. Since this time, the complexity of aerospace and defense technologies has grown tremendously as modern systems require enhanced capability, multi-mode functionality, and pinpoint accuracy while remaining unperturbed by threats of expanding diversity. As system complexity grows, a disturbing trend in the increasing frequency and magnitude of cost and schedule overruns has also emerged [2].

As cost and schedule pressures threaten to terminate the acquisition of the next generation of defense and aerospace projects, innovative approaches are needed to improve the design and development of complex systems. Stochastic process decision methods offer a radically different approach to managing system development. Fundamental to the stochastic process view of system development is that uncertainty is the greatest threat to achieving program objectives. Uncertainty is captured by identifying and measuring Quantities of Interest or QoIs.

QoIs evolve with the system and may include requirements, performance parameters, and key system traits. Once QoIs are defined, stochastic processes and Bayesian methods are employed to estimate the overall state of system development. This knowledge enables technology developers to identify and strategically reduce the greatest contributors of uncertainty, thereby achieving improved cost and schedule performance.

1.2 Objectives

The objective of this thesis is to provide a basis for the application and test of stochastic process decision methods on real systems. This objective is accomplished by defining QoIs from a stochastic process view of system development, identifying QoIs and performing basic uncertainty analysis, and tracking the evolution of QoIs through the development of three real systems. The systems under consideration are of varying complexity and maturity in order to establish a diverse collection of test cases for evaluating stochastic process approaches to system development.

A secondary objective of this thesis is to document the design, analysis, and results of three space hardware development projects. Discussion of the Cathode Anode Satellite Thruster for Orbital Repositioning (CASTOR) documents the historical development of a student-built satellite for reference by future student satellite programs. Likewise, the preliminary design of the Regolith X-ray Imaging Spectrometer (REXIS) is provided to form the foundation for detailed design and analysis. Lastly, a structural dynamics experiment is presented to evaluate the accuracy of various techniques for modeling rigid component attachment to a spacecraft structural panel.

1.3 Approach

The organization of this thesis is derived from the three projects that form test cases for stochastic process analysis. The diagram in Figure 1-1 provides the context for this thesis relative to the development of stochastic process decision approaches. The mathematical foundations for the stochastic process approaches are rooted in estimation and information theory. While a brief introduction is provided in Chapter 2, this theory and the stochastic approaches are largely beyond the scope of this thesis. Instead, this thesis focuses on identifying and tracking the QoIs in the system development projects identified in the red boxes below:
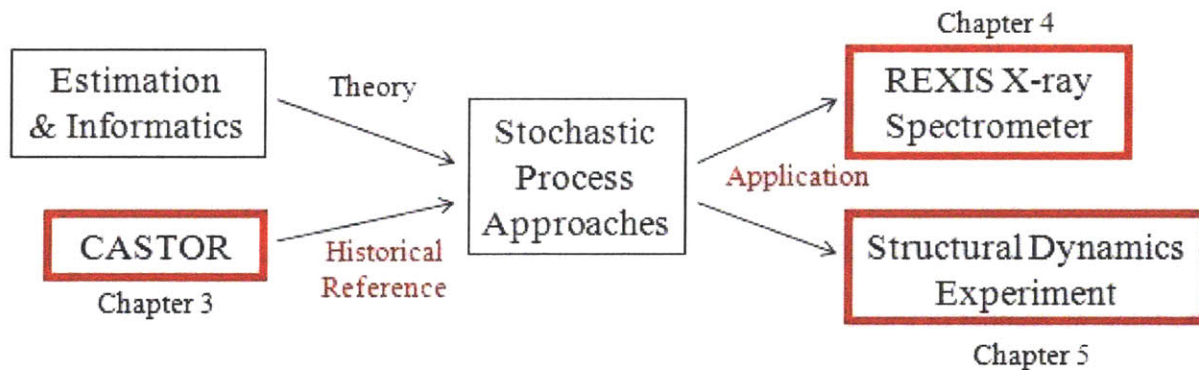
Figure 1-1: Thesis Contributions (red, **bold**) within the Context of Developing Stochastic Process Decision Approaches for Complex Systems

Identification and evolution of the QoIs driving the design of the three systems presented in this thesis provide a basis for applying stochastic processes at varying phases of system maturity. The first system to be presented is the CASTOR satellite discussed in Chapter 3. CASTOR is a mature, ongoing satellite project that has maintained extensive historical documentation pertaining to the satellite's design, analysis, simulation, and test. The QoIs driving CASTOR performance are identified and their evolution is tracked with historical context. This information enables stochastic processes to be applied retrospectively to assess the state of CASTOR development and identify sources of uncertainty throughout various design phases.

Furthermore, because CASTOR is an ongoing project, the satellite presents the opportunity to measure QoIs, invest resources according to model outputs, and observe the resulting outcome on satellite development.

The second system analyzed is the REXIS x-ray spectrometer discussed in Chapter 4. REXIS is the student collaboration experiment on the OSIRIS-REx asteroid sample return mission. REXIS is in the preliminary design phase of system development. As a new program, REXIS provides the unique opportunity to test and evaluate stochastic process decision approaches throughout all phases of system development. This thesis identifies REXIS QoIs to establish a foundation for future stochastic process analyses.

Lastly, a structural dynamics experiment performed in conjunction with the United States Air Force Academy's FalconSAT program is presented in Chapter 5. The purpose of this experiment is to conduct a trade study that explores the accuracy of various modal analysis techniques as applied to a component mounted on the center of a spacecraft panel. The analytical techniques employed in this study illustrate statistical assessment tools commonly used to evaluate the impact of QoIs on system performance.

Chapter 2 - Background

The field of systems engineering first originated at Bell Laboratories during the early 1940's as an outgrowth of technology development during World War II. In 1946, the U.S. Air Force founded the Research and Development (RAND) Corporation. RAND created the field of systems analysis which was applied extensively in the development of missiles and missile defense systems [3]. In 1950, the first documented course in systems engineering was taught by G.W. Gilman. Gilman was the director of systems engineering at Bell Laboratories and he taught the course at the Massachusetts Institute of Technology [4].

The process that emerged by the 1960's and came to be known as the systems engineering process generally involves identifying user needs, translating needs to requirements, conducting trade studies, performing analysis, integration and test, and verification and validation [5]. Using this framework, the field of systems engineering has enabled humans to organize engineering effort across many disciplines to create systems of enormous complexity. These innovations and the growth of complexity have not been accompanied by a corresponding improvement in systems engineering processes for managing complexity. In an effort to fill this void, stochastic processes offer an alternative approach to complex system development. This chapter provides an introduction to the stochastic process view of system development and presents QoIs as the elementary basis for enabling stochastic process analysis.

2.1 The Stochastic Process View of System Development

The stochastic process view of system development is a radically different approach to the design, integration, and verification of complex systems. Figure 2-1 illustrates the stochastic process approach to system development. At the core of Figure 2-1 is the system development cycle. The cycle is initiated with the definition of system requirements at the outset of a new project. The system then enters a period of design, analysis, and test where models are developed and experiments are performed. Throughout system development, QoIs are measured and uncertainties are calculated using Bayesian estimation tools. This information informs an estimate of system state and enables system developers to identify the sources of uncertainty that most adversely affect system development. Resources such as funding and research effort are then strategically invested to reduce those uncertainties [6]. This approach to system development enables technology developers to efficiently converge on a design that satisfies requirements and achieve improved budget and schedule performance.
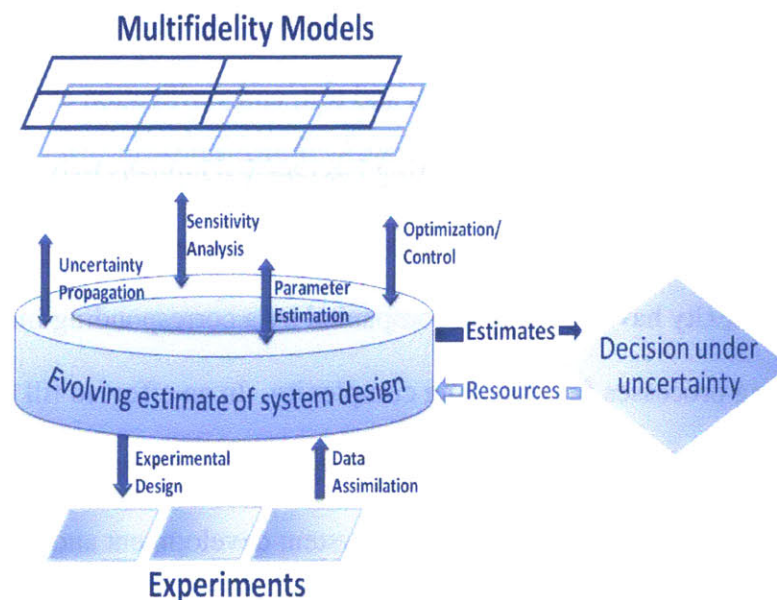
Figure 2-1: A Stochastic Process View of Complex System Development [6]

20

2.2 System State and Quantities of Interest

Fundamental to the stochastic process approach to complex system development is the idea of system state. System state describes the condition of the system at a given point in time and evolves as the design matures. System state is defined through the collective contributions of quantities of interest or QoIs. QoIs are measurable characteristics of the system that drive system performance. Like system state, QoIs evolve with the system and are defined from requirements, performance parameters, and key system traits. Example QoIs include power produced by a spacecraft's solar panels or yield strength of a material.

Stochastic processes and Bayesian estimation methods are used to estimate system state and its uncertainty. At the beginning of system development, the uncertainty of system state is very high as the details of the final design are largely unknown. Component specifications and theoretical calculations serve as the basis for estimating uncertainty during the early phases of system development. As the design matures, uncertainty is reduced as experimental data and models of increasing fidelity provide an enhanced estimate of system state.

2.3 Summary

As systems continue to grow in complexity, innovative solutions are needed to guide system development. Applying stochastic processes to system development provides a radically different approach to the conventional systems engineering process. The underlying objective behind the stochastic process view of system development is to quantitatively estimate and evolve system state through the use of performance-driving QoIs. By strategically reducing the uncertainty of system state, technology developers are able to better guide system development to meet requirements and achieve budget and schedule objectives.

Chapter 3 - CASTOR Development and QoIs

The CASTOR satellite is the most mature and complex system analyzed in this thesis. The tracking of CASTOR QoIs provides a retrospective view of system development that is useful for testing stochastic process decision methods. This chapter documents the historical development of the CASTOR satellite, identifies CASTOR QoIs and their evolution, and provides an illustration of how uncertainty is reduced through testing.

3.1 Chronological Development of the CASTOR Satellite

The CASTOR mission is to characterize the on-orbit performance of the Diverging Cusped Field Thruster (DCFT) developed by the MIT Space Propulsion Laboratory. The DCFT is an electric propulsion system similar in performance to existing Hall-effect thrusters but with the advantages of (1) lower power consumption, (2) longer lifetime, and (3) the thruster's ability to operate over a wide range of power levels. The CASTOR mission objective is to measure the thruster's power and xenon consumption and compare on-orbit thrust and efficiency data to measurements obtained in a vacuum chamber. This information will expand the existing body of knowledge of electric propulsion in two areas. First, it will contribute to the currently limited collection of data on the orbital performance of Hall effect thrusters. Second, this mission will serve as a valuable plasma physics experiment by allowing scientists to characterize the interaction between the plasma generated by the DCFT with Earth's ionosphere and magnetic field.

CASTOR was a competitor in the sixth University Nanosatellite Program (UNP-6) sponsored by the Air Force Office of Scientific Research. The satellite's development has been a student-led initiative intended to provide future engineers with a hands-on experience developing space hardware. MIT undergraduate and graduate students have contributed to all aspects of the satellite's design, fabrication, assembly, and test. CASTOR is a good candidate for testing stochastic processes because the satellite is a mature design that was developed almost exclusively at MIT. Many of the students who designed the satellite are still at MIT to answer questions about the project's evolution and to provide historical context regarding the rationale for key design decisions. Furthermore, satellite development is not yet complete. Ongoing testing and analysis enables QoIs to be measured in real time. As a student-built satellite, CASTOR provides a low-risk opportunity for assessing the utility of stochastic processes as resources can be invested to reduce uncertainty and the resulting effects on system state can be observed.

CASTOR development began in fall 2008 with the objective of becoming the first student-built satellite to reach the moon. Figure 3-1 shows the first engineering test unit (ETU-1) that was built and tested to qualification levels for both vibration and thermal vacuum. Prototypes were also manufactured for the satellite's avionics. After a number of initial testing failures, the team determined that the requirements necessary to reach the moon were too ambitious given financial constraints and the three-year development time allotted by the University Nanosatellite Program. In spring 2009, the new CASTOR mission became to operate the thruster in space for 1,500 hours or longer. This requirement was established to demonstrate the thruster's endurance capability, and because 1,500 hours is the duration of testing performed by comparable Hall-effect thrusters.
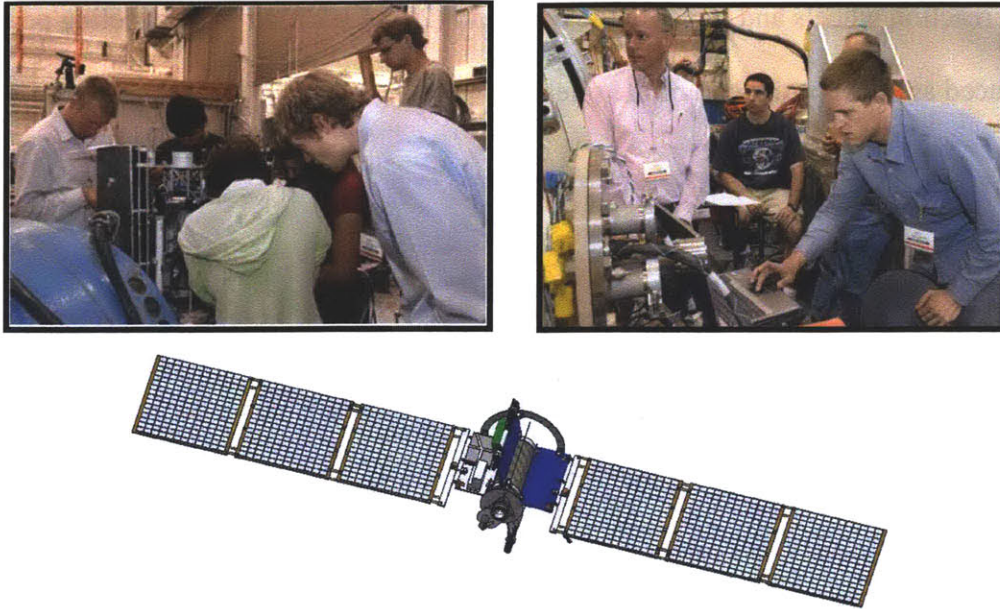
Figure 3-1: MIT Students Performing Environmental Testing (TOP) on the Initial CASTOR Design for Reaching the Moon (BOTTOM)

Despite the change in mission scope, feedback from the UNP Preliminary Design Review (PDR) instructed the team to significantly reduce the complexity of its satellite. In particular, UNP judges were concerned about the risk introduced by the satellite's tri-fold deployable solar panels and pressure vessels. In response, the CASTOR satellite underwent an extensive redesign. As shown in Figure 3-2, the sun-tracking, tri-fold solar arrays were replaced with single-panel deployable arrays. This change in configuration meant that the thruster could no longer be operated continuously and would instead be operated only during periods of sunlight. In addition, the pressure in the thruster's xenon tank was reduced from 4500psi to 3000psi to increase the factor of safety. The reduction in pressure resulted in a decrease in thruster operation time from 1,500 hours to 1,000 hours. Lastly, the attitude control system underwent a major redesign after a student-built simulation of the satellite indicated that the cold-gas control system would be depleted within two days of on-orbit operations due to a dipole induced by the DCFT's permanent magnet. This discovery led to (1) the replacement of the cold-gas system

with three reaction wheels and three torque coils and (2) the addition of a canceling permanent magnet placed at the opposite end of the satellite.
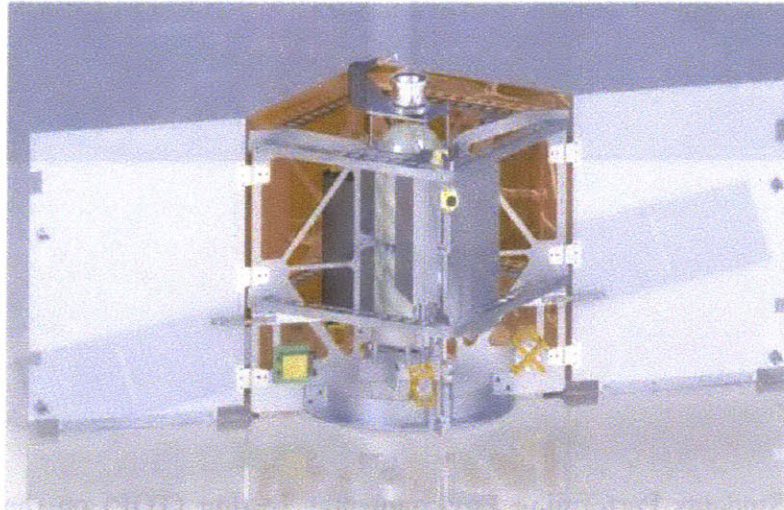
Figure 3-2: CASTOR Satellite in its Deployed Configuration

A second engineering test unit (ETU-2) was built and tested. The reduced complexity and experience from ETU-1 enabled the team to perform considerably better in its second series of environmental tests, but the results did not satisfy the stringent UNP requirements. At the CASTOR Critical Design Review (CDR) in spring 2011, the judges expressed concern about the structural integrity of the student-built composite panels as well as continued anxiety over the xenon pressure vessel. In response, an ISO9000-certified vendor was identified to professionally manufacture the composite panels, and tank pressure was reduced from 3000 psi to 1800 psi. Another change was the addition of a Xenon Feed System (XFS) developed by the NASA-Glenn Research Center. Replacing the student plumbing design with the NASA XFS offered both reduced risk and the ability to throttle the xenon flow rate to the DCFT. The CASTOR design was modified accordingly until NASA reneged on its offer due to funding shortages prior to the Proto-Qualification Review in summer 2010.

In response to this setback, the team reverted to its initial feed system design and built the third engineering test unit (ETU-3). This model was essentially a fully integrated satellite complete with avionics, wiring harness, and a demonstration plumbing system. Only costly flight components such as reaction wheels were replaced with mass simulators. The team took this model to the Proto-Qualification Review where it was once again criticized for its pressure vessel. This resulted in a re-evaluation of the CASTOR team's objectives.

It had been evident since the Preliminary Design Review that the objective of operating the thruster for 1500 hours would not be achievable. The CASTOR team's strategy was to maintain tank pressure as high as UNP would permit to demonstrate the thruster's on-orbit endurance capability. The mandate following the Proto-Qualification Review to further reduce pressure led the CASTOR team to abandon the endurance objective and pursue a modified mission. The revised mission objective required that the thruster be operated only enough to fully characterize its performance in space. Given this mission objective, a requirement of 600 psi was established as the new tank pressure. The CASTOR team presented this design at the UNP Flight Competition Review in January 2011 where the CASTOR satellite was not selected.

Going forward, the CASTOR program is continuing integration, test, and analysis efforts under the assumption that an alternative launch opportunity will arise. Should CASTOR obtain a launch, the satellite will likely experience a relaxation in several of the stringent UNP requirements, but any introduction of new requirements may also require redesign.

3.2 Identification of CASTOR QoIs

As presented in this section, the data and discussion pertaining to the CASTOR satellite

provide an illustration of a procedure for identifying and organizing QoIs in preparation for

analysis using stochastic process decision methods. This section identifies the top-level QoIs

that drove the CASTOR design throughout the satellite's development. The QoIs for the

subsystems that most substantially influenced the CASTOR design are analyzed in detail. These

subsystems are the propulsion and power subsystems. The QoIs for these subsystems are tracked

since CASTOR's inception in fall 2009, and N-squared diagrams are used to illustrate the

interactions between detailed subsystem QoIs.

The QoIs in Table 3-1 are organized according to the eight subsystems that comprise the

CASTOR satellite. While this list is not entirely exhaustive, these QoIs are the most substantial,

top-level drivers of system performance, and neglecting any of these QoIs would result in an

incomplete system definition. Identifying all of the QoIs of a complex system is an arduous, if

not impossible task. As an initial effort to identify top-level QoIs, the subsystem team leaders

who contributed to the CASTOR design were interviewed. The stochastic process approach to

system development was briefly explained to each subsystem leader, and the leaders were asked

to identify the requirements and general performance characteristics that most strongly drove the

design of their subsystem. The QoIs identified through these interviews are summarized in

Table 3-1.

Table 3-1: CASTOR Quantities of Interest

Subsystem	Quantities of Interest
Systems	Hardware Cost ($), Schedule (months), Number of Requirements (#)
Propulsion	Tank Pressure (psi), Thruster Operating Time (hr)
Structures	Mass (kg), Dimensions (cm x cm x cm)
Thermal	Min and Max Component Temperatures (K)
Power	Production (W), Consumption (W)
Avionics	Data Storage (MB), Processor Utilization (%)
Communications	Data Rate (bps), Equivalent Isotropically Radiated Power (dBm)
ACS	Control Torque (Nm), Momentum Storage Capacity (Nms), Knowledge and Pointing Accuracy (deg)

Applying stochastic approaches to the entire CASTOR satellite is beyond the scope of preliminary testing objectives. For this reason, the two subsystems that most substantially influenced satellite design throughout system development are selected for detailed study. These two subsystems are the propulsion and power subsystems. The requirements for these subsystems presented a persistent challenge to the student engineers who designed CASTOR. These challenges were primarily derived from the clash between ambitious science objectives and highly-conservative UNP design requirements. Specifically, the desire to operate the thruster for extended durations at high power levels was checked by mass and volume requirements that imposed practical limitations on the size of solar panels.

The evolution of the CASTOR propulsion QoIs is summarized in Figure 3-3. During fall 2008 (label A in Figure 3-3) the CASTOR satellite team determined that a lunar mission was infeasible given the limited time and funding allocated by the UNP-6 program. The new mission

objective became to operate the thruster for 1500 hours to match the performance of competing electric thrusters. During the spring and summer of 2009 (B), tank pressure was reduced in response to PDR feedback instructing the team to reduce risk. The requirement to achieve 1,500 hours of operation was no long possible at the lower pressure level, and the new requirement became to measure thruster degradation. In spring 2010 (C), CDR feedback encouraged additional risk reduction by lowering tank pressure even further. Lastly, during fall 2010 (D), the CASTOR team determined that at 1800psi, the mission to measure thruster degradation was compromised as degradation at 600 hours of operation would be insubstantial and difficult to conclusively measure. The new requirement became to minimally characterize DCFT operation in space, which resulted in a required tank pressure of 600psi.

Tank Pressure and Thruster Operating Time

QoI	FA '08	SP '09	FA '09	IAP '10	SP '10	FA '10	IAP '10
Tank Press:	4500 PSI	4500 PSI	3000 PSI	3000 PSI	3000 PSI	1800 PSI	600 PSI
Hours of Op:	4000 Hr	1500 Hr	1000 Hr	1000 Hr	1000 Hr	600 Hr	200 Hr
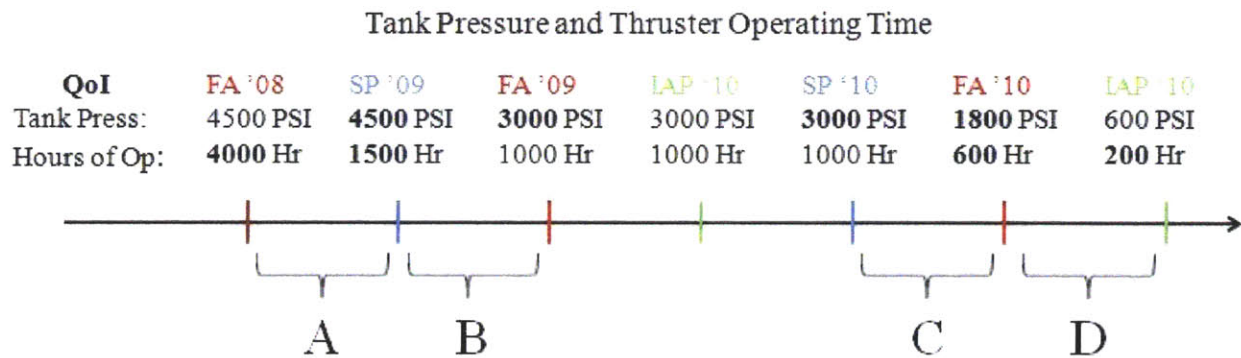
Figure 3-3: Evolution of CASTOR Propulsion QoIs

Similarly, the evolution of the CASTOR power QoIs are shown in Figure 3-4. During summer 2009 (A), PDR feedback to reduce risk resulted in a structural redesign. The new design eliminated the tri-fold, sun-tracking solar panels and reduced solar panel area. During the 2010 Individual Activities Period (IAP) (B), the thruster operation requirement is modified to enable thruster characterization at various power levels ranging from 40W to 300W. In spring 2010 (C), a higher fidelity model describing solar panel area identifies a slight reduction in available

surface area. Lastly, during fall 2010 (D), thruster testing reveals that the minimum threshold for thruster operation is 50W, not 40W.

Total Power Production and Thruster Cathode Consumption

QoI	FA '08	SP '09	FA '09	IAP '10	SP '10	FA '10	IAP '10
Produce:	290 W	290 W	169 W	169 W	169 W	165.1 W	165.1 W
Consume:	162.5 W	162.5 W	100 W	100 W	40-300 W	40-300 W	50-300 W

A   B   C   D
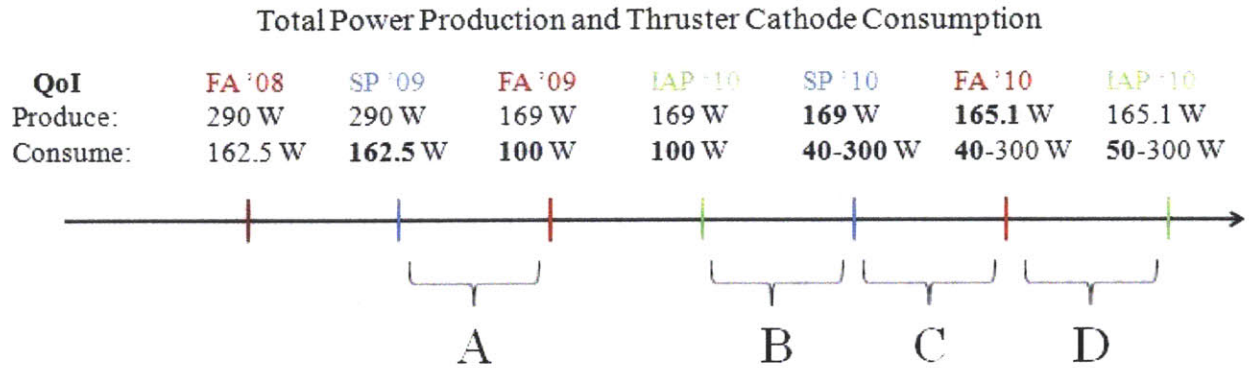
Figure 3-4: Evolution of CASTOR Power QoIs

Once top-level QoIs are identified for the overall system, N-squared diagrams provide an efficient means for organizing lower-level subsystem QoIs and identifying relationships between subsystem components. The N-squared diagram in Figure 3-5 demonstrates the linkages between the power and propulsion subsystems at the end of IAP 2010. The external input of solar flux in the top left of the diagram progresses through the system to produce the external output of thrust in the bottom right.

Within the N-squared diagram, the internal components required to convert solar flux into thrust are listed along the diagonal. The terms off the diagonal are QoIs. A QoI listed to the *right* of a component is a component output. Likewise, a QoI listed *above* a component is an input. As an example, consider the QoI of 165W in the top left of Figure 3-5. This QoI is an output of the solar panels and is an input to the Maximum Peak Power Tracker or MPPT. A detailed description of the individual components in Figure 3-5 is provided in Appendix A, and the corresponding uncertainty for each of the QoIs in Figure 3-5 is provided in Figure 3-6.

31

Solar Flux
1367W/m²

Xenon Gas
600 psi

Solar Panels	165W						
	MPPT	153W (24V)					
		PPU			8.2W (15V)	18.8W (500mA)	100W (200V)
			Tank	600psi			
				Regulator	15psi		
					Flow Cntrls	1 sccm	9 sccm
						Cathode	
							Anode

→ Thrust 7mN
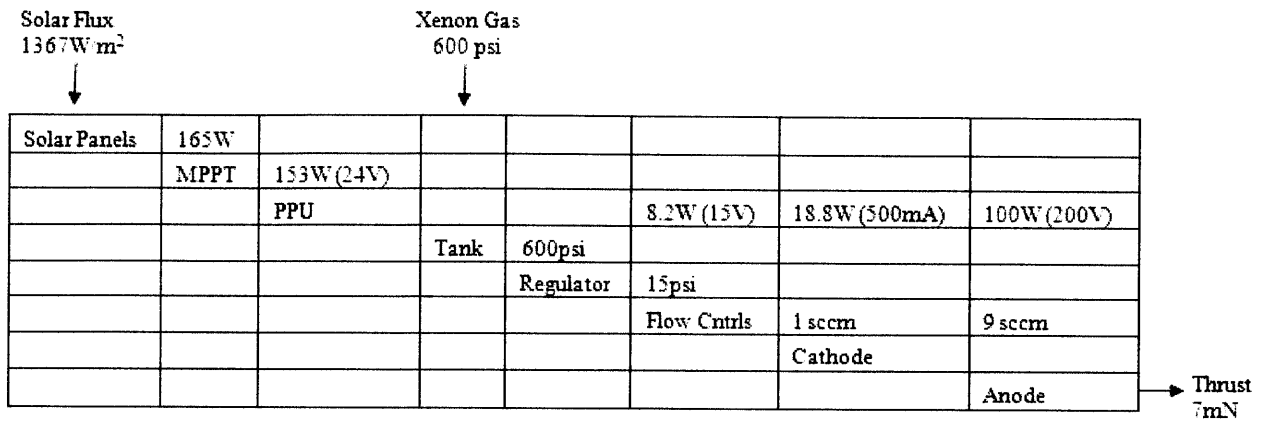
Figure 3-5: N-Squared Diagram Demonstrating Relations Between the Power and Propulsion Subsystems

Solar Flux
±3.4% (W/m²)

Xenon Gas
±1% (psi)

Solar Panels	-50% (W)						
	MPPT	-16.7%, -50% (V)					
		PPU			±1% (V)	±5% (mA)	±4% (V)
			Tank	±3% (psi)			
				Regulator	±10% (psi)		
					Flow Cntrls	±1.5% (sccm)	±1.5% (sccm)
						Cathode	
							Anode

→ Thrust -30% (mN)
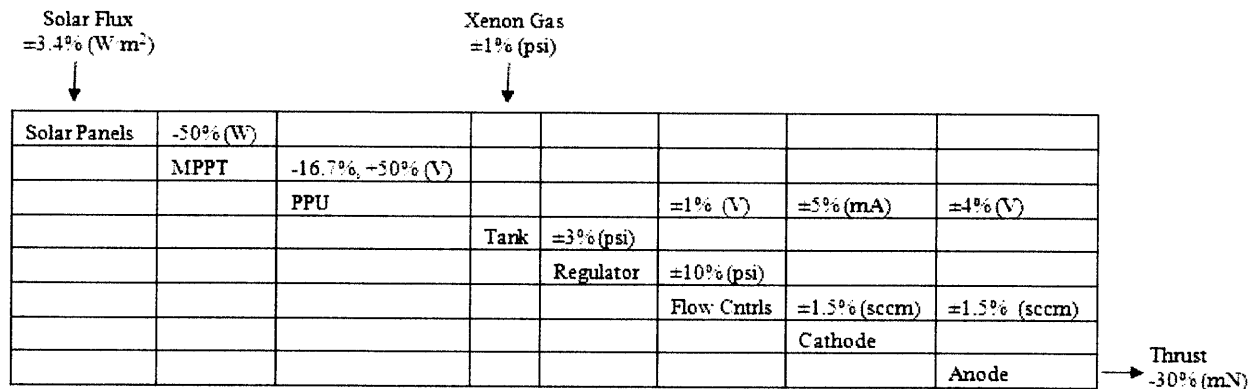
Figure 3-6: N-Squared Diagram Containing the Uncertainties of QoIs Identified in Figure 3-5

3.3 Illustration of QoI Uncertainty Reduction through Testing

This section illustrates how uncertainty is reduced through testing and provides an example of how Bayesian methods are employed to estimate QoI and system uncertainties. Bayesian methods enable QoI estimates to be combined and updated by taking into account multiple sources of data. Using the updated QoI estimates, the uncertainty of the system is quantified using entropy as a metric.

To begin, CASTOR subsystem QoIs were identified and measured both before and after testing. These subsystem QoIs are more detailed than the system-level QoIs discussed in Section 3.2. Subsystem leaders were asked to identify upcoming tests and the QoIs to be measured in those tests. QoI estimates were developed prior to testing using knowledge from previous tests, hand calculations, simulations, and vendor specifications. Following each test, the subsystem leaders reported the values of the QoIs they measured as well as the error of the measurement. The results of this survey are summarized in Table 3-2. At the publication of this thesis, some of the post-test results are blank as they have not yet been determined.

Using the pre- and post-test data, Bayesian estimation methods are used to calculate updated QoI estimates. As shown in the equations below, the updated QoI estimate (*posterior*) is determined by taking into account pre-test (*prior*) and post-test (*likelihood*) data. The updated QoI estimate for each mean (μ) and standard deviation (σ) is determined as follows [7]:

$$\mu_{posterior} = \frac{\sigma_{prior}^2}{\sigma_{prior}^2 + \sigma_{likelihood}^2}\mu_{likelihood} + \frac{\sigma_{likelihood}^2}{\sigma_{prior}^2 + \sigma_{likelihood}^2}\mu_{prior} \qquad [3\text{-}1]$$

$$\sigma_{posterior} = \sqrt{\frac{\sigma_{prior}^2 \sigma_{likelihood}^2}{\sigma_{prior}^2 + \sigma_{likelihood}^2}} \qquad [3\text{-}2]$$

Table 3-2: CASTOR QoIs Before and After Testing

Subsystem	Test Name	QoI	Pre-Test Estimate	Post-Test Result
Avionics	Oscillator Frequency Verification	Rise and Fall Time	Mean: 5.2ns, ≤15.6ns	Mean: 8.4ns, ≤12.4ns
	Digital Output (on/off signals) Verification	Rise and Fall Time	Mean: 10ns, ≤25ns	
		Output Low Voltage	0.00 - 0.66V	3mV
		Output High Voltage	2.3-5.5V	2.95V
		Input Leakage Current	±2uA	
	Analog Output Voltages (PDU, PPU, Flow Controllers) Verification	Voltage Error	±50mV	±11mV
	Analog Input Signals Verification	Sample Rate	≤500,000 samples/s	
		Range	0 - 3.3V	
		Error	±1.6mV	
	Scheduler Verification	Task Execution	± 10s from scheduled time	
Comm	Splitter Loss Test for Multi-Modem Integration	Splitter Loss	-3dB-15%, +10%	-3.28dB±.1dB
	Patch Antenna Qualification Test	Antenna Gain	3dB-20% to 6dB+20%	5.386dB, 1σ = 0.333dB
		Half-Power Beam Width	Vpol: 60°-5%, +30% Hpol: 60°-5%, +30%	Vpol: 70°± 2° Hpol: 80°± 2°
		Impedance	50Ω ±15%	43.18 Ω±0.5Ω
Power	Power Propulsion Unit Test: 24 to 200V Anode Converter	Voltage Error	200V±4%	
		Max Current	≤750mA	
		Efficiency	≤90%	
	Power Propulsion Unit Test: 24 to 15V Converter	Voltage Error	15V±1%	15±0.33%
		Max Current	≤8.67A	1.23A
		Efficiency	≤89%	75.34%
	Power Propulsion Unit Test: 500mA BuckPuck	Current Error	500mA±5%	15±0.47%
		Voltage Range	6-32V	1.15A
		Efficiency	≤95%	72.1%
	Battery Charging Circuit Test	Voltage Range	0-33V	
		Efficiency	≤80%	
		Max Current	≤1A	
Propulsion	Gas Feed System Test	Argon Flow Rate	9 sccm ±1%	
Structures	Vibration Test	First Natural Frequency	120Hz ±20%	61Hz ±1%

With knowledge of the updated mean and standard deviation, the next objective is to calculate the uncertainty of each QoI in a manner that enables comparison to other QoI's and the system as a whole. The concept of entropy is employed to achieve this objective. Entropy is a measure of the uncertainty in the system [8]. For a normal distribution, the entropy (h) of a QoI can be calculated using the equation 3-3 [8]. This definition allows for QoIs to be compared on a relative basis regardless of units. Furthermore, the entropies are additive which enables calculation of total entropy for the system or subsystem by summing the entropies of the individual QoIs.

$$h = \frac{1}{2}\ln(2\pi e\sigma^2)$$
[3-3]

To illustrate this process, the QoIs for the communications subsystem are considered. Using equations 3-1 and 3-2, the posterior means and standard deviations are calculated. These values are listed in Table 3-3. Note that the means and standard deviations listed in Table 3-3 use conservative, normalized estimates of the values in Table 3-2. Using this information, the entropy is calculated both before (*prior*) and after (*posterior*) testing for each QoI using equation 3-3. The results of this exercise are summarized in Table 3-3. As is evident, testing resulted in a 71% decrease in entropy for the communications subsystem QoIs under investigation.

Table 3-3: Updated Estimate of QoI Mean and Standard Deviation

QoI	From Table 3-2				Updated QoI	
	μ_{prior}	σ_{prior}	$\mu_{likelihood}$	$\sigma_{likelihood}$	$\mu_{posterior}$	$\sigma_{posterior}$
Splitter Loss	-3dB	0.45dB	-3.28dB	0.1dB	-3.26dB	0.10dB
Antenna Gain	4.5dB	2dB	5.386dB	0.333dB	5.36dB	0.33dB
Vpol Half-Power Beam Width	60°	18°	70°	2°	70°	2°
Hpol Half-Power Beam Width	60°	18°	80°	2°	80°	2°
Impedance	50Ω	7.5Ω	43.18Ω	0.5Ω	43.21Ω	0.5Ω

Table 3-4: Entropy Before (*prior*) and After (*posterior*) Testing

QoI	σ_{prior}	h_{prior}	$\sigma_{posterior}$	$h_{posterior}$
Splitter Loss	0.45dB	0.6	0.10dB	-0.9
Antenna Gain	2dB	2.1	0.33dB	0.3
Vpol Half-Power Beam Width	18°	4.3	2°	2.1
Hpol Half-Power Beam Width	18°	4.3	2°	2.1
Impedance	7.5Ω	3.4	0.5Ω	0.7
TOTAL		14.7		4.3

Chapter 4 - REXIS Preliminary Design and QoIs

The Regolith X-ray Imaging Spectrometer (REXIS) is the student collaboration experiment on the OSIRIS-REx asteroid sample return mission. This chapter is organized according to the individual studies that were conducted throughout the preliminary design process, and extensive effort is made to document the assumptions and rationale behind design decisions. The studies are quite diverse and range from discussion of an instrument performance simulation to a trade study used to forecast the labor required for software development. In addition to presenting the REXIS preliminary design, a key objective of this chapter is to identify the QoIs driving REXIS development. Table 4-1 summarizes the REXIS QoIs and provides the chapter and section number in which they are addressed.

Table 4-1: REXIS QoIs

Section	QoI
4.3- Cost and Schedule	Cost
	Schedule
4.4- Software Development	Effort
4.5- Structural Analysis	Tower and Mask Frame First Natural Frequency
	Tower and Mask Frame Maximum Stress
	Focal Plane First Natural Frequency
4.6- Detector Radiation	Aluminum Shield Thickness
4.7- Collimator Simulation	Total Detector Count
4.8- Observation Opportunities	Full-Width-Zero-Intensity Field of View
	Traverse Rate

4.1 REXIS Background

The objective of REXIS is to image the surface of 1999 RQ36 to produce a global map of the relative elemental abundances of oxygen, magnesium, silicon, sulfur, and iron. While the physics of x-ray spectrometry can quickly become burdensome, the basic concept of operation is quite simple. The sun illuminates the asteroid surface with photons covering a wide spectrum of energy. Some of these photons are in the x-ray portion of the spectrum (1.24 keV to 124 keV). Solar photons at the x-ray energy level possess the unique ability to excite elements on the asteroid surface, causing these elements to emit photons to space. Depending on the element, these photons are emitted at unique energy levels that are characteristic of the element's identity [9]. The REXIS x-ray spectrometer works by measuring the energy level and flux of photons emitted from the particulate covering the asteroid surface. This particulate is called regolith. The data collected using the REXIS instrument will allow scientists to determine (1) what elements are present on the surface and (2) how much of each element is on the surface relative to other elements. This data will provide insight into the origins of the solar system and Earth's formation.

REXIS is a soft x-ray telescope meaning that it images the asteroid regolith by detecting photons in the lower energy levels of the x-ray spectrum (0.3 to 7.5keV). Imaging is achieved using a coded-aperture mask and four CCID-41 detectors produced by Lincoln Laboratory. These features are identified in Figure 4-1. The mask contains a series of pinholes that project a pattern onto the detector. The mask's pinholes are organized to maximize the signal-to-noise ratio at the detector, and the mask pattern is convolved to resolve images of relative elemental abundances on the asteroid surface. The remaining components in Figure 4-1 describe the structure, thermal insulation, and electronics required to support the instrument. Not shown in

this figure are the solar monitor, sun shield, and radiator that will also be needed to complete the REXIS mission. For a more technical description of the REXIS preliminary design, reference the REXIS proposal provided in Appendix B.
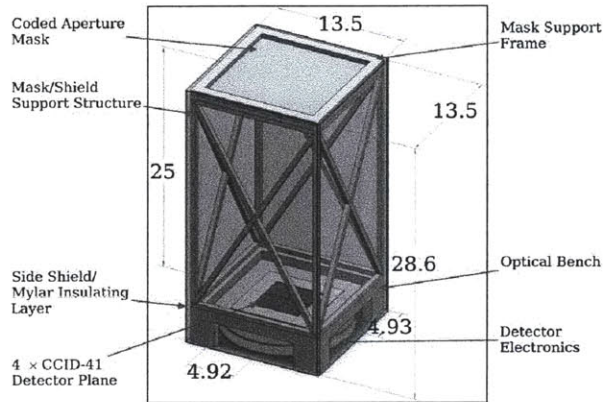
Figure 4-1: REXIS Preliminary Design. All lengths are in centimeters.

By the time the OSIRIS-REx mission launches, REXIS will have provided hands-on experience for over 100 future scientists and engineers in the design, fabrication, and test of space hardware. This educational objective is to be achieved using the Conceive, Design, Implement, and Operate (CDIO) Curriculum. The CDIO curriculum provides students with the opportunity to learn from subject-matter experts as they observe and contribute throughout all the development phases of a space engineering project. Four organizations between MIT and Harvard are participating in the design of the REXIS instrument. The MIT Space Systems Laboratory (SSL) teaches the undergraduate space engineering class and will provide the predominant source of student labor. For this reason, the SSL will serve as the lead organization for organizing hardware development. The MIT Earth, Atmospheric and Planetary Sciences (EAPS) department will provide scientific support for the mission and will co-list an undergraduate course to complement the SSL course. The MIT Kavli Institute for Astrophysics and the Harvard College Observatory bring a wealth of experience in the development of x-ray

astronomy instruments and will serve as technical mentors to students. The Harvard College Observatory also plans to recruit Harvard students from the Department of Astronomy to cross-register for the MIT space engineering class.

4.2 OSIRIS-REx Mission Overview

OSIRIS-REx is an asteroid sample return mission carrying a diverse collection of sensors and instruments to explore the asteroid 1999 RQ36. The OSIRIS-REx mission is a competitor in the NASA New Frontiers 3 program, and the OSIRIS-REx spacecraft is the vehicle that will carry REXIS to the target asteroid. The name "OSIRIS-REx" is an acronym that describes the mission's science objectives [11]:

Origins

- Return a pristine sample that provides insight into the origin of the organic compounds that enable life on Earth.

Spectral Interpretation

- Validate ground- and space-based spectral observations of an organic-rich Near-Earth Object (NEO).

Resource Identification

- Identify NEO resources that may be used for in-situ resource utilization during future human exploration missions or even asteroid mining.

Security

- Characterize the Yarkovsky Effect and its impact on asteroid orbit to expand the base of knowledge for securing Earth against future asteroid impacts. Furthermore, a precise understanding of the orbit of 1999 RQ36 is of particular interest as the asteroid has the highest probability of impacting Earth of all identified Potentially Hazardous Asteroids.

Regolith Explorer

- Explore the mineralogical and elemental content of the regolith.

40

A rendering of the OSIRIS-REx spacecraft is shown in Figure 4-2. The arm in the lower left protruding from the spacecraft is the sample collection device. The small dome beside the sampling arm (center of the instrument deck) is the sample return capsule. The REXIS payload is contained in the red box along with the other instruments on the instrument deck [12].
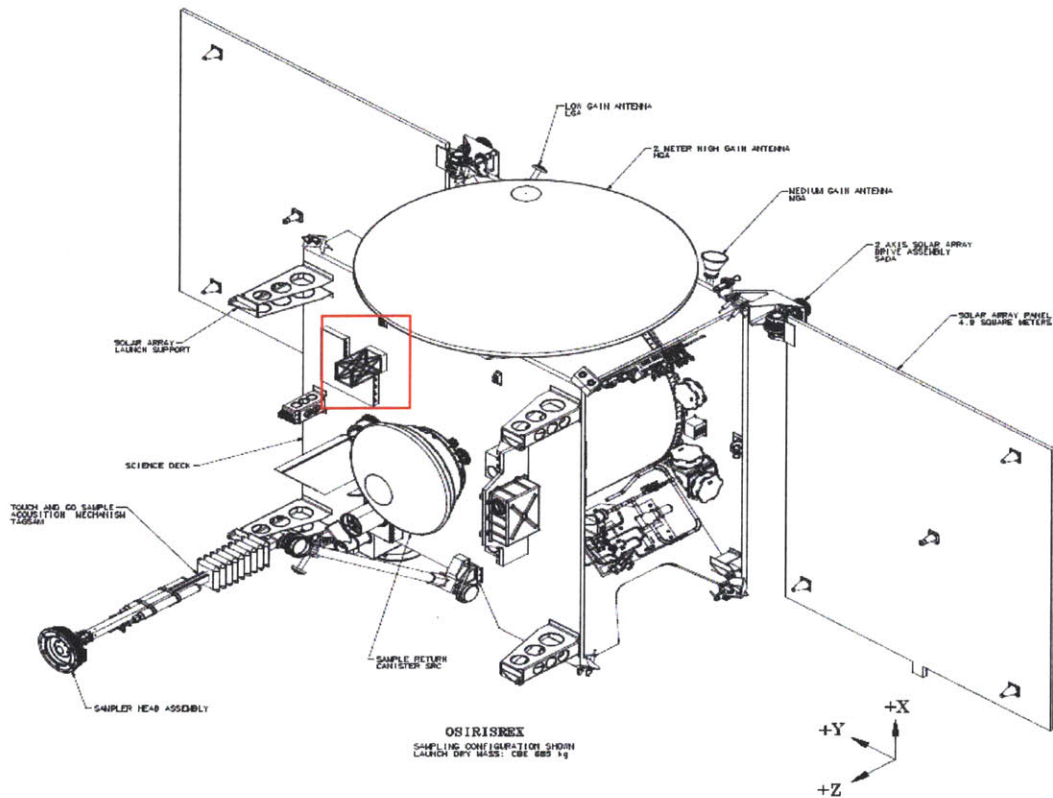
Figure 4-2: The OSIRIS-REx Spacecraft [12]

If selected, the OSIRIS-REx spacecraft is scheduled for launch in September 2016. It will cruise to the asteroid for approximately three years. Upon arrival at the asteroid in late 2019, the spacecraft will collect data to produce a detailed map of the surface from various orbits and distances. In early 2020, the spacecraft will land on the asteroid for sample collection. Up to three sampling attempts can be made. After sampling, the spacecraft will begin its cruise back to Earth with sample retrieval expected in 2023 [10].

41

4.3 Cost and Schedule

The budget for the development and operation of the REXIS payload is $5.7M through 2023. A detailed budget organized by government fiscal year (GFY) is provided in Appendix C. The preliminary REXIS schedule is in Appendix D. If the OSIRIS-REx mission is selected, REXIS funding will begin mid-December 2011. Instrument development and test will occur through 1 July 2015 when the instrument is scheduled for delivery to Lockheed Martin. Following delivery, minimal staffing is maintained for instrument operation and data analysis. The current budget and schedule allocate margins of approximately $1M and four months respectively. These margins are 20% of the total budget and 1 month per year over the duration of the program.

The unmargined development cost of the REXIS payload is $4.77M. This cost is estimated using bottom-up cost estimation. Figure 4-3 and Figure 4-4 depict program cost as a function of time and as a proportion of total program expenses respectively. Expenses are divided into six key categories. Of the six categories, salaries and research assistant (RA) tuition cover personnel-related expenses. The program has currently budgeted $1.05M for tuition and stipend for four research assistants and $2.11M for the part-time salary of three faculty members, four research specialists, and two post-doctoral researchers. Salaries are subject to overhead and employee benefits resulting in 67% and 48% increases respectively. These burdens produce a multiplier of 2.47 of the individual's base salary, making personnel the dominant expense for the REXIS program.
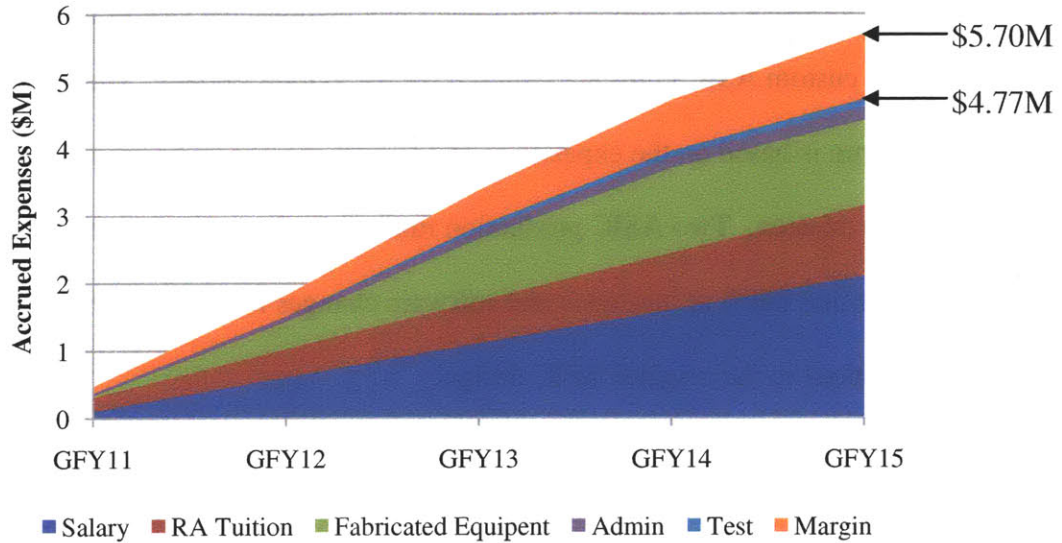
Figure 4-3: REXIS Accrued Expenses from 1 Aug 2011 to 30 Sept 2015
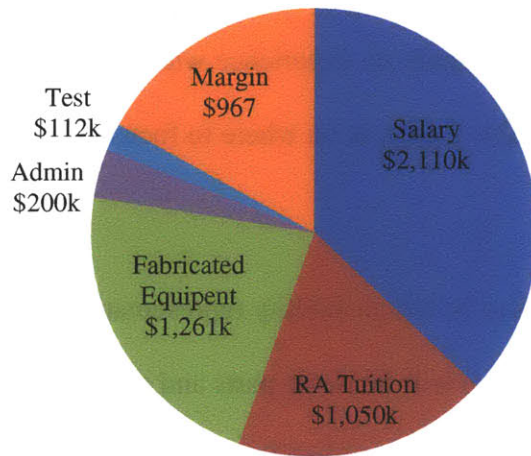
Figure 4-4: REXIS Total Expenses from 1 Aug 2011 to 31 Sept 2015

At $1.26M, fabricated equipment is the second largest program expense. The fabrication of

the Lincoln Laboratory CCID-41 detectors and two production runs of Application Specific

Integrated Circuits (ASIC's) account for 78% of total hardware cost. The estimate for the CCID-

41 detectors was obtained from Lincoln Laboratory and includes the cost of production and processing. The custom ASIC chips are required for the avionics board. The cost estimate for the ASIC batch run is based on the experience of a faculty member who recently procured ASIC chips for a space mission. Two ASIC production runs are budgeted in the event that errors are discovered in the first batch or hardware and software changes for the REXIS flight models require modifications to the original ASIC design.

The fabricated equipment budget provides the necessary resources for producing four models of the REXIS payload. The first model, Engineering Test Unit 1 (ETU-1), will be a preliminary design model made exclusively by the students in the space engineering course. ETU-1 will consist of a structural model with mass simulators and prototype electronics in an unpackaged 'flatsat' configuration to demonstrate basic hardware/software functionality. ETU-1 will allow the students the opportunity to gain hands-on experience with hardware fabrication while also providing the program with valuable feedback on where to focus effort and resources for the second model.

The second model, ETU-2, is to be a high-fidelity representation of the REXIS payload. For experience and cost savings, students will fabricate parts and electronics where possible, but complex components will be contracted to vendors for fabrication. This model is to include a coded-aperture mask, operational CCID-41 detectors, and ASICs from the first production batch. ETU-2 will be qualification tested and will undergo a battery of tests to identify software and hardware problems.

Lastly, two flight models are to be produced and delivered to Lockheed Martin. The motivation for producing two flight models is to provide (1) a backup in the event of problems

during carrier integration, and (2) a ground unit for diagnosing technical problems should they arise.

The budget also contains provisions for travel, computing, and test expenses. The travel and computing expenses are lumped as administrative expenses and are anticipated to consume 4% of the REXIS budget. The travel budget includes provisions to support the participation of 2-3 REXIS team members at OSIRIS-REx reviews, meetings, and hardware integration. Three trips are anticipated each year. Most trips will require travel to either the University of Arizona in Tucson, AZ; the NASA Goddard Space Flight Center in Greenbelt, MD; or the Lockheed Martin Space Systems Company in Littleton, CO.

The test budget for the REXIS project includes expenses for facility use such as vibration and thermal vacuum testing at Lincoln Laboratory. At only 2% of the REXIS budget, test expenses could be viewed as severely underfunded since test often accounts for 20% or more of total program cost. Two explanations exist for the modest testing budget: (1) salary expenses for REXIS testing are allocated in the salary budget, and (2) the REXIS budget assumes integrated hardware and software test will be performed by Lockheed Martin under OSIRIS-REx funding.

4.4 Software Development Analysis

The following analysis demonstrates that the current REXIS software development plan has insufficient funding and labor allocated to complete the project on time. To provide quantitative evidence for this conclusion, the COCOMO II software cost estimation tool is employed to predict the effort required to complete the project. Three scenarios are considered. The first scenario assumes that the REXIS software is developed exclusively by a post-doctoral researcher, a research assistant, and undergraduate students. The first scenario is the baseline for

this analysis as it describes the composition of the software development team as currently budgeted. The second scenario calculates the anticipated reduction in effort if a part-time software engineer is added to the team to improve process and workforce proficiency. Lastly, the third scenario estimates the implications on cost and schedule if software production is outsourced to a professional software developer. In all three scenarios, effort as measured in person-months is the QoI.

4.4.1   COCOMO II Background

Before discussing model inputs, it is appropriate that the reader possess basic familiarity with the COCOMO II software cost estimation tool. The first edition of COCOMO was published in 1981 in response to persistent schedule and budget estimation problems in the software development industry. The most current version of the model, COCOMO II, is based on meticulously collected data from a diverse sampling of software projects. The model produces an effort estimate in person-months from which cost and schedule can be derived. The dominant factor governing model output is the predicted number of source lines of code (SLOC) [13]. The REXIS team anticipates that 4,000 new lines of code and 3,000 reused lines of code will need to be developed. This estimate is based on the expert opinions of the post-doctoral researcher who will be developing the code and a Kavli technical specialist. The Kavli technical specialist contributed to the software development for the spectrometer on the *HETE-II* mission, which is the instrument from which REXIS derives much of its heritage.

The COCOMO II model employs five scale drivers and seventeen cost drivers. Scale drivers have an exponential impact on development effort and are taken into account by considering such factors as precedentedness, team cohesion, and process maturity [13]. In contrast, cost

46

drivers are multipliers of effort and consist of factors like software reliability and programmer capability [13]. When evaluating these drivers, the "nominal" entry signifies that a particular driver has an average effect on the total effort required to complete the project. In this study, discussion and analysis is reserved for off-nominal entries describing the unique characteristics of the REXIS software and organization.

4.4.2   Scale and Cost Drivers governing REXIS Software Development

Of the five COCOMO II scale drivers, development flexibility and team cohesion are largely beyond of the REXIS team's control. Development flexibility describes the project's freedom from external constraints. Given that the REXIS code will ultimately become integrated with the OSIRIS-REx software, the development flexibility driver is rated as "very low;" the REXIS software will be required to comply with strictly defined requirements, standards, and interfaces specified by the carrier spacecraft. As for team cohesion, this variable describes the ability of the program to align priorities and work as a team. While the various organizations involved in the mission are highly motivated to cooperate and succeed, a large number of organizations are involved in both REXIS and the OSIRIS-REx program and most organizations have little or no experience working together. For this reason, team cohesion is rated as "low." Table 4-2 summarizes the assignments for scale drivers.

Table 4-2: Off-Nominal Scale Drivers Independent of Scenario

Scale Driver	Rating	Justification
Development Flexibility	Very Low	Strictly defined requirements, standards, and interfaces specified by carrier spacecraft
Team Cohesion	Low	Many organizations; no experience working together

As for cost drivers, the drivers that are independent of the scenarios in this experiment include software reliability, reusability, and documentation. The reliability requirement for REXIS is "high" because coding errors could impact the scientific value of the mission, or worse, result in undesirable performance of the spacecraft and other instruments. In contrast, reliability is not set to the extreme value of "very high" because (1) errors in the REXIS code will not result in the loss of life, and (2) the OSIRIS-REx spacecraft designers are building the REXIS payload interface such that REXIS can be ejected if the payload is found to be the source of hardware or software malfunctions.

As for reusability and documentation, it is important that the REXIS code be developed with these cost drivers in mind. Since instrument design is heavily based on flight heritage, writing code for "high" reusability is essential for use in future missions. In addition, it is foreseeable that the carrier's software engineers will essentially 'reuse' the REXIS code as the payload software is integrated into the code for the OSIRIS-REx mission. It is also for this reason that REXIS documentation standards must be "very high" as many engineers and technicians on the OSIRIS-REx mission will scrutinize the student-developed code.

Lastly, the storage constraint and platform volatility cost drivers are also modified from their nominal setting. The OSIRIS-REx program has limited the REXIS payload to 100MB of data storage, which is approximately equivalent to collecting 50M photons; a quantity that could be exceeded if data is not intelligently collected. For this reason, data storage is at a premium and its cost driver is rated as "very high." In contrast, platform volatility is rated as "low" since once the spacecraft launches, there will be no changes to the hardware. Table 4-3 summarizes the assignments for cost drivers.

Table 4-3: Off-Nominal Cost Drivers Independent of Scenario

Cost Driver	Rating	Justification
Reliability	High	Coding errors could harm scientific objectives
Reusability	High	Expected use in x-ray missions beyond REXIS
Documentation	Very High	Many engineers will scrutinize student-developed code as it is integrated into OSIRIS-REx software
Data Storage	Very High	Limited to 100Mb; intelligent use required
Platform Volatility	Low	No changes to hardware after launch

4.4.3 Scenario Analysis

As a basis for comparison among the three scenarios considered, the REXIS program is currently budgeting for the full time equivalent (FTE) of one software engineer working a standard 152-hour month. Scenario 1 uses this labor estimate exclusively; Scenarios 2 and 3 explore with the impact on schedule if professional labor is added. The assumption of one FTE software engineer is derived from the combined part-time efforts of a post-doctoral researcher at 20% FTE, a research assistant at 40%, and three undergraduate students devoting approximately 5 hours per week (60 hours per month) to provide the remaining 40%. The assumption that the combined efforts of these individuals equals the productivity of one software engineer likely contains error due to the burdens required for team communication and differences in skill level.

In the first scenario, the software is to be entirely developed by one post-doctoral researcher, one research assistant, and three undergraduate students. The process maturity scale driver and personnel cost drivers are all penalized with this arrangement. The process maturity of the team is "very low" as defined by the Software Engineering Institute's Capability Maturity Model (CMM). Based on previous software development efforts, the MIT satellite team does not have the requisite planning, organization, documentation, or training policies in place to justify a rating higher than CMM Level 1, the lowest score achievable [13].

Personnel issues also penalize the team. With the exception of language and toolset experience, all personnel cost drivers are set to "very low." Personnel driver scores and justifications are summarized in Table 4-4. None of the team members have formal training in the design, analysis and test of developing code for complex applications like REXIS. Another problem is that the team is plagued with turnover rates approaching, and sometimes exceeding, 50% per year. Language experience is set to "low" as all team members are expected to have basic knowledge of the programming language prior to joining.

Table 4-4: Scale and Cost Drivers for Scenario 1: Faculty and Students

Driver	Rating	Justification
Process Maturity	Very Low	CMM Level 1 (Lower Half)
Analyst Capability	Very Low	No formal software analysis training
Programmer Capability	Very Low	No formal programming training
Personnel Continuity	Very Low	Annual turnover of 50% or more
Application Experience	Very Low	Little or no team experience with software system development
Platform Experience	Very Low	Limited team knowledge of advanced software architectures and techniques
Language Experience	Low	MIT students are expected to have knowledge of common programming languages

For the second scenario, a professional software engineer is added to the team for the purpose of elevating process maturity with the added benefit of providing training and contributing to overall program continuity. Working two days per week (40% Full Time Equivalent (FTE)), this software engineer essentially serves a hybrid role of software consultant, project manager, and code developer. The engineer is to apply prior experience developing software for space missions to organize the code-writing effort. He or she must be available to work with students during bi-weekly course meetings and is expected to supplement the team's lack of experience in advanced software development techniques. The expected benefits realized through adding a part-time engineer are summarized in Table 4-5.

Table 4-5: Scale and Cost Drivers for Scenario 2:
Software Engineer Assists Faculty and Students

Driver	Rating	Justification
Process Maturity	Low	Elevated to CMM Level 1 (Upper Half)
Analyst Capability	Low	Net benefit realized with engineer's experience
Programmer Capability	Low	Enhanced through formal programming training
Personnel Continuity	Low	Greater continuity of key players
Application Experience	Low	Management possesses experience with the software system development process
Platform Experience	Low	Net growth of team knowledge of advanced software architectures and techniques
Language Experience	Low	Unchanged due to time dependency. High student turnover prevents significant team advancement

In the third scenario, it is assumed that software development is outsourced to a full-time professional software engineer or engineering firm with prior experience developing software for space missions. This scenario alleviates much of the managerial and organizational burdens of scenarios 1 and 2, and faculty and student resources are now freed to contribute to other mission areas. The consequence of this decision is that it neglects an important educational objective to provide students with a hands-on opportunity to gain experience in a critical area of spacecraft development. The effects on cost and scale drivers for scenario 3 are summarized in Table 4-6.

Table 4-6: Scale and Cost Drivers for Scenario 3: Outsource Software Development

Driver	Rating	Justification
Process Maturity	Nominal	Assume CMM Level 2
Analyst Capability	Nominal	Experience from previous space projects
Programmer Capability	Nominal	Experience from previous space projects
Personnel Continuity	Nominal	Assume average turnover rate
Application Experience	Nominal	Knowledgeable of software development process
Platform Experience	Nominal	Demonstrated application of advanced software architectures and techniques
Language Experience	Nominal	Assume average language proficiency

Using the scale and cost drivers previously discussed, the COCOMO II model is run for each of the three scenarios to estimate effort in person-months. The additional program cost

incurred for scenarios 2 and 3 assumes a burdened salary cost (salary + overhead + benefits) of $300k/year. Scenario 2 assumes the software engineer works at 40% FTE for the entire four-year development effort, whereas Scenario 3 assumes a full-time engineer is employed for the estimated twenty month development time. The effort in person-months as well as the added program cost are summarized in Table 4-7 for all three scenarios, and screen shots of the model inputs are provided in Appendix E. Note that the added cost for scenario 3 assumes the faculty and student positions in scenarios 1 and 2 are not eliminated but instead allocated to other program needs.

Table 4-7: Effort and Added Cost of Scenarios 1, 2, and 3

Scenario	Effort	Added Program Cost
S1: Faculty & Students	84 pers-mos	$0
S2: Engineer Assists Faculty & Students	42 pers-mos	$480k
S3: Outsource	20 pers-mos	$500k

If the program proceeds with scenario 1, it will take an estimated seven years to complete the project assuming the faculty and student team are equivalent to one software engineer. This outcome is unacceptable as the OSIRIS-REx spacecraft will be on its cruise to the asteroid by the projected completion date. In scenario 2, the improvements in process and personnel with the addition of a software engineer result in an estimated completion time of 3.5 years. With an allotted payload development time of just under four years, the part-time software engineer is not only desirable but required for the project to be completed on-time. The challenge of adding this engineer is that at a total added cost of $480k, software will consume approximately 50% of the program's $1M margin. Consuming such a large portion of the margin early in the program may appear imprudent, but delaying the need for additional labor and process improvements will likely result in an even greater cost burden in the future.

Lastly, the outsourcing scenario provides an important upper-bound for estimating how quickly this project could be completed by a professional organization. At $500k, this option would consume half of the program's margin, but software development could be complete within 20 months assuming only one engineer is assigned to the project. Given that the REXIS payload is to be delivered to Lockheed Martin on 1 July 2015, twenty months prior places the program at its Critical Design Review (CDR) in December 2013. In terms of total program duration, CDR is just beyond the halfway point and is intended to mark the transition from instrument design to fabrication. If at CDR the program is not approximately halfway complete with the software development effort, the REXIS team should consider outsourcing part or all of the REXIS code to a professional software developer.

4.4.4 Recommendations and Conclusions

In summary, this study has revealed three key findings for the REXIS program using the COCOMO II software cost estimation tool. First, the software development effort as it is currently budgeted is insufficient to meet the required delivery date of 1 July 2015. Second, if the program is to achieve this date, it must improve its process maturity and personnel. It is advised that these improvements be accomplished by hiring a part-time software engineer with experience writing code for space projects. Lastly, the project must review its rate of coding progress at CDR. If software development is less than 50% complete, the program should outsource some or all of the remaining project.

When evaluating this study, it is important to recognize the limitations of the COMOCO II model. First, the model was used near, and perhaps beyond, the extent of its intended bounds when evaluating some variables. The personnel continuity cost driver is one example as student

turnover is often 50% or higher. Furthermore, the software is being developed in the context of an academic setting and not a business, meaning that the REXIS program is obliged to satisfy educational objectives in addition to operational objectives. These fundamental differences may result in effort increases that were not captured by the model's designers.

4.5 Structural Analysis

Structural analysis of the REXIS preliminary design is performed to identify potential trouble areas requiring further analysis and redesign for the detailed CAD model. The tower and mask frame subassembly, the focal plane, and the electronics boards are the structures under consideration. The first natural frequency (FNF) of all three structures and the maximum von-Mises stress in the tower and mask frame are the QoIs. These analyses are performed using a combination of analytical and numerical techniques. Because the launch vehicle for the OSIRIS-REx mission has not yet been identified, the REXIS payload has no formal launch load requirements. For the purposes of this analysis, a structure is considered at-risk if its FNF is below 100Hz or if the structure's yield strength is exceeded when 10G accelerations are applied simultaneously along the instrument's three primary axes. These requirements are derived from the specifications contained in the User's Guides for the University Nanosatellite Program [14] and ESPA class satellites [15].

4.5.1   Tower and Mask Frame

As shown in Figure 4-5, the tower and mask frame are the structures of greatest interest in this investigation as they are cantilevered from the side of the spacecraft and are anticipated to experience the most severe loads during launch. The REXIS tower is a box truss constructed using extruded aluminum rod. The rod is 0.5cm x 0.5cm square and contains a hollow center. The side walls are 0.1cm thick. Joint connections at the truss corners are welded. The mask

frame sits atop the tower and is simplified to a solid extrusion that is 1cm in width and 1cm in height around the mask perimeter. The gold mask is excluded from this analysis because its strength and mass contributions are negligible relative to the tower and mask frame.

The finite element model for these structures is made using FEMAP v10.1.1 for pre- and post-processing activities. NEi NASTRAN v10.0 is used as the solver. The tower and mask frame are to be constructed using aluminum 6061-T651. The material properties for this alloy are derived from *Metallic Materials Properties Development and Standardization* (MMPDS-03) and are shown in Table 4-8:

Table 4-8: Aluminum 6061-T651 Material Properties [16]

Material Property	Value
Young's Modulus, E	68.2GPa
Poisson's Ration, ν	0.33
Mass Density, ρ	$2700\frac{kg}{m^3}$

The REXIS finite element model consists of a custom grid assembled manually using 176 nodes all connected using 200 elements. A rendering of this model is shown in Figure 4-5. The tower and mask frame are modeled using beam elements with hollow and solid cross-sections respectively. The assembly is constrained at the four corners of the tower. The nodes at these positions are fixed in X, Y, and Z-translation to form a pinned boundary condition. The validity of this boundary condition is dependent upon the assumption that the tower and mask frame are mounted on a rigid electronics box. Loads are created by simultaneously applying 10G accelerations along the principal axes to simulate worst-case launch loads.
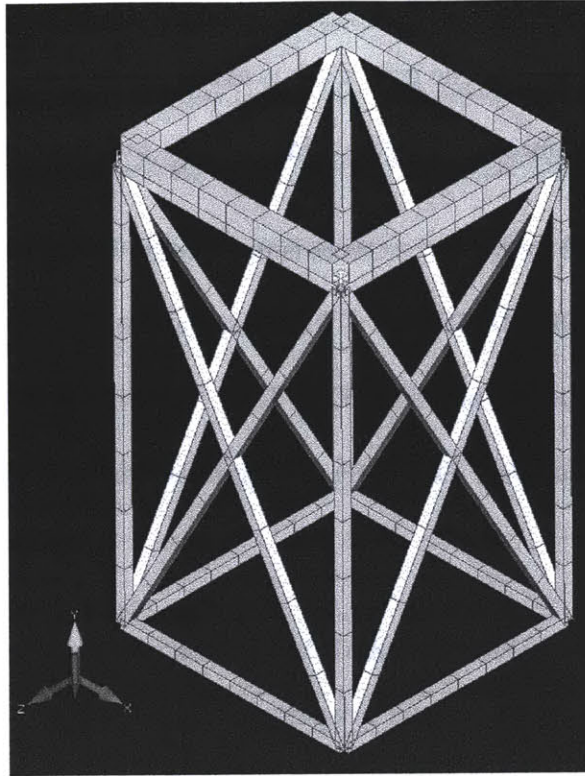
Figure 4-5: Finite Element Model of the REXIS Tower-Mask Assembly

Prior to conducting stress and modal analysis, two tests are performed to verify the model's accuracy: (1) the Single Point Constraint (SPC) test and (2) the unconstrained boundary condition (Free-Free) test. The SPC test compares the weight of the finite element model to the weight of the CAD model when a 1G acceleration is applied along the instrument's Y-axis. This comparison serves to verify that the finite element model and CAD model share common mass properties. The outputs of the SPC test are expected to be four equal loads located at the four corners at the base of the tower. The test is satisfied if the sum of these loads matches the weight of the instrument with less than 1% error. The SPC test for this experiment is passed as the CAD and finite element weights agree to within 0.2%.

For the Free-Free test, the constraints at the bottom of the tower are removed and a modal analysis is performed to confirm that no unintended constraints exist. This test is satisfied when

56

the model's first six rigid-body modes are effectively zero (10E-5 or less). After conducting the Free-Free test on the tower-mask model, the test verifies that the unconstrained model's first six modes are all less than 10E-5.

Once the precursory model tests are satisfied, the modal and structural analyses are performed. From the modal analysis, the predicted first natural frequency (FNF) of the tower-mask assembly is 357Hz. When animated, this first mode shape is a symmetric 'breathing mode' shown in Figure 4-6.
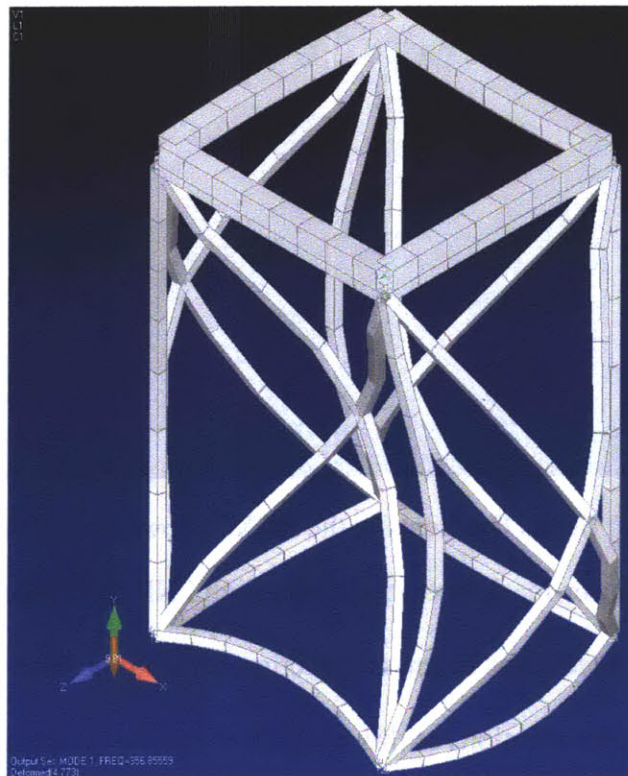
Figure 4-6: The REXIS Tower-Mask Assembly's First Mode Shape at 357Hz

As for structural analysis, the stress results of the tower and mask assembly are summarized in Figure 4-7 assuming a worst-case acceleration of 10G is applied simultaneously along all three

axes. The scale units in Figure 4-7 are in pounds per square inch. The greatest stress observed in the tower-mask assembly occurs at the top of the vertical truss member aligned with the body-load acceleration vector. The anticipated stress in this element is 3.18 MPa, which provides a factor of safety of 75.7 against yield. Note that this analysis does not account for any stress concentrations introduced by the joint's welding or geometry. These omissions may substantially reduce the calculated factor of safety, and future analyses should be expanded to account for these effects. Should stress concentrations result in an unacceptable factor of safety, gusset plates can be added at the truss joints to provide a substantial increase in stiffness.
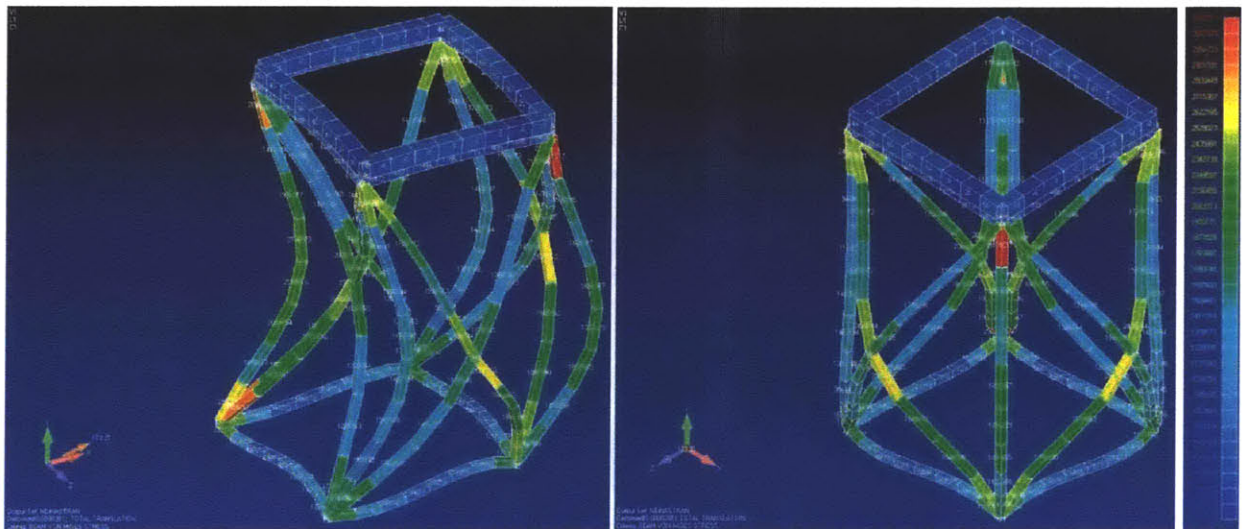
Figure 4-7: Stress Gradients in the REXIS Tower-Mask Assembly

As is evident by the tower-mask assembly's very high FNF and factor of safety against yield, these structures are good candidates for mass reduction and optimization should mass become a critical design factor. Future iterations of this analysis should be performed using launch load requirements provided by the OSIRIS-REx program office. As necessary, model fidelity may be improved by increasing the number of nodes and elements around areas of interest such as the welded truss joints. Due to the variability in welding techniques, future design iterations should consider alternatives to welding such as using pinned or fastened joints. Furthermore, future

analysis should be expanded to the gold mask as it is necessary to ensure the membrane will not permanently deform when exposed to the launch vehicle's vibrational and acoustic environment.

4.5.2   Detector Plane Analysis

Modal analysis of the aluminum plate supporting the detector plane is performed to ensure the instrument's CCID-41 detectors will not be damaged by the vibrational and acoustic launch environment. For the purposes of preliminary design, the FNF of the detector plane is estimated using analytical solutions available in Robert Blevins's *Formulas for Natural Frequency and Mode Shape*. The solutions contained in this manual are derived from empirical test data. For the REXIS focal plane, shown in Figure 4-8, the detector rests on a 2mm thick plate with a clamped boundary condition around the 11.5cm x 11.5cm square plate. The material properties for the aluminum 6061-T651 used to fabricate the plate are derived from MMPDS-03[16].
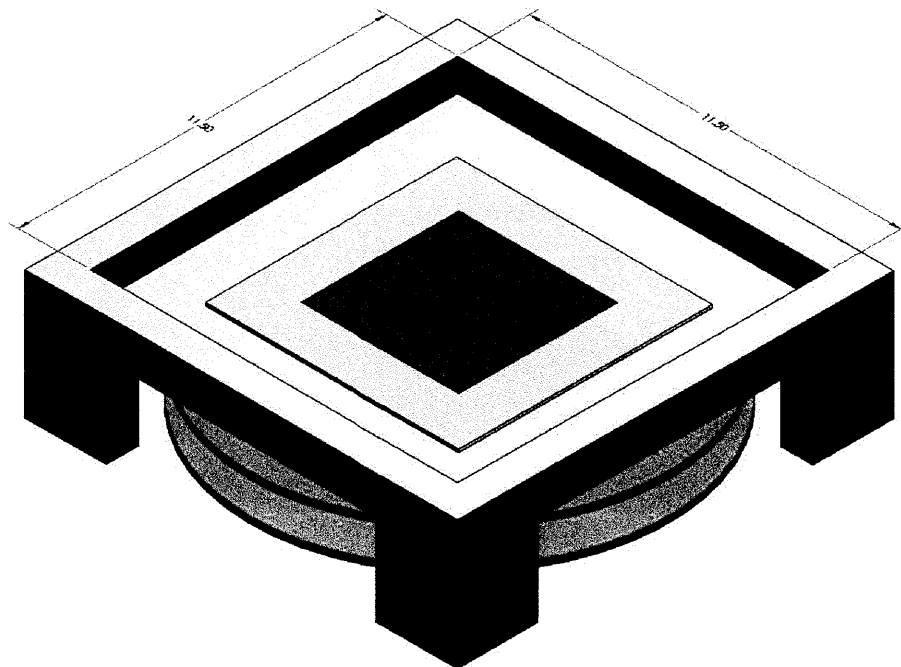
Figure 4-8: REXIS Focal Plane

59

Using Table 11-4 in Blevins, the natural frequencies for a uniform, clamped rectangular

panel are calculated using [17]:

$$f_n(c, d) = \frac{\lambda_{cd}^2}{2\pi a^2} \sqrt{\frac{D}{\gamma}} \qquad [4\text{-}1]$$

In this equation, f_n is the natural frequency; λ_{cd}^2 is a dimensionless parameter based on the

boundary condition and retrieved from Table 11-4 ($\lambda_{cd}^2 = 35.99$) [17]; a and b are the

dimensions of the plate ($a = b = 0.135$m); c and d are positive, whole numbers corresponding to

plate modes ($c = d = 1$); γ is the plate's mass per unit area ($\gamma = \rho t = 5.4 \frac{kg}{m^2}$); and D is the plate

bending constant calculated using the formula [17]:

$$D = \frac{Et^3}{12(1-\nu^2)} \qquad [4\text{-}2]$$

In this equation, E is the modulus of elasticity for aluminum 6061-T651 (E = 68.2GPa) [16], t is

the plate thickness (t = 0.002m), and ν is Poisson's ratio for the plate material ($\nu = 0.33$).

Using these equations, the plate's FNF is calculated to be 1,329Hz. While this FNF appears

quite conservative, three considerations beyond FNF necessitate the current design and preclude

the plate from optimization at this time. First, excessive deflection of the plate's focal plane

could damage the fragile CCID-41 detectors and their electrical connections, so a rigid plate with

an FNF substantially above launch requirements is desirable. Second, machining the plate below

the prescribed 2.0mm thickness becomes impractical as vibration and heat between the cutting

tool and aluminum plate will result in a poor surface finish. Third, this analysis does not account

for the modal contributions of surface mounted components such as the detectors or the radiation

shield that must be included in future analyses as the design matures.

4.5.3   Electronics Board Analysis

The electronics boards consist of plates fabricated using G10/FR4 fiberglass upon which high-value electronic components like the ASIC chips will be mounted and fragile electrical connections will be made. The following analysis employs a parameter sweep of the analytical solution techniques presented in Blevins to determine the boards' FNF as a function of (1) board thickness and (2) the mass of electrical components mounted on the board. To bound the parameter space, a worst-case scenario is considered by assuming the boards extend to the perimeter of the 11.5cm x 11.5cm electronics box. Note that this makes the boards square as shown in Figure 4-9 as opposed to the circular boards shown in REXIS renderings elsewhere in this document. The board is secured using rigid standoffs that form the corners of a 7cm x 7cm concentric square.
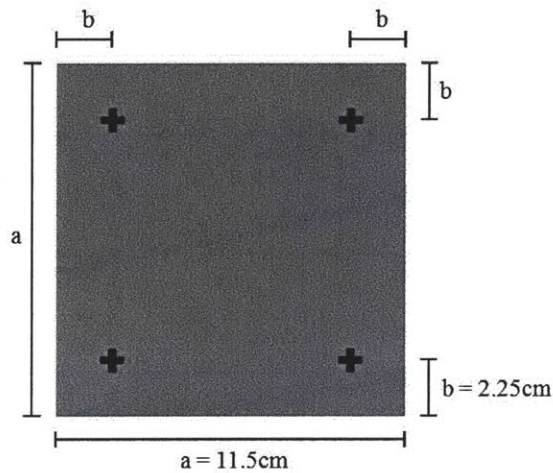
Figure 4-9: REXIS Electronics Boards as a Square Plate with Four Pin Supports.

The equation for calculating the board's FNF is identical to that used in section 4.4.2. The dimensionless parameter term, λ_{cd}^2 is retrieved from Table 11-6 in Blevins as $\lambda_{cd}^2 = 19.69$ for the boundary condition in Figure 4-9 [17]. The density and elastic modulus for G10/FR4 are $\rho = 1850 \frac{kg}{m^3}$ [18] and E = 18.6GPa [19] respectively.

61

To perform the parameter sweep, the board thickness and total component mass are varied. Three board thicknesses are investigated: 0.02in (0.5mm), 0.031in (0.8mm), and 0.047in (1.1mm). These thicknesses are considered because they are the three thinnest sizes of G10/FR4 offered by the MIT satellite team's board fabrication vendor (Advanced Circuits). Total component mass is varied between 0g and 100g. This analysis is performed by assuming the total component mass is 'smeared' across the board's 11.5cm x 11.5cm surface area as would approximately be the case for electronic components distributed across a printed circuit board. The smeared mass per unit area is added to the board mass per unit area for incorporation into the FNF calculation. The results of this parameter sweep are shown in Figure 4-10.
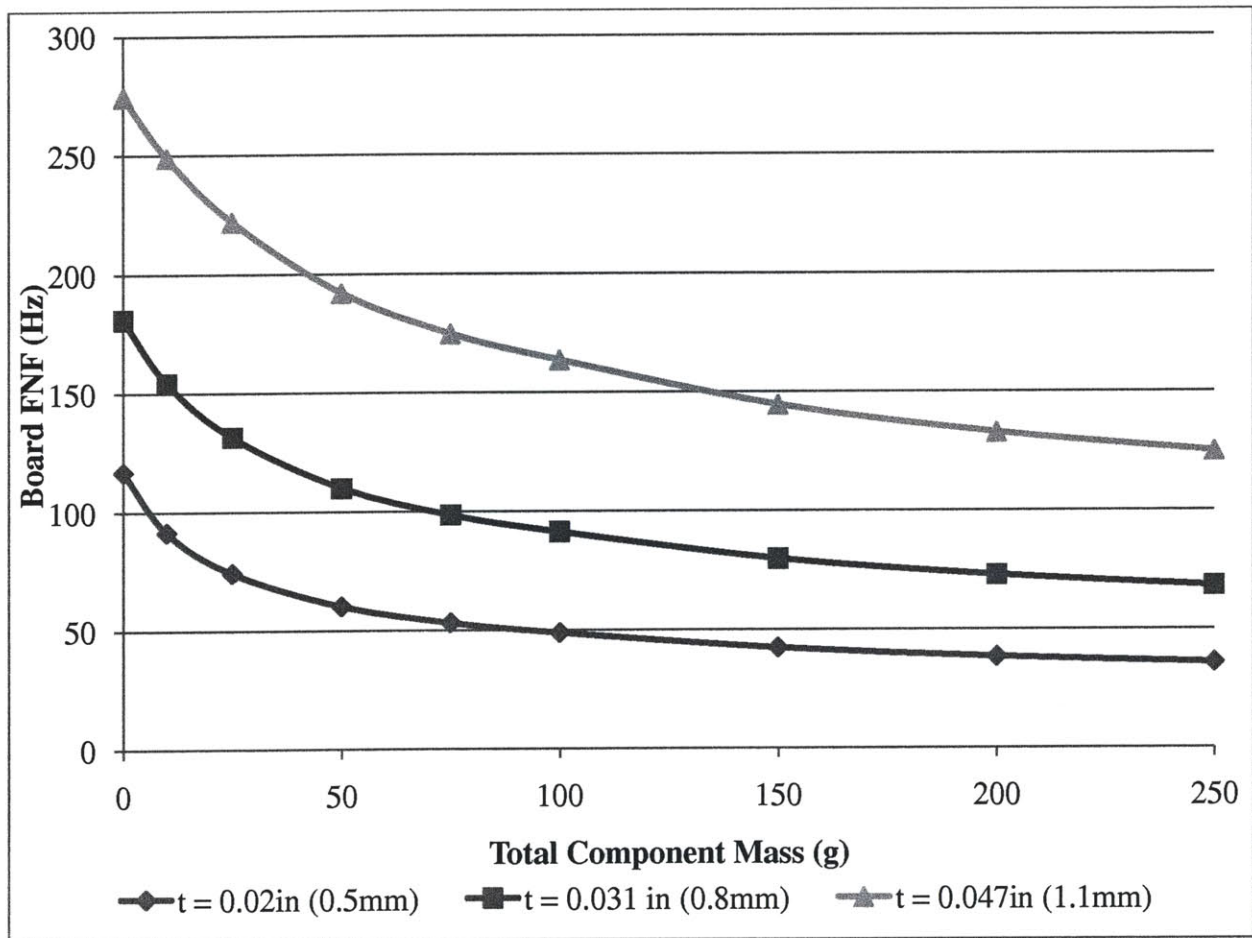
Figure 4-10: REXIS Electronics Board FNF for Standard Board Thicknesses

62

This parametric sweep serves as a lower bound for estimating the FNF of the boards contained in the 11.5cm x 11.5cm REXIS electronics box. The sweep assumes the electronic components are approximately evenly distributed over the board surface to form a smeared mass. As the REXIS design matures and electronic component masses become known, designers can use this table to quickly and confidently select a board thickness that conserves mass yet satisfies launch vibe requirements.

4.6 Detector Radiation Analysis and Shield Design

During the 3.5 year cruise from Earth to 1999 RQ36, REXIS will be bombarded with high-energy particles from the sun and deep space. Over time, radiation exposure will degrade REXIS's four CCID-41 detectors, wielding the instrument useless unless sufficient shielding is provided to mitigate damage. Radiation shielding is commonly achieved using dense metals such as lead or aluminum, which add mass to the instrument. In this section, the allowable radiation dose for the Lincoln Laboratory CCID-41 detector is calculated. Using the maximum allowable dose along with the output of a space environment modeling program called SPENVIS, the required thickness of an aluminum radiation shield is determined to ensure the instrument will operate as intended upon arrival at the asteroid. The aluminum shield thickness is the primary QoI in this analysis.

4.6.1   Detector Background

An x-ray detector such as the Lincoln Laboratory CCID-41 is grown from a single silicon crystal. Silicon is used because of the material's favorable charge transfer properties. The detector operates by collecting charge imparted by incoming photons on pixels etched into the crystal surface. The pixels hold the charge until the detector's electronics measure the charge at each pixel and then ground or 'refresh' the pixel array to begin the next imaging cycle. The

quality of x-ray spectrometry is dependent on (1) the efficiency of charge transfer and (2) the accuracy of charge measurement. High-energy particles from the sun and deep space degrade the detector's ability to efficiently transfer charge, thereby reducing spectral resolution [22].

A common metric of detector performance is charge transfer inefficiency (CTI). The CTI of a new detector is approximately 10E-6. Exposure to heavy particles (protons primarily) can damage the detector's crystal lattice by displacing silicon atoms. These imperfections in the crystal lattice can result in electron traps that increase the detector's CTI and reduce spectral resolution. Radiation dose is often measured in terms of the ionizing dose (unit: rad) that is produced through exposure to high-energy charged particles such as x-rays and gamma rays. For the CCID-41 detectors on REXIS, the non-ionizing dose due to protons and other heavy particles is of interest. The unit of measurement for the non-ionizing dose is mega-electron volt per gram (MeV/gm). In estimating detector degradation, CTI is proportional to non-ionizing dose [22].

4.6.2 Calculation of Maximum Allowable Radiation Damage for the CCID-41 Detector

The allowable degradation (or maximum CTI) for the REXIS detectors is calculated using *Suzaku* heritage flight data [23]. *Suzaku* is an x-ray telescope launched by the Japanese Aerospace Exploration Agency (JAXA) in July 2005 to explore x-ray energy sources in deep space. The detectors used on the *Suzaku* mission share heritage with the CCID-41 detectors on REXIS. After five years in low earth orbit, *Suzaku*'s detectors have degraded to a CTI = 5×10^{-5} [23]. This degradation produces adequate spectral resolution for the REXIS instrument. Using data from *Suzaku* ground radiation tests, the CCID-41 detector's CTI increases per 1MeV/gm dose of radiation according to [23]:

$$\frac{d(CTI)}{d(dose)} = 2.0 \pm 0.5 \times 10^{-12} \left(\frac{MeV}{gm}\right)^{-1}$$

Since the maximum allowable CTI = 5×10^{-5}, the maximum allowable radiation dose is calculated to be:

$$Allowable\ Dose = \frac{5 \times 10^{-5}}{2.0 \times 10^{-12}} \frac{MeV}{gm} = 2.5 \pm 0.5 \times 10^{7} \frac{MeV}{gm}$$

4.6.3 Radiation Shielding

The radiation shield thickness required to protect the REXIS detectors is calculated using an internet interface called the Space Environment Information System or SPENVIS. Upon registration, SPENVIS is provided free of charge by the European Space Agency for modeling space environment effects due to cosmic rays, the radiation belts, and solar particles.

The REXIS radiation model is created in three steps. The first step is to generate the spacecraft trajectory. The REXIS detectors require protection for approximately 3.25 years from launch in September 2016 to arrival at 1999 RQ36 in January 2020. The orbit type selected for the cruise is near-Earth interplanetary at a distance of 1AU from the sun. After defining the trajectory, the next step is to identify the radiation sources and effects. The sun is the predominant radiation source, so the JPL solar particle model is employed at both the 95% and 99% confidence levels. The damage due to trapped protons and electrons is the effect of interest, so the AP8 and AE8 models are employed at solar minimum to correspond with the anticipated state of solar activity during the cruise to the asteroid. The last step is to identify non-ionizing energy as the long-term radiation dose of interest. The damage factor is set to 2.0 $\times$ $10^{-12} \left(\frac{MeV}{gm}\right)^{-1}$ in order for the relative degradation output to directly correspond with detector CTI. These steps and the SPENVIS inputs are summarized in Appendix F.

Figure 4-11 depicts detector degradation as a function of aluminum shield thickness for the 95% and 99% confidence levels. In reviewing these plots, it is evident that a shield thickness of approximately 6.2mm is required to ensure the radiation dose will not exceed the maximum allowable $2.5 \pm 0.5 \times 10^7 \frac{MeV}{gm}$ at the 95% confidence level. In contrast, a substantially larger shield over 20mm thick is required to achieve the 99% confidence level. These two values serve as lower- and upper-bounds for guiding the future decision on mask thickness. Reducing the REXIS shield thickness below the 6.2mm lower-bound may compromise the mission. On the other hand, a shield thickness over 20mm will likely not be practical due to mass limitations. In short, the REXIS radiation shield thickness should be at least 6.2mm, and any additional mass that can be allocated from the OSIRIS-REx program should be applied to increasing the radiation shield thickness for improved mission assurance.
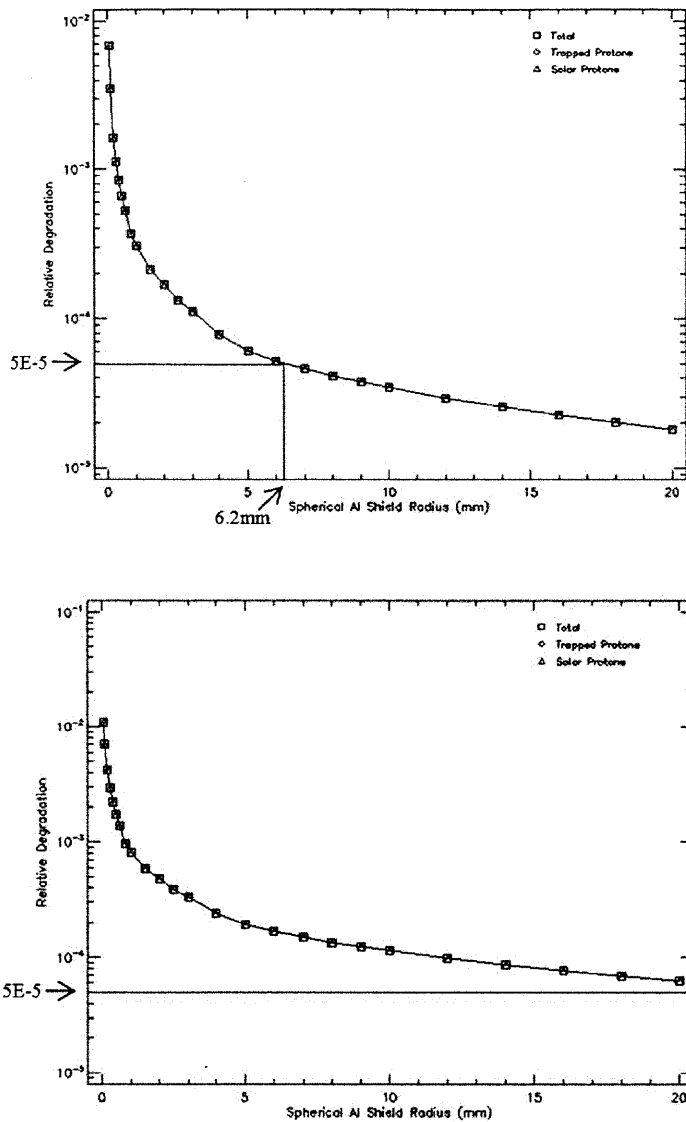
Figure 4-11: Degradation as a Function of Aluminum Shield Thickness for the 95% (TOP) and 99% (BOTTOM) Confidence Levels

4.6.4   Preliminary Radiation Shield Design

The objective of this section is to define the tradespace for designing the radiation shield once it is appropriate to develop a more detailed design for this critical component. The shield design process is divided into three distinct steps. The first step is to select the shield deployment motion, the second step is to select the shield geometry, and the third step is to select the shield deployment mechanism. Note that in the previous section the horizontal axis in Figure

67

4-11 specifies a shield radius and assumes a spherical shield will be used. For the purposes of machinability and mass efficiency, the REXIS baseline design intends to use a flat plate with a thickness equal to the prescribed radius. Future radiation analyses should consider the effects of shield geometry. A key assumption in the preliminary design of the radiation shield is that the OSIRIS-REx spacecraft provides adequate radiation protection for the backside of the detector. This assumption should be confirmed prior to initiating detailed shield design.

The baseline design for the REXIS radiation shield is that it will be fabricated from aluminum 6061-T651 and will have dimensions of approximately 5cm x 5cm with a thickness between 6.2mm and 20mm. These dimensions provide an anticipated shield mass between 42g and 135g. Should the instrument design permit, the REXIS team may have the option of purchasing a commercial-off-the-shelf (COTS) mechanism. This option is preferable as COTS components often have flight heritage and may offer cost savings over developing and qualifying a custom mechanism. For future reference, Honeybee Robotics is a manufacturer of space-qualified mechanisms for operations such as shield deployment [25]. In addition, *Spacecraft Structures and Mechanisms* by Thomas Sarafin is an excellent resource for sizing and selecting mechanisms used commonly in space applications [26].

The preliminary requirements for the shield are that it must deploy exactly one time after remaining stowed and locked at all times during launch and cruise to the asteroid. During cruise, the OSIRIS-REx spacecraft allocates 2W for instrument survival heaters that may be used to preserve the deployment mechanism and other instrument components, but the mechanism should be designed to operate following 3.25 years of extreme thermal cycling. Upon deployment, the shield may not separate from the instrument. Furthermore, the mechanism must

be designed such that the shield cannot move into an orientation that obstructs the detector's field of view.

The first decision in designing the shield deployment mechanism is to select the desired motion. Two candidate motions are described in Figure 4-12. The perceived advantage of option one is the simplicity of design as rotation is constrained about a single pivot point. A disadvantage is that it may be a challenge to ensure the shield remains in a locked position that does not occlude the instrument's field of view following deployment. Option two mitigates this hazard by translating in the horizontal plane. A potential disadvantage of option two is that complex compound motion may be required as vertical translation may be necessary prior to horizontal translation to avoid damaging the detectors as the shield is removed. Furthermore, as the instrument is currently designed, option two or variants thereof may interfere with the base of the tower.

Option 1: Rotation about a hinge (Side View)

Cover

Detector Focal Plane

Option 2: Translation (Side View)

Cover

Detector Focal Plane
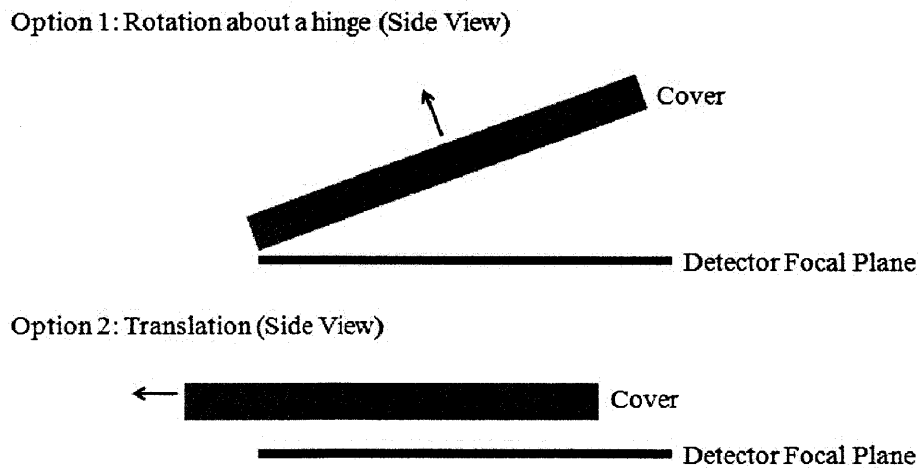
Figure 4-12: Two Options for Radiation Shield Deployment Motion

The second decision in designing the shield deployment mechanism is to select the shield geometry. Example renderings of three candidate options are shown in Figure 4-13. These three options exist in a continuum on which mechanism complexity is traded for size, where size is

defined as the envelope required for both the stowed and deployed configurations. The key trade is that as the volume for deployment becomes smaller, mechanism complexity increases. The first option is to use a solid shield. The simplicity of this design is its primary advantage; deployment is possible with minimum mechanization. In contrast, moving a solid shield may require more volume than is available depending on the selected motion and instrument design. The third option exists at the other end of the continuum as it fits neatly within a compact dynamic envelope but introduces the added challenge of deploying four independent petals.

Simple　Bulky　　Option 1: One Solid Cover (Top View)

Complexity　Size

Option 2: Two Halves (Top View)

Option 3: Four Petals (Top View)

Complex　Compact
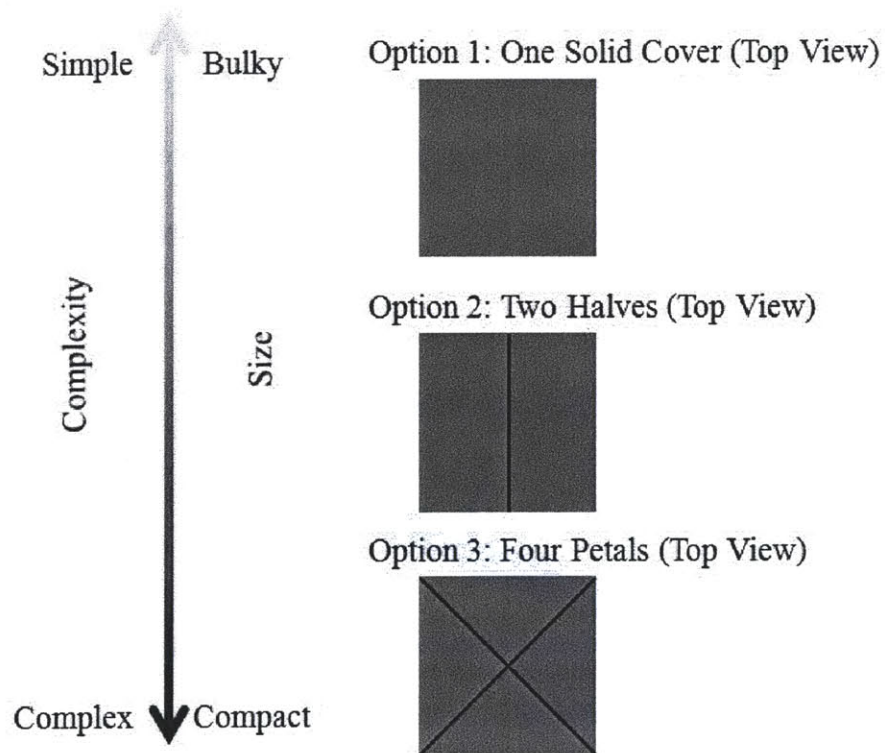
Figure 4-13: Three Options for Shield Geometry

The third decision in designing the radiation shield and deployment system is to select the mechanism or mechanisms that will deploy and lock the shield in its final position. Reliability and mass efficiency are two essential design features for the REXIS deployment mechanism. Candidate deployment mechanisms include linear actuators, solenoids, and a spring paired with an electro-resistive wire that melts when current is applied to allow deployment. Once the shield

70

is deployed, a locking mechanism may be required to ensure the shield does not occlude the detector. Example locking mechanisms include magnets, a hard-stop behind a spring, or a linear actuator with self-locking worm gear.

4.7 Collimator Mode Simulation

Data collected using the REXIS payload will complement the OSIRIS-REx mission by identifying relative elemental abundances on the surface of the asteroid, thereby enabling program scientists to identify sites of interest for sample collection. The REXIS data can be analyzed to provide two useful perspectives on the asteroid surface. A localized perspective is provided by operating in imaging mode in which relative elemental concentrations are determined by segmenting the surface into 4.3m x 4.3m squares at a distance of 700m from the surface. In contrast, a global perspective is obtained by operating the instrument in collimator mode. In this mode, the total number of counts at the detector is the QoI. Collimator mode enables scientists to perceive macroscopic differences in surface composition that may be too subtle to notice between images collected in imaging mode. These differences may occur over large areas called "blobs" that vary in elemental concentration from the homogenous surface conditions.

4.7.1 Simulation Code Structure

The anticipated number of counts expected due to elemental excesses and deficits on the asteroid surface is predicted using the Collimator Count simulation. This simulation is programmed using the Interactive Data Language or IDL^{TM}. The following discussion provides a summary of the Collimator Count simulation. To supplement the discussion in this section, the simulation source code is provided in Appendix G. The simulation consists of four programs. The block diagram in Figure 4-14 describes the data flow between the programs. The batch file,

71

`countbat.pro`, serves as the driver script for the Collimator Count simulation as it compiles

and runs `countpro.pro` and `countrun.pro`. Following processing, the batch file,

`plotbat.pro`, is used to plot the results of `countbat.pro` and its constituent programs.
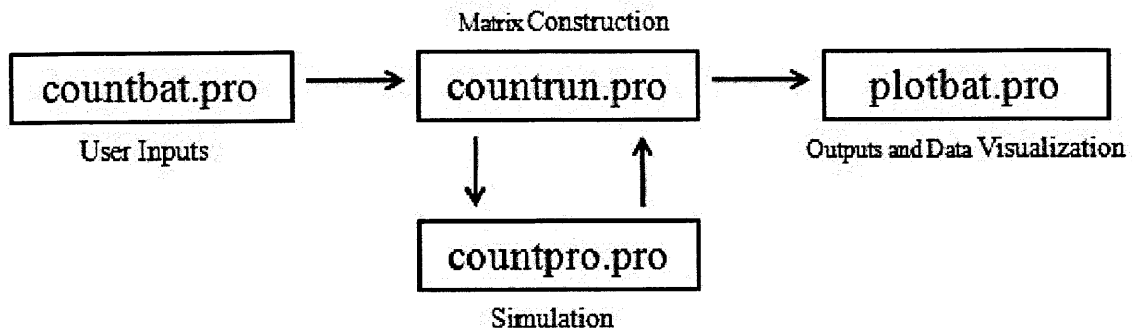
Figure 4-14: Collimator Count Simulation Block Diagram

The user-defined inputs for countbat.pro are defined below:

w_d – detector width in centimeters. The default value is 4.92cm, which is the expected width of the 2x2 array of CCID-41 detectors. It is assumed that the length and width of the detector array are equal.

w_m – mask width in centimeters. The default value is 9.84cm, which is twice the width of the detector as required by the design for a uniformly redundant array [21].

dist_d2m – distance between the detector and mask in centimeters. The default value is 25cm to provide the FWZI-FOV of 32.8° at a distance of 700m to the asteroid surface as defined for the REXIS preliminary design. This is the most easily adjusted parameter for modifying the instrument's field of view.

dist_sc2ast – distance between the OSIRIS-REx spacecraft and the asteroid in meters. The default value is 700m.

flux – the anticipated counts per second that will strike the detector (1) taking into account filtering provided by the mask, and (2) assuming the surface of 1999 RQ36 is perfectly homogeneous. The default value is 27 counts per second, which assumes a local noon observation position looking onto a disk.

dur – duration at the observation position in earth days. The default is 21 days.

conc_arr – array containing concentration factors. Concentration factors greater than 1.0 signify an excess, factors less than 1.0 signify a deficit. These factors serve as multipliers applied across the blob.

blob_rad_arr – array containing radii of a 'blob' on the asteroid. A 'blob' is an area or sum of areas of excess or deficit concentration. The units for this input are square meters.

sm – sigma multiplier. This value prescribes the confidence level that must be achieved to surpass the threshold count and assumes the photons strike the detector according to a Poisson distribution.

Using the defined input parameters, the `countrun.pro` program is called.

`Countrun.pro` contains the logic for computing and storing the count rate and derived quantities of interest for each of the concentrations (conc) and blob radii (blob_rad) prescribed by the user. The output arrays are called:

ActCount_arr – "Actual Count" floating point array; an array containing count rates corresponding to each of the user-defined concentration (conc) and blob surface area (blob_rad) inputs.

Thresh_arr – "Threshold" floating point array containing the excess and deficit thresholds that must be exceeded for detection.

ET_arr- "Exceed Threshold" integer array containing a -1 entry if a deficit is detectable, a 0 entry if a deficit or excess is undetectable, and a +1 entry if an excess is detectable for each of the user-defined concentration (conc) and blob surface area (blob_rad) inputs.

`Countrun.pro` calculates each entry in the output matrices by calling the function `countpro.pro`. `Countpro.pro` uses the user-defined inputs to first calculate the half-angle (θ) of the fully-coded (FC), full-width-half-max (FWHM), and full-width-zero-intensity (FWZI) fields of view (FOV). These half angles are illustrated in Figure 4-15. The FC FOV is the maximum angle at which the entire detector observes the asteroid surface. The FWHM FOV is the maximum angle at which exactly one-half of the detector observes the asteroid surface. Lastly, the FWZI FOV is the angle beyond which no portion of the surface is observed by the detector.

73
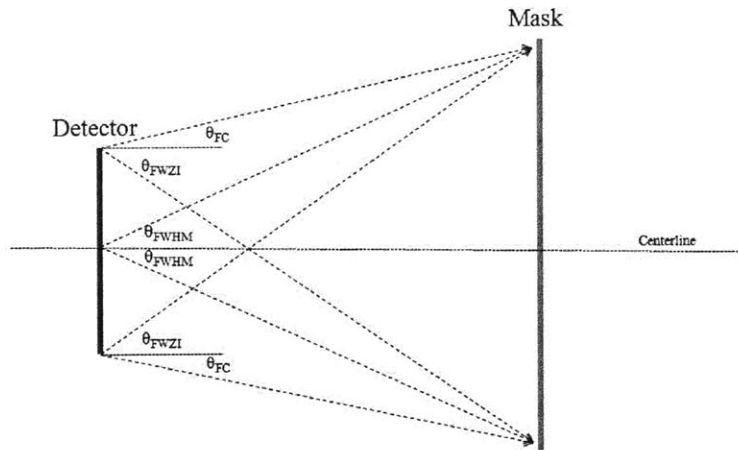
Figure 4-15: Half Angles (θ) for the Fully-Coded (FC), Full-Width-Half-Max (FWHM), and Full-Width-Zero-Intensity (FWZI) Fields of View (FOV)

After computing the half angle, `countpro.pro` calculates the side length and surface area covered by the FOV as a function of the distance to the asteroid. Figure 4-16 shows the various FOV's as projected on the 600m diameter asteroid from a distance of 700m to the asteroid center. The FWZI FOV is used for the remainder of the simulation to predict the total number of counts across the entire FOV.
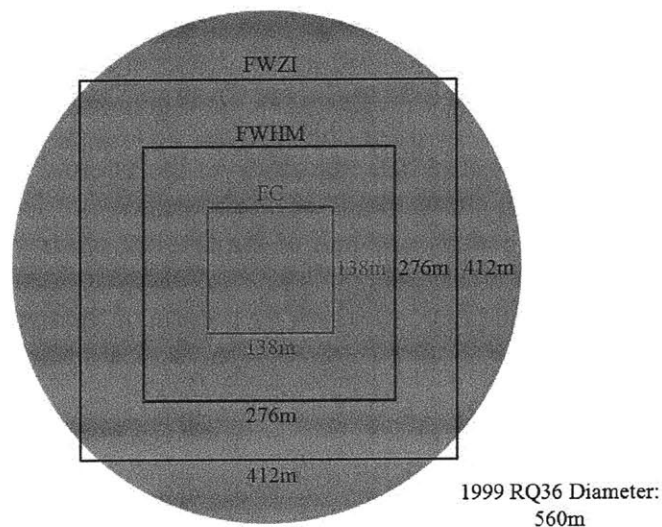
Figure 4-16: FOVS Projected onto Asteroid at 700m to Center

Next, the expected total count from a homogeneous patch on the asteroid is calculated. This variable is called NomCount for "nominal count." This calculation converts the user input for duration (dur) into seconds and then determines the duration spent observing any one patch (dur_patch) by multiplying the duration times the fraction of the total asteroid surface observed. The variable NomCount is found by multiplying the user-defined flux by dur_patch. The count distribution is assumed to be a Poisson distribution. This assumption is appropriate since the simulation (1) is based on the probability of a number of events (counts) occurring in a fixed period of time and (2) these events occur with a known average rate (27 counts/s) [27]. As a Poisson distribution, the standard deviation (NC_StDev) is estimated by taking the square root of NomCount [27].

The final step in countpro.pro is to calculate the expected number of counts when an excess or deficit of elements exists on the surface. The expected number of counts is then compared to the threshold value to conclusively determine if a deficit or excess exists. The variable representing the expected number of counts is called ActCount, which is the abbreviated form of "actual count." The ActCount variable is determined by adding the excess or deficit count contributions to the expected count that would be observed if the asteroid were homogeneous in composition. The excess and deficit contributions are calculated by multiplying the blob area times the concentration normalized about the homogeneous surface composition (i.e. conc = 1.0).

Excess Contribution (i.e. conc > 1.0): $unit\_flux * (\pi * blob\_rad^2)(conc - 1)$

Deficit Count Contribution (i.e. conc < 1.0): $unit\_flux * (\pi * blob\_rad^2)(conc - 1)$

Next, the threshold count is calculated for the purpose of evaluating a detectable excess or deficit. The threshold calculation is centered about the nominal count (NomCount). The excess threshold adds the product of the user-defined sigma multiplier (SM) and nominal count standard deviation (NC_StDev) to the nominal count (NomCount). Likewise, the product is subtracted from the nominal count (NomCount) for the deficit scenario. If the actual count is beyond the threshold, an excess or deficit is reported for the corresponding surface area and concentration.

4.7.2   Collimator Simulation Results

The following results demonstrate the anticipated performance of the REXIS instrument for various blob sizes and concentrations of oxygen on the surface of 1999 RQ36. Plots specific to magnesium and iron are included in Appendix H. The simulation assumes the instrument observes the surface from a local-noon position at 700m from the center of the asteroid. Furthermore, the asteroid surface is assumed flat, not spherical, and the surface is fully illuminated by a quiescent sun.

The plots in Figure 4-17 and Figure 4-18 consider the effects of concentration and blob radius on the total number of counts emitted by oxygen atoms on the asteroid surface. The homogeneous surface condition is represented by a blob radius of 0m or a concentration of 1.0. As expected, the number of counts observed becomes more exaggerated as blob radius and concentration diverge from the homogeneous condition. Furthermore, note that concentrations less than 1.0 signify a deficit condition, which is why the number of counts decreases with increasing blob size. In Fig 4-14, the blob radii of 2.4m, 203m, and 242m are intentionally selected to illustrate key design points. The 2.4m radius produces the equivalent surface area coverage as the 4.3m x 4.3m pixel size. At the other extreme, a blob with a 206m radius is the maximum blob size that will fully fit within the instrument's 32.8° FWZI FOV at a distance of

700m to the asteroid center. Lastly, the blob radius of 232m produces an absolute upper-bound. A blob with a radius of 232m produces a surface area equivalent to the instrument's maximum coverage as limited by its square FOV.
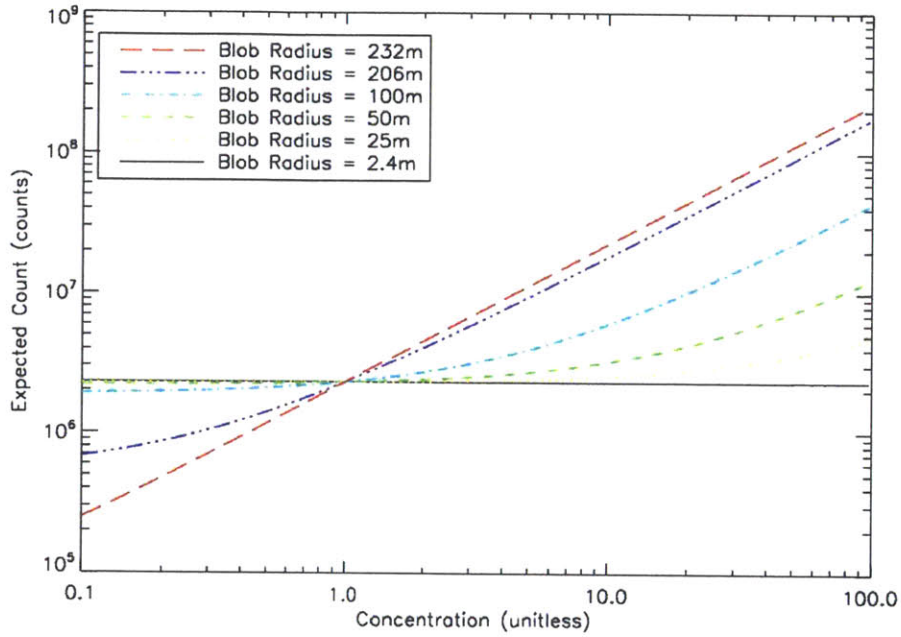
Figure 4-17: Expected Number of Counts at Detector for Various Concentrations of Oxygen
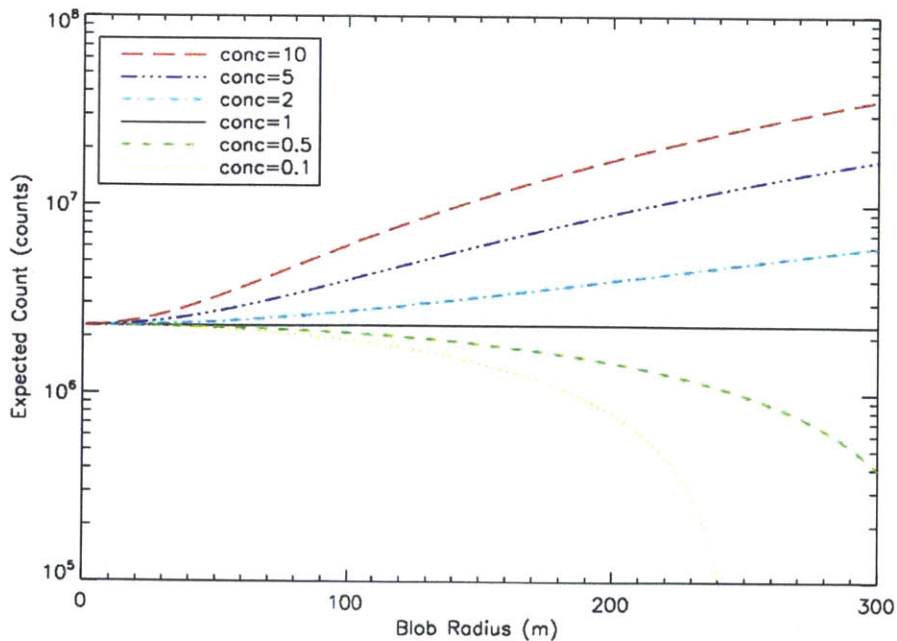
Figure 4-18: Expected Number of Counts at Detector for Various Blob Sizes of Oxygen

77

The plots in Figure 4-19 and Figure 4-20 show the requisite blob size and concentration necessary to detect the presence of an elemental excess or deficit at a defined confidence level. As described in the previous section, the counts are emitted from the asteroid surface according to a Poisson distribution. In order for there to exist a detectable excess or deficit, the number of counts must exceed a threshold defined by the expected nominal count and confidence level (sigma multiplier). Figure 4-19 demonstrates the possible combinations of surface areas and concentrations to produce a detectable excess (white) and deficit (black) at the 5σ confidence level. Note that the green shading indicates that neither an excess nor a deficit are detectable. Figure 4-20 is an identical plot but over a continuum of 0σ to 100σ. Excesses above 100σ are shown in white.
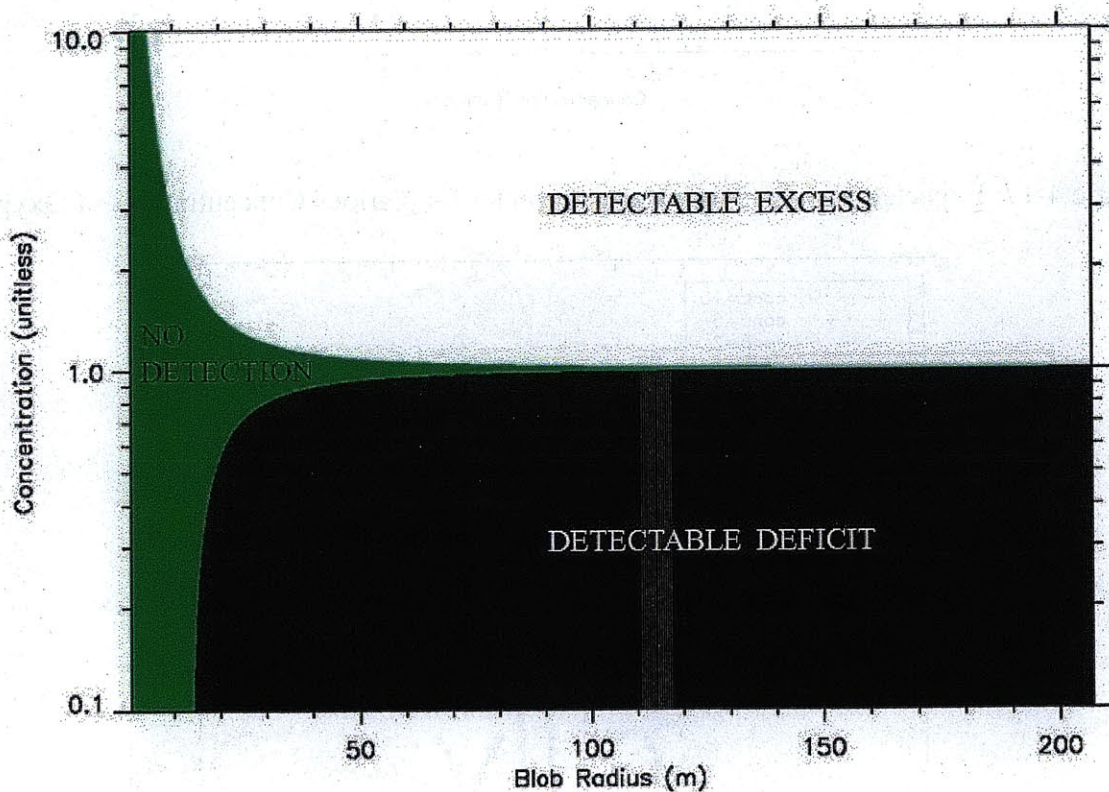
Figure 4-19: Detection of Oxygen at 5σ Confidence
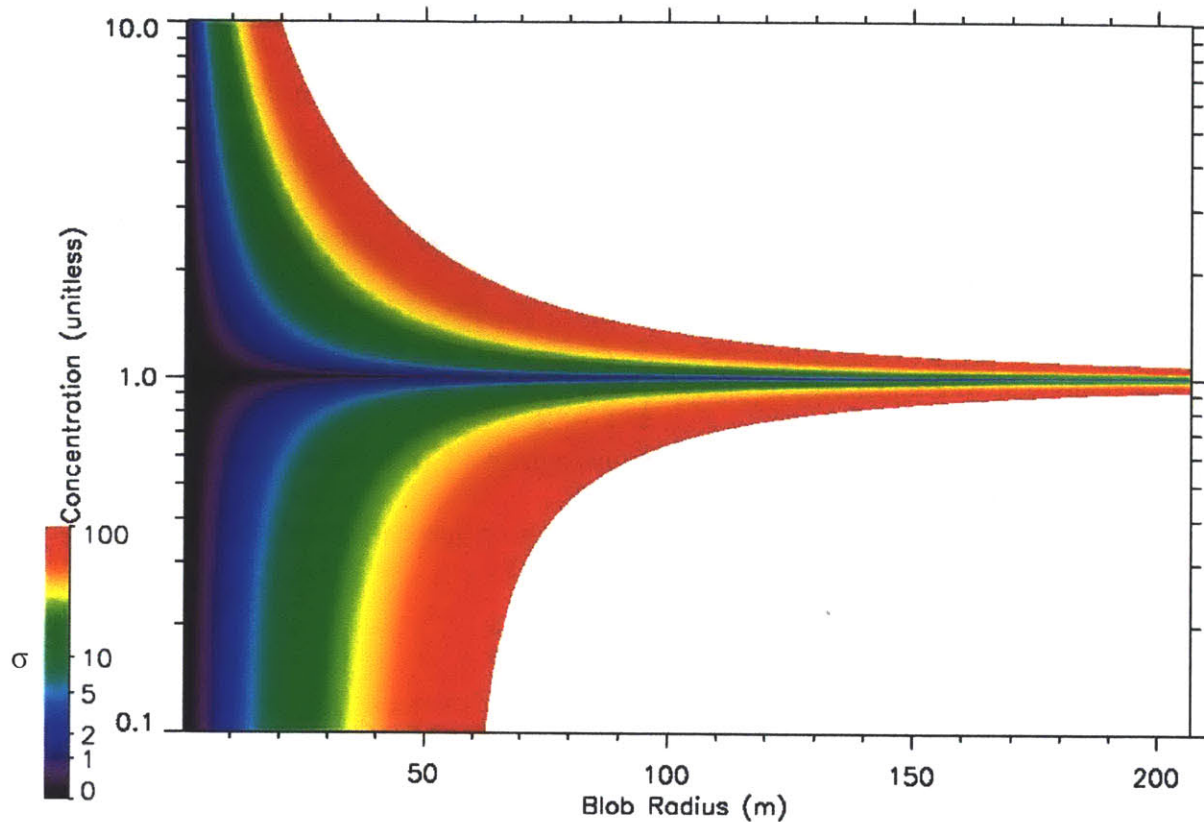
Figure 4-20: Detection of Oxygen as a Function of Confidence (σ)

4.8 Observation Opportunities

In order to size the REXIS spectrometer's field of view and detector, it is first necessary to identify the phases during the mission when the instrument is capable of viewing the surface. The REXIS payload is designed to observe the asteroid at a distance of 700m from the asteroid center with a pointing accuracy of 21 arcmin. This distance was initially selected using information contained in the "NASA OSIRIS-REx Student Collaboration Experiment" [20]. With the arrival of the "OSIRIS-REx Design Reference Mission," it is now possible to conduct a more exhaustive exploration of the observation opportunities for the REXIS payload [10]. The two QoIs in this exploration are the instrument's full-width-zero-intensity field of view (FWZI-FOV) and traverse rate.

The REXIS FWZI-FOV is determined by the dimensions of the CCD detector and the distance between the detector and the mask. As a uniformly redundant array, the dimensions of the coded-aperture mask must be twice the dimensions of the detector [21]. Therefore, the mask dimensions are beyond the design space for the REXIS payload. As discussed in detail in Section 4.7: Collimator Simulation, the FWZI-FOV is 32.8°. The FWZI-FOV is of interest because it is the widest angle at which any part of the detector can observe the surroundings. At distances greater than 700m from the asteroid center, the instrument's FWZI-FOV exceeds the 560m-diameter asteroid, allowing galactic cosmic rays from deep space to introduce error into measurements.

The REXIS traverse rate is a function of the spacecraft's velocity relative to the surface of 1999 RQ36 as well as the spacecraft's pointing accuracy. To achieve the desired 21 arcmin angular resolution specified in the REXIS Proposal (Appendix B), the instrument must not traverse more than 10 arcmin during each 8s exposure, or 1.25 arcmin/s. The 10 arcmin value is less than one-half of the desired angular resolution in order to comply with the Nyquist-Shannon sampling theorem. The requirement driving the 8s exposure time is derived from the spectrum of desired coverage. If exposure time is increased, the detector will become saturated.

The calculations used to determine expected traverse rate are best illustrated using an example. These calculations require only basic knowledge of trigonometry, statistics, and the rate equation: $distance = velocity * time$. This example analyzes the first reconnaissance flyover in Phase 6, and is organized using four steps to illustrate unique sources of error. The first step is to calculate the image shift due to the spacecraft's velocity relative to the asteroid surface. Second, the traverse introduced due to the spacecraft's knowledge and pointing accuracy is determined. Third, the traverse from the slewing maneuvers performed in Phases 4B

80

and 6 are calculated. And fourth, the total expected traverse rate is calculated using the root mean square (RMS) method for the traverse estimates calculated in steps 1-3. The total traverse rate must be less than or equal to the maximum traverse rate of 1.25 arcmin/s to be a valid observation opportunity.

Step 1: Traverse due to Spacecraft Ground Track

During Phase 6-Reconaissance, a series of four flyovers are to occur to evaluate candidate sample selection sites. The distance to the asteroid surface is 500m and the velocity relative to the surface is 0.12 m/s. A rendering of this scenario is shown in Figure 4-21.
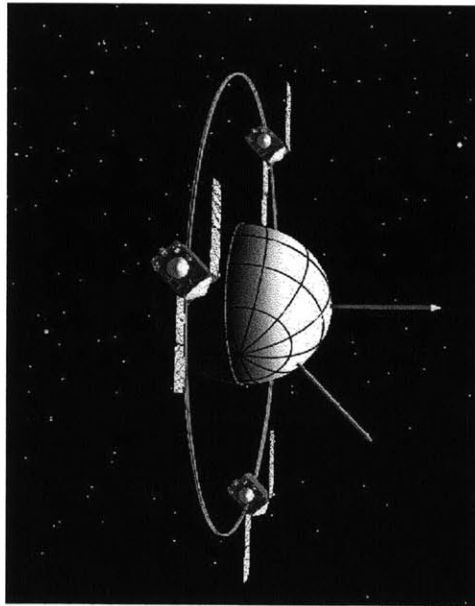
Figure 4-21: Illustration of Spacecraft Traverse over Asteroid Surface

$$Position\ after\ 8s\ =\ 8s * 0.12\frac{m}{s}\ =\ 0.96m$$

$$Traverse\ =\ \tan^{-1}\left(\frac{0.96m}{500m}\right) = 6.6\ arcmin$$

Step 2: Traverse due to Spacecraft Pointing Knowledge and Accuracy

Lockheed Martin reports that the spacecraft's pointing knowledge will be 1.0 arcmin and pointing accuracy will be 3.4 arcmin. Both values are at the 3σ confidence level.

Step 3: Traverse due to Cone Slew Maneuver

During Phase 4B – Detailed Survey as well as Phase 6 – Reconnaissance, the spacecraft performs a cone-slew maneuver at ±3.4° every 80s and ±1.4° every 75s respectively [10]. The resulting ground track due to the cone-slew maneuver is traced on the asteroid surface by the red and blue circles in Figure 4-22. The colored boxes and circles represent the various fields of view of the OSIRIS-REx instrument suite at a distance of 500m to the surface. These fields of view are relative to a 50m x 20m site of interest signified by the yellow ellipse. These instruments have much shorter exposure times than REXIS and therefore do not experience an equivalent loss in image resolution due to the cone-slew maneuver.
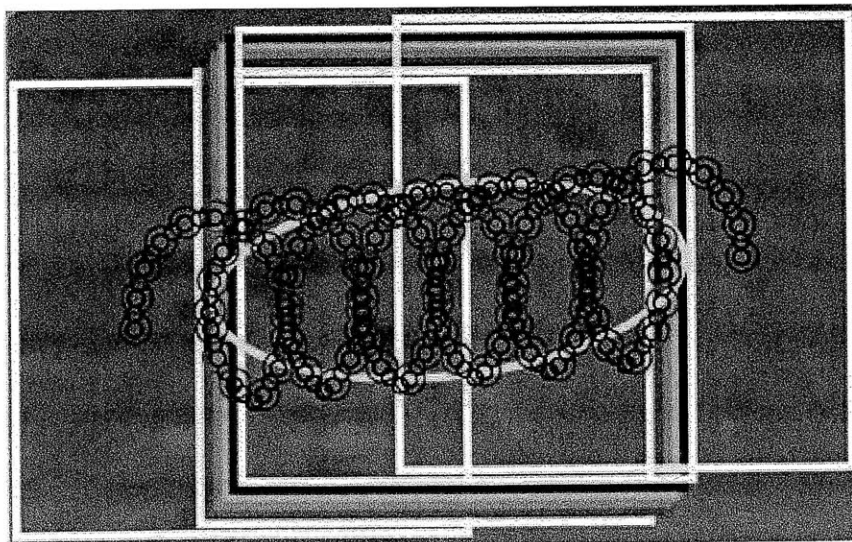
Figure 4-22: Ground Track during Cone Slew Maneuver

The traverse due to the cone slew maneuver in Phase 6 is calculated assuming an 8s exposure at 500m from the asteroid surface:

$$Slew\ Raduis\ on\ Surface: \quad radius\ =\ 500m * \tan 1.4° \ =\ 12.2m$$

$$Circumerence\ on\ Surface: \quad circum\ =\ 2\pi * radius\ =\ 76.8m$$

$$Traverse\ Rate\ =\ circum/75s\ =\ 1.02\ m/s$$

$$Traverse\ Angle\ =\ \tan^{-1}(Traverse\_Rate/500m)\ =\ 0.117°/s\ or\ 7.01\ arcmin/s$$

$$S/C\ Cone\ Slew\ =\ Traverse\_Angle * Exposure\_Duration$$

$$S/C\ Cone\ Slew\ in\ 8s\ =\ 56\ arcmin$$

Step 4: Root Mean Square Traverse Rate

The contributions from steps 1-3 to the overall traverse rate are uncorrelated. Therefore, the overall traverse rate is estimated using the root mean square of the individual traverse contributions.

$$Traverse\ Rate\ =\ \frac{\sqrt{Grnd\_Trk^2 + Ptng\_Knwldg^2 + Ptng\_Accy^2 + Slew^2}}{Exposure\_Duration}$$

In Phase 6, the traverse rate is:

$$Traverse\ Rate\ =\ \frac{\sqrt{6.6^2 + 1^2 + 3.4^2 + 56^2}}{8}\ \frac{arcmin}{s}$$

$$Traverse\ Rate\ =\ 7.1\ arcmin/s$$

Of the ten phases in the OSIRIS-REx mission, phases 4-8 are candidates for instrument operation as the spacecraft is within observation range of 1999 RQ36. Phases 1-3 encompass launch and cruise to the asteroid. Phases 9 and 10 are for the cruise back to Earth and sample recovery. The observation opportunities for Phase 4A (P4A) through Phase 8 Step 3 (P8S3) of the OSIRIS-REx mission are defined in Table 4-9 and Figure 4-23. Reference the "OSIRIS-REx Design Reference Mission" [10] for more information on each phase. In Table 4-9, green

highlighting indicates that the phase satisfies both the traverse rate (<1.25 arcmin/s) and the observation range (<700m) requirements. Yellow highlighting indicates that the traverse rate is satisfied, but the observation range is exceeded. In Figure 4-23, only mission phases with traverse rates less than the required 1.25 cm/s (red line) possess sufficient image stability for imaging.

As seen in Table 4-9, Phase 5B Orbital B is the only phase that satisfies both the range and traverse rate requirements. Beyond the 700m range, galactic cosmic rays introduce error as particles are detected from sources other than the asteroid surface. In addition, the galactic sources may be strong enough to saturate the CCD resulting in detector pile-up. For this reason, observations in Phases 4 and 5A are prohibited using the current FWZI-FOV, and substantial redesign would be required to observe during these phases. The observation opportunities in Phase 6 are within range but exceed the maximum traverse rate due to the cone slew maneuver. Without the cone slew maneuver, the traverse rate falls to approximately 1.0 arcmin/s: well within the 1.25 arcmin/s requirement. The REXIS and OSIRIS-REx programs are currently exploring the possibility of making observations during Phase 6 when the cone slew maneuver is not being performed.

Table 4-9: Traverse Rate by Mission Phase

Phase Description	Traverse Rate (arcmin/s)	
	Actual	Required
P4A- N Pole Flyover (6700m)	0.60	1.25
P4A- S Pole Flyover (6700m)	0.46	1.25
P4A- Equatorial Flyover (6700m)	0.46	1.25
P4B- Rot Obs 30° phase (4700m)	15.41	1.25
P4B- Rot Obs Equatorial (4700m)	15.41	1.25
P4B- Rot Obs Polar (4700m)	15.41	1.25
P5A- Orbital A (1200m)	0.46	1.25
P5B- Orbital B (700m)	0.46	1.25
P6- Recon Flyover 1 (500m)	7.07	1.25
P6- Recon Flyover 2 (500m)	7.09	1.25
P6- Recon Flyover 3 (500m)	7.11	1.25
P6- Recon Flyover 4 (500m)	7.05	1.25
P7S1/P8S1- Checkpoint (125m)	6.07	1.25
P7S2/P8S2- Descent (125m)	7.71	1.25
P7S2/P8S2- Descent (30m)	32.03	1.25
P7S3/P8S3- Matchpoint (30m)	2.33	1.25

KEY: Out of Range
Within Range
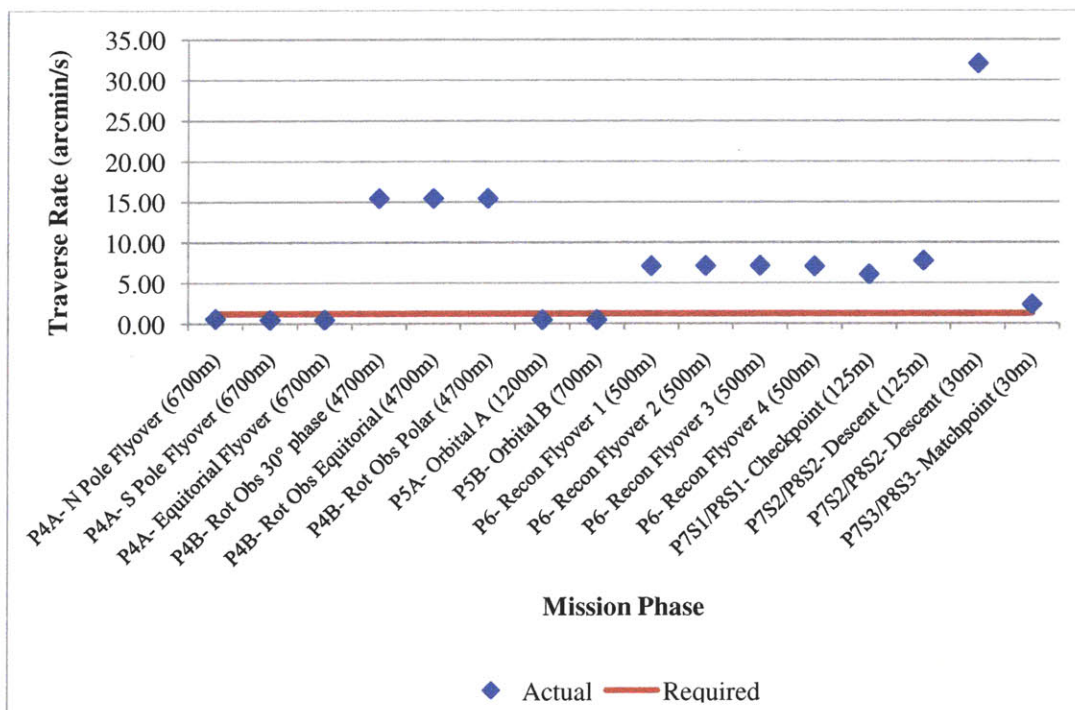
Figure 4-23: Traverse Rate by Mission Phase

4.9 REXIS QoIs and Future Work

By mapping the elemental abundances on the surface of 1999 RQ36, the REXIS instrument will provide valuable context for sample collection and insight into the history of our solar system. In addition, the REXIS instrument will offer over ten graduate and one hundred undergraduate students the opportunity to gain hands-on experience building and testing space hardware. The preliminary design efforts documented in this chapter provide an analytical basis for future instrument development should the OSIRIS-REx and REXIS missions be selected. Furthermore, this chapter establishes the foundation for applying stochastic process decision methods to monitor and guide the development of the REXIS x-ray spectrometer.

4.9.1   Summary of REXIS QoIs

Each subsystem analysis in this chapter identifies QoIs driving the REXIS design. These QoIs are summarized in Table 4-10. To contain the uncertainty of the REXIS QoIs, lower and upper bounds (LB and UB respectively) are defined wherever possible. The rationale for these boundaries is traceable to the analysis presented in the sections throughout this chapter. As the REXIS design matures, additional QoIs will be identified, and QoI estimates will evolve as formal requirements are established and the design is matured. For stochastic process decision methods to be effective, it is imperative that QoIs are monitored and reported back as updates become available.

Table 4-10: REXIS Quantities of Interest

Section	QoI	Estimate	Uncertainty
4.2- Cost and Schedule	Cost	$4.77M	UB: +20% (+$1M)
	Schedule	46 months	UB: +8.7% (+4 mos)
4.3- Software Development	Effort	84 pers-mos	LB: 20pers-mos, UB: 100 pers-mos
4.4- Structural Analysis	Tower and Mask Frame FNF	357 Hz	LB: 100Hz
	Tower and Mask Frame Max Stress	3.18 MPa	UB: 241 MPa (Al yield strength)
	Focal Plane FNF	1329 Hz	LB: 100Hz
4.5- Observation Opportunities	FWZI FOV	32.8°	LB: 28° (1200m to surface), UB: 120° (OSIRIS Rqmt)
	Traverse Rate	1.25 arcmin/s	UB: 1.25 arcmin/s
4.6- Collimator Simulation	Total Detector Count	50M	LB: 1M
4.7- Detector Radiation	Aluminum Shield Thickness	6.2mm	LB: 6.2mm, UB: 20mm

4.9.2 REXIS Future Work

Prior to beginning the detailed design of REXIS, several critical items must be addressed as early as possible to avoid costly delays and redesign in the future. First, the REXIS team needs to obtain a set of requirements from the OSIRIS-REx program. The development of these requirements must be a dialogue between REXIS and OSIRIS-REx. In particular, the REXIS team must continually remind the OSIRIS-REx program of the need for a solar monitor, radiator, and sunshade. These three hardware components were not included in the original submission of the REXIS proposal, but the need for these components has become evident through the preliminary design effort. The solar monitor is needed to provide context relative to solar conditions for evaluation of the spectral lines emitted from the asteroid surface. The radiator and sunshade are needed to accommodate the -60°C operating temperature of the CCID-41 detectors.

In parallel with establishing requirements, the REXIS and OSIRIS-REx programs must coordinate to develop the REXIS Concept of Operations. This document should specify the distance from the instrument to the asteroid surface and the duration of imaging. The REXIS team must be certain to communicate that the REXIS baseline design calls for a traverse rate less than 1.25 arcmin/s. Understanding the operating conditions will define the instrument's FoV and

allow for more exact simulation of the total number of counts anticipated at the detector. These key constraints will largely drive the mechanical and electrical design of the REXIS instrument.

Once REXIS funding is established, the procurement process for long-lead items must begin. The manufacture and processing of the CCID-41 detectors is anticipated to require one year for delivery. Similarly, each production run for the ASIC chips is anticipated to take six months.

Lastly, REXIS must be proactive in working with Lockheed Martin to define the mechanical, electrical, and software interfaces with the OSIRIS-REx spacecraft. An interface control document (ICD) should be established early in the REXIS development process and meticulously maintained through the duration of the project.

Chapter 5 - Modeling the Structural Dynamics of Rigid Component Attachment to a Square Plate as Applied to Small Satellite Panels

It is common practice in satellite design to mount a component or box to the surface of a spacecraft panel. An example may include a reaction wheel mounted on a side panel. The additional mass has the consequence of reducing the panel's first mode. This effect is, to a varying extent, countered by the box stiffness which provides additional rigidity to the panel. This experiment explores the impact of box footprint on panel modal response by testing a panel with three boxes of approximately equal mass but increasing surface area coverage. The objective of this experiment is to identify analytical and numerical modeling techniques that agree to within 5% of experimental results to provide guidance in performing panel analysis with surface-mounted components. The QoIs in this experiment are box footprint (in^2) and the panel's first natural frequency (Hz).

5.1 Background and Methods

In any well-founded structural analysis, both analytical and numerical techniques must be performed and compared to build confidence that the analysis approach is correct. This section begins by reviewing the analytical methods used to estimate the first natural frequency (FNF) of simply-supported and clamped panels. These analytical methods are performed as a 'sanity

check' for comparison to results obtained using numerical methods such as finite element

analysis. The latter half of this section discusses the finite element techniques employed to

model the panel and three boxes used in this experiment.

5.1.1   Analytical Methods

The natural frequencies for a uniform, simply-supported rectangular panel are calculated as

shown below [17]:

$$f_n(c,d) = \frac{\pi}{2}\left[\left(\frac{c}{a}\right)^2 + \left(\frac{d}{b}\right)^2\right]\sqrt{\frac{D}{\gamma}} \qquad\qquad [5\text{-}1]$$
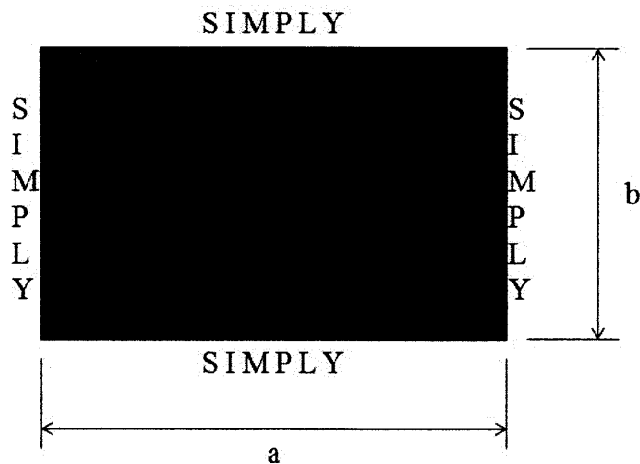
Figure 5-1: Simply-Supported Rectangular Panel

In this equation, f_n is the natural frequency; a and b are the dimensions of the plate; c and d are

positive, whole numbers corresponding to plate modes; γ is the plate's mass per unit area; and D

is the plate bending constant calculated using the formula [17]:

$$D = \frac{Et^3}{12(1-v^2)} \qquad\qquad [5\text{-}2]$$

In this equation, E is the modulus of elasticity for the plate material, t is the plate thickness, and

v is Poisson's ratio for the plate material.

Likewise, the natural frequencies for a uniform, clamped rectangular panel are calculated using [17]:

$$f_n(c,d) = \frac{\lambda_{cd}^2}{2\pi a^2}\sqrt{\frac{D}{\gamma}}$$

[5-3]
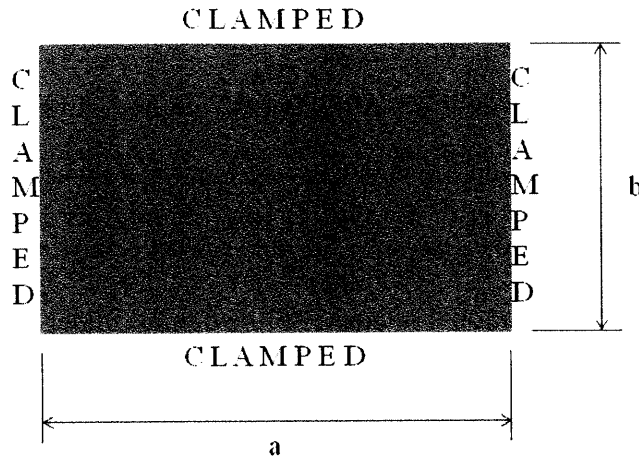
Figure 5-2: Clamped Rectangular Panel

In this formula, the terms share the same meaning as those in the simply-supported case.

One significant change is the addition of the term λ_{cd}, which is a dimensionless frequency

parameter based on the panel's rectangularity (a:b ratio) and the desired mode shape (c,d). The

value of this parameter is retrieved from Table 11-4 of *Formulas for Natural Frequency and*

Mode Shape [17].

The above analyses can be expanded to include the mass contribution of a surface-mounted

component by distributing or 'smearing' the mass across the panel's surface. Component mass

is accounted for by modifying the mass per unit area [26]:

$$\gamma_{Total} = \gamma_{Panel} + \gamma_{Component}$$

[5-4]

91

5.1.2   Numerical Methods

In addition to analytical methods, numerical approaches are employed to understand the modal response of the panel and box structure. Accuracy is the primary objective in exploring various panel-analysis scenarios, but computational efficiency is another important variable in assessing the value of numerical methods. While modern finite element tools enable the engineer to automatically mesh and analyze complex structures, the models these tools produce can quickly become a burden to even the most capable computers when combined with other complex structures in coupled-loads analyses. For this reason, a custom, simple grid is employed to minmize the computational intensity of the models under study.   The grid used for the panel in this experiment is shown in Figure 5-3.
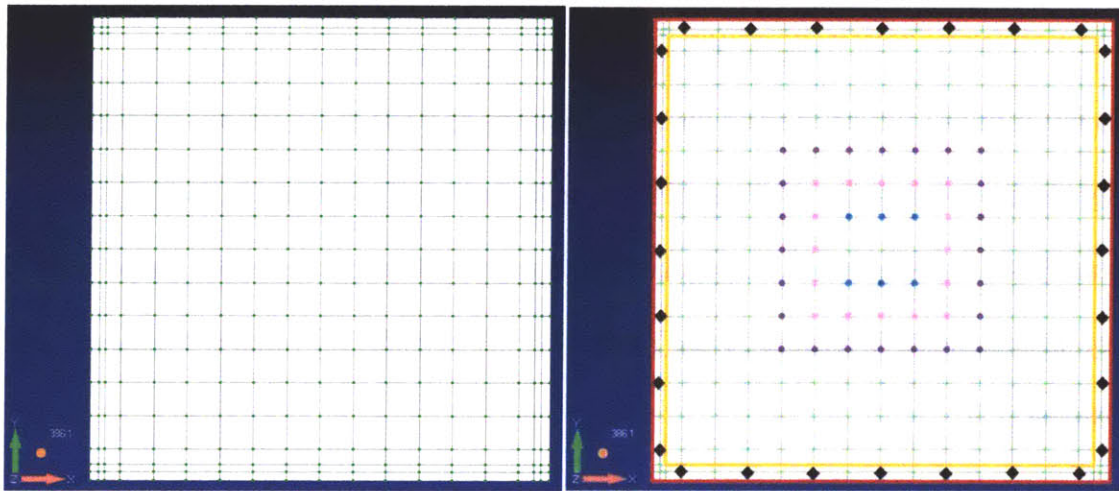
Figure 5-3: Panel Grid. LEFT: Panel Grid as seen in FEMAP. RIGHT: Panel grid indicating node locations for feature attachment. Red square – outer-perimeter of the test frame. Black diamonds – fastener locations for securing the plate to the test frame. Orange square – inner-perimeter of the test frame. Purple circles – fastener locations for the 9in x 9in box. Pink boxes – fastener locations for the 6in x 6in box. Blue circles – fastener locations for the 3in x 3in box.

The panel grid is contstructed using FEMAP v10.1.1 for pre- and post-processing activities. NEi NASTRAN v10.0 is used as the solver. The grid consists of 361 nodes connected using 324 plate elements. The fastener locations are positioned on the grid to form a 20in x 20in

square that defines the panel dimensions used in this analysis. The inner- and outer-perimeters of the test frame are also included in the panel grid to allow flexiblity in modeling test frame interactions. As seen in Figure 5-3, the test frame inner-perimeter forms a 19.4in x 19.4in square of nodes on the panel, and the outer-perimeter forms a 20.8in x 20.8in square. The nodes in the center of the panel form 1.5in x 1.5in squares to conveniently correspond with the fastener locations on the 3in x 3in, 6in x 6in, and 9in x 9in boxes.

The material properties for the plate elements are defined using the specifications for aluminum 6061-T651 as reported in MMPDS-03 [16]. Each plate element is assigned a thickness of 0.118in, which corresponds to the thickness of the actual panel. An acceleration of $386.1 \frac{in}{s^2}$ is applied along the panel's –Z axis to model the effects of gravity. While gravity does not play a role in the modal analysis, it is necessary to include gravitational acceleration for the Single Point Constraint check discussed in Section 5.3: Model Verification.

The boxes are modeled and attached to the panel using five finite element modeling techniques. These models are designated as RBE2, RBE3, CBUSH, Solid, and Extrude. The model names are derived according to the type of element employed in each analysis. Specifically, the Rigid Body Element (RBE) models are created using RBE2 and RBE3 elements to attach a concentrated mass element to the panel. The RBE2 element forms a rigid link between two nodes and functions by evenly distributing mass to dependent nodes when multiple elements are used. The RBE3 element is similar to the RBE2 element except the element is not rigid. For this reason, the RBE3 element works by distributing mass to dependent nodes while not rigidizing the structure.

Using FEMAP, the RBE2 and RBE3 models are created by placing a node at the box's center of mass located above the center of the panel. The concentrated mass property is applied to the node. RBE2 and RBE3 elements are then used to link the concentrated mass to the panel for each of the two cases. A perspective view of this arrangement is shown in Figure 5-4 for the RBE2; the RBE3 model looks identical. The RBE2 element is created by defining the concentrated mass as the independent node. This node is locked in all translational and rotational degrees of freedom with respect to the element's local coordinate system, and the dependent nodes are nodes on the panel where fasteners would be located were the box modeled discretely. The definition of the RBE3 element is identical to that of the RBE2 except that the RBE3 frees the X, Y, and Z-translational degrees of freedom to distribute mass without stiffening the panel.
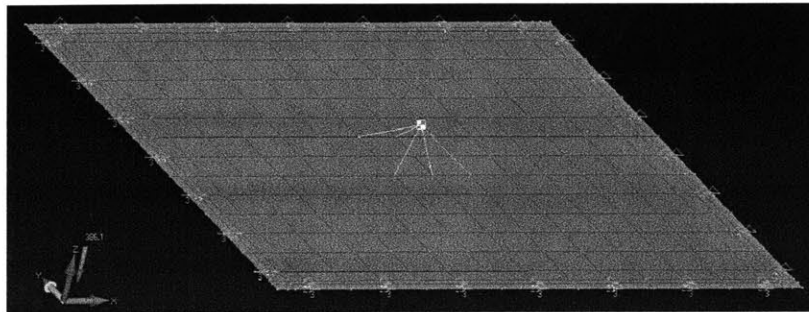
Figure 5-4: Attachment of a Concentrated Mass to the Panel using RBE2 Elements

The CBUSH and Solid models require the use of solid elements to model the boxes. For the Solid model, each box is constructed such that the nodes along the base of the box align with the nodes on the panel. The common nodes between the box and panel are then merged to rigidly attach the box to the panel. The height of each box is dictated by the mass of its physical counterpart, i.e. the box height is set such that the mass of the box in the simulation matches the mass of the actual box used in the experiment. Because of this methodology, the box center of mass does not match the center of mass of the actual component. This discrepancy is assumed

negligible since the panel's drumhead mode is of intest in this experiment, not the rocking mode.

Figure 5-5 illustrates these modes.
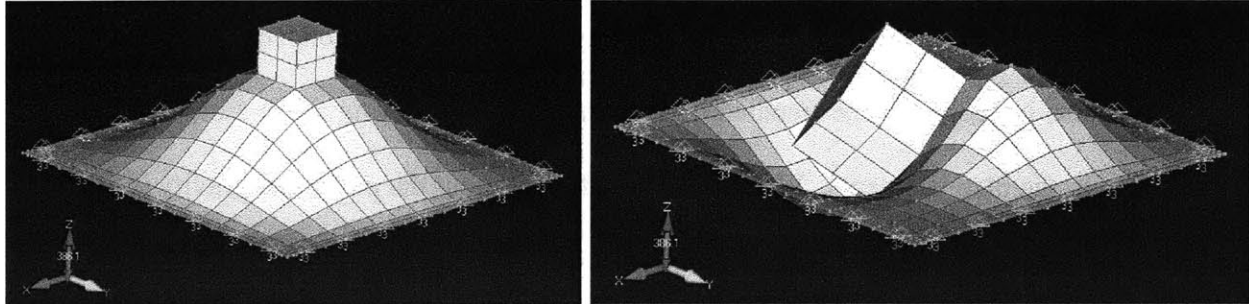
Figure 5-5: Illustration of Drumhead (LEFT) and Rocking (RIGHT) Panel Modes

The CBUSH model differs from the Solid model in that the CBUSH model uses spring/damper elements to attach the box to the panel at the presribed fastener locations. The translational stiffness of the spring/damper elements is set to $10E6 \frac{lb}{in}$ to simulate the presence of a fastener. A perspective view of the CBUSH model is shown in Figure 5-6.
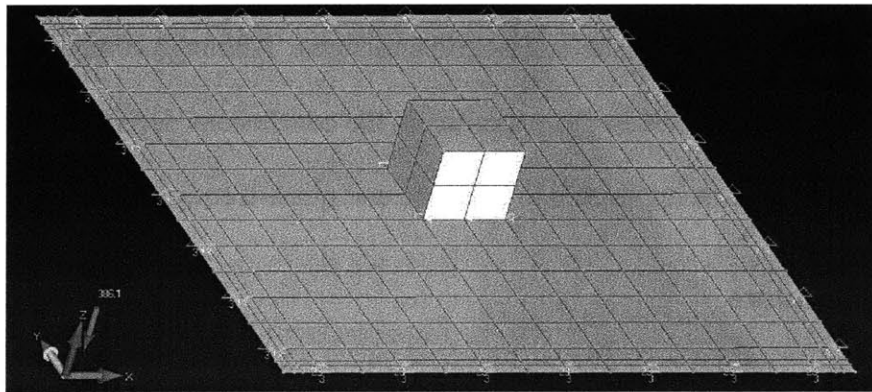
Figure 5-6: Solid 3in x 3in Box Attached to the Panel using CBUSH Elements

The fifth modeling technique investigated in this experiment is the Extrude model. The Extrude model is created by increasing the thickness of the plate elements that would be covered by the footprint of the box. The element thickness is increased to account for both the mass of

the panel and the box. The Extrude model 'extrudes' the box equally from both faces of the panel to maintain the center of mass in the plane of the panel.

In addition to the aforementioned numerical analyses, smeared and concentrated mass analyses are also performed. The smeared mass is modeled by applying a non-structural mass per unit area to the plate elements. When distributed throughout the panel and gravity is applied, this non-structural mass applies a force equal to that of the box. Likewise, to model the concentrated mass, a concentrated mass element is defined and applied to the center of the panel.

5.2 Hardware and Experimental Procedures

The panel in this experiment is intentionally sized to represent a panel that could be found on a small ESPA-class satellite. ESPA standards dictate that the satellite must have a fundamental frequency above 35 Hz and must not exceed external dimensions of 24in x 28in x 38in [4]. A solid panel is used to minimize the introduction of error and complexity associated with the machining and assembly of composite and isogrid structures. Although composite and isogrid structures are not explicitly tested in this experiment, the conclusions derived from this experiment are assumed to be applicable to isotropic and quasi-isotropic structures.

5.2.1 Test Hardware

The panel, boxes, and test frame used in this experiment are shown in Figure 5-7 through Figure 5-9. Renderings of the panel and box CAD models are provided in Appendix I. Despite the panel's physical dimensions of 20.8in x 20.8in, the 20in x 20in square formed by the fastener holes is used to define the 20in x 20in panel considered in this experiment. The same methodology is applied to the boxes whose bolt hole patterns are used to define the 3in x 3in, 6in

x 6in, and 9in x 9in footprints on the panel. The panel is secured to the test frame using #10 fasteners spaced at 3in intervals along the edges of the panel.

In Figure 5-8, note that the 3in x 3in box has only two flanges for fastening to the panel, while the 6in x 6in and 9in x 9in boxes have four flanges around their outer-perimeters. The two faces of the 3in x 3in box that would have flanges are left as solid aluminum to make the small box as massive as possible. This added mass ensures a more measurable impact on the panel's modal response. Additionally, it is industry standard practice to fasten small boxes along only two flanges [30]. All boxes are secured to the panel using #10 fasteners spaced at 1.5in intervals along the box edges.
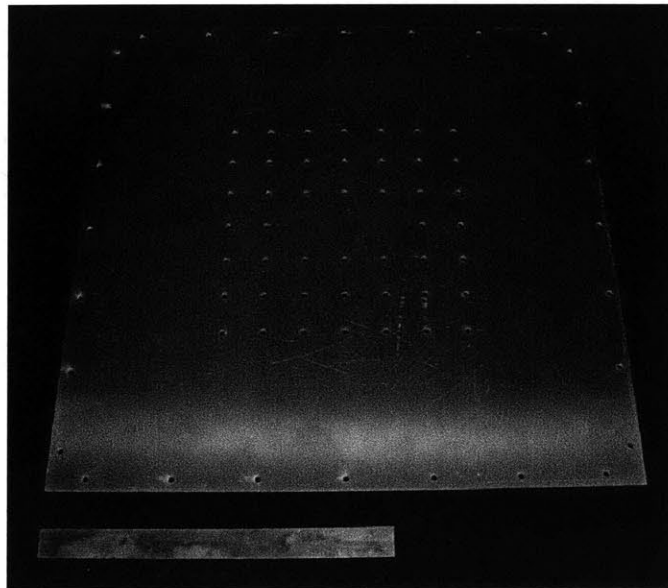
Figure 5-7: 20in x 20in Panel. Note that the 20in x 20in dimensions mark the bolt hole centers around the perimeter of the panel.
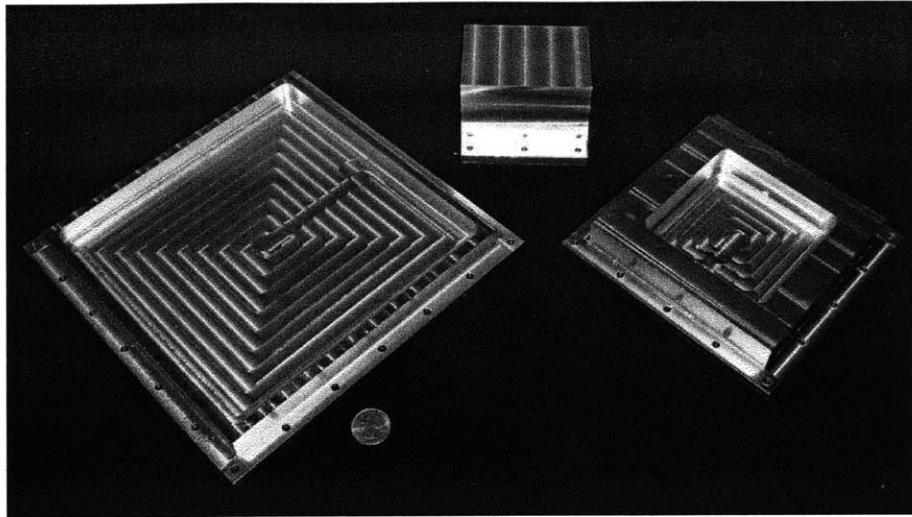
Figure 5-8: Box Simulators. 9in x 9in box (LEFT), 3in x 3in box (CENTER), 6in x 6in box (RIGHT). Note that the prescribed dimensions mark the bolt hole centers around the perimeter of the boxes.
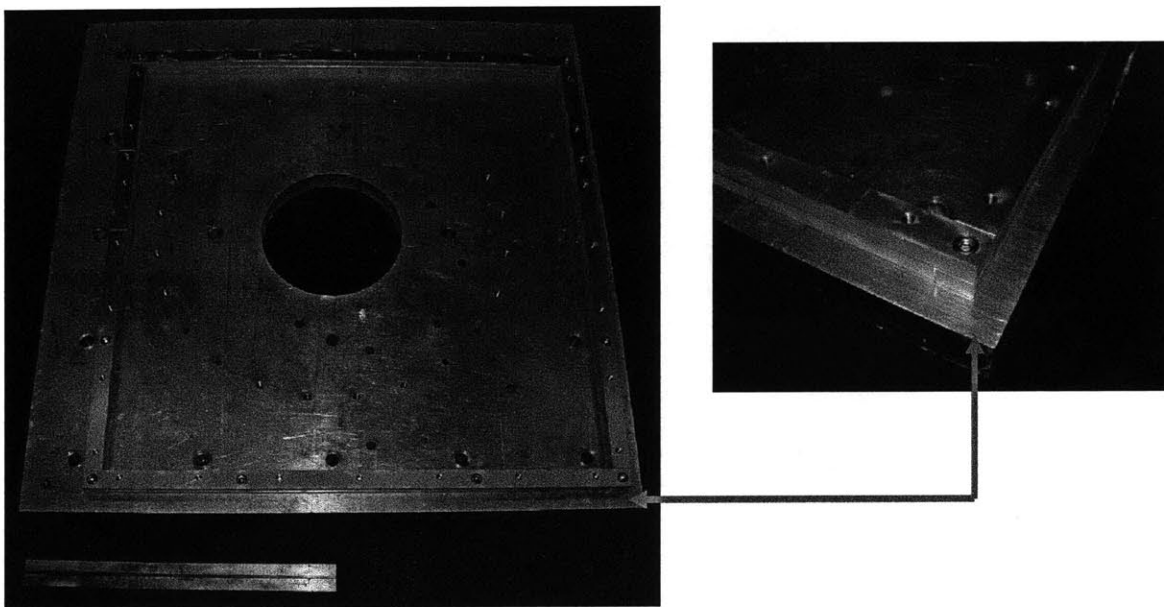
Figure 5-9: Rigid Test Frame with Corner Call-Out to Illustrate Assembly

The panel and box masses are summarized in Table 5-1. Since the objective of this experiment is to determine the consequence of box stiffening on the panel's first mode, the boxes were designed and fabricated to have approximately equal mass. Once the boxes were fabricated, fastener mass along with differences in machining accounted for a 10.8% difference in mass between the 3in x 3in and 9in x 9in boxes. The mass of the 6in x 6in box was between

the 3in x 3in and 9in x 9in boxes. The differences in masses are accounted for by incorporating the mass of the actual boxes into the analytical solutions and finite models, but it is useful for this experiment to quantify the ramifications of these differences. The panel's modal sensitivity to the difference in box masses is calculated by comparing the FNF's found by modifying the concentrated-mass finite element model to match the 3in x 3in and 9in x 9in boxes. The resulting FNF's are 46.2Hz for the 3in x 3in box at 2.325lb and 44.4Hz for the 9in x 9in box at 2.577lb. In conclusion, the sensitivity analysis reveals that the 10.8% increase in mass results in a 4.2% decrease in FNF.

Table 5-1: Panel and Box Weights at 1G $\left(386.1\frac{in}{s^2}\right)$

Component	Weight (lb)	Fastener Weight (lb)	Total Weight (lb)
Panel	5.033	N/A	5.033
3in x 3in Box	2.248	0.077	2.325
6in x 6in Box	2.216	0.236	2.452
9in x 9in Box	2.222	0.355	2.577

5.2.2   Assumptions

Two key assumptions are made to simplify this experiment. First, it is assumed that the differences in the boxes vertical center of mass are negligible since the mode shape of interest is the panel's drumhead mode, and not a rocking mode. Second, the boxes are assumed to be effectively rigid when compared to the panel. This assumption is to preclude the introduction of an additional drumhead mode in the box that would result in a non-linear modal response.

To ensure the second assumption is correct, the 9in x 9in box is analyzed as the worst-case scenario as it has the largest footprint (9in x 9in) and the thinnest base plate (0.2in). The stiffness contributed by the box's sidewalls is neglected to simplify the FNF calculation and provide further confidence that the box is effectively rigid compared to the panel. Applying the analytical techniques discussed in Section 5.1.1, the 9in x 9in box's first natural frequency is

99

531Hz assuming a simply supported boundary condition and 854Hz assuming a clamped boundary condition. As will be observed in the results section, these respective estimates are 5.6 and 9.0 times the panel's experimentally-determined FNF of 94Hz. Because the 9in x 9in box's FNF is much greater than that of the panel, the 9in x 9in box as well as the 6in x 6in and 3in x 3in boxes are considered to be rigid.

5.2.3   Test Setup and Procedures

After fabrication and inspection, the panel is instrumented and mounted to the test frame. The first test has no box attached to the panel and is the baseline case to determine the panel's FNF for comparison to the analytical and numerical predictions. The configuration shown in

Figure 5-10 depicts this baseline case. The panel's FNF is determined in this experiment using the modally tuned impulse hammer kit (PCB Piezotronics Model GK291D01) for instrumentation. Data acquisition is performed using an Agilent Technologies DSO 1004A oscilloscope and a Lenovo W500 laptop computer. An accelerometer is mounted in the center of the –Z face of the panel. This is done to accommodate the attachment of the boxes to the panel's +Z face. The #10 bolts along the panel perimeter are torqued to 25in-lb and the panel is struck with the modal impact hammer. The accelerometer's output in G's is recorded for later data reduction. This procedure is repeated for each box size. The boxes are attached to the panel using #10 fasteners, which are also torqued to 25in-lb.

Through exhaustive experimentation, it was determined that the panel's frequency response is the same regardless of whether (1) the box is struck or (2) the panel is struck immediately beside the box (reference Section 5.4: Results). For the purposes of consistency, each box was struck on center, and four cycles were measured for each box.
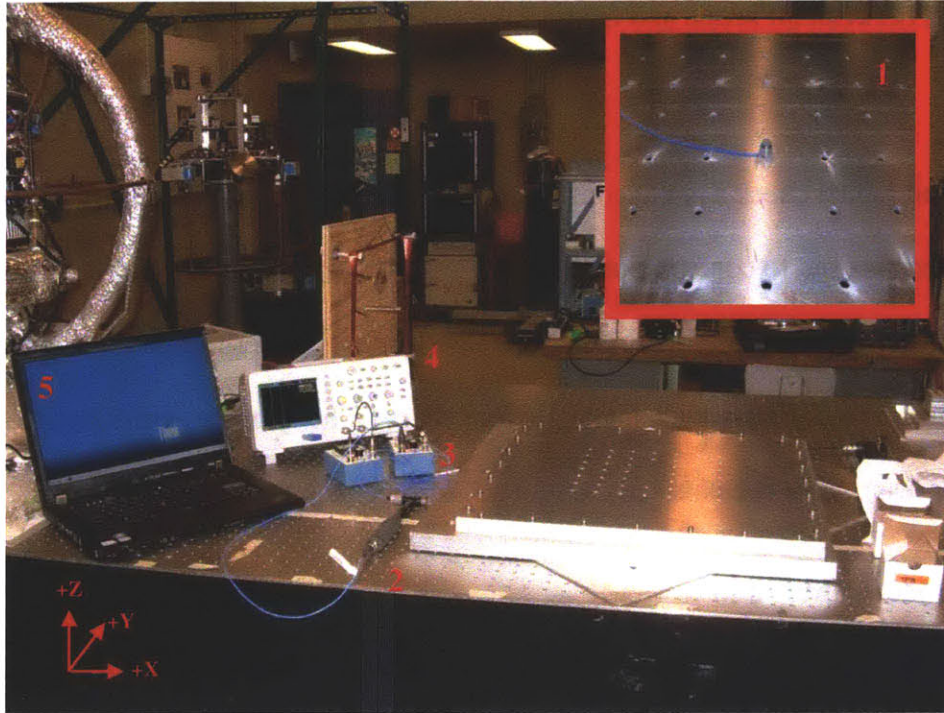
Figure 5-10: Test Setup. Panel mounted on test frame with no box attached. Accelerometer (1) is mounted on the backside (-Z face) of the panel to allow for box attachment to the topside (+Z face) of the panel. Also shown are the impact hammer with load cell (2), signal conditioners (3), oscilloscope (4), and laptop (5) for data acquisition. The accelerometer is centered on backside of the panel to permit box attachment atop the panel.

5.3 Model Verification and Calibration

5.3.1   Model Verification

Two tests are performed on each finite element model prior to running the modal analyses for the desired panel-box configuration. The first model check is called the Single Point Constraint (SPC) check. This check is performed to ensure the correct material properties and geometry are reflected in each model. The SPC test compares the masses of the actual panel and boxes to the masses represented in the models by summing the loads observed at the nodal constraints along the perimeter of the panel when a 1G $\left(386.1\frac{in}{s^2}\right)$ acceleration is applied along the panel's –Z axis. The results of the SPC check are summarized in Table J-1 located in Appendix J. Since

the difference between all actual and model weights is less than 1%, all models pass the SPC check.

The second model check is an unconstrained modal analysis called the Free-Free check. The Free-Free check is used to confirm that the panel and box have no unintended constraints. This check is implemented by suppressing the constraints around the perimeter of the panel. The Free-Free check is satisfied when the panel's first six rigid-body modes are effectively zero (10E-6 Hz or less). This check is satisfied for each of the panel models.

5.3.2 Model Calibration

This experiment was originally designed to test a simply-supported 20in x 20in panel of 0.125in thickness with a first mode of approximately 60Hz. Following fabrication, the analytical calculations and finite element models were updated to reflect the actual panel thickness of 0.118in. As shown in Appendix I and confirmed using finite element analysis, the calculation of the first fundamental frequency of the simply-supported panel is 56 Hz, or 40% error from the experimentally-determined fundamental frequency of 94 Hz. In an effort to reduce this error, the clamped boundary condition is considered. This calculation is also shown in Appendix K, and predicts a fundamental frequency of 102 Hz, or 8.5% error. Given that the panel is neither simply-supported nor perfectly clamped, it is reasonable that the actual panel's fundamental frequency exists between the two analytical results. The clamped boundary condition is a reasonably good estimate of the actual panel, but using the clamped estimate in practice is discouraged as it is a non-conservative estimate that exceeds the actual panel's FNF.

To achieve the desired 5% accuracy, the analytical results suggest that the simply supported and clamped boundary conditions are inadequate to accurately predict the panel's fundamental

frequency. For this reason, a trade study is conducted considering various boundary conditions in an effort to match as closely as possible the fundamental frequency of the model with that of the actual panel. The results of this trade study are summarized in Table 5-2. This table is organized according to (1) the boundary condition at the fasteners securing the panel to the test frame (i.e. the "Fastener BC" columns) and (2) the Z-axis translational boundary condition assigned along the inner and outer perimeters (i.e. the "Clamped Z-Axis Translation" columns). A pictorial representation of the individual boundary conditions is provided in Appendix L. While not every possible boundary condition is considered, the study is sufficiently exhaustive to allow identification of a boundary condition that matches the experimental result to within 1.1%. The boundary condition providing this accuracy is highlighted in Table 5-2 and is shown in Figure 5-11. This boundary condition consists of simply-supported fasteners paired with alternating Z-translation constraints along the panel's outer perimeter.

Table 5-2: Boundary Condition Trade Study Results

| Fastener BC | | Z-Axis Translation Constraint | | | | FNF (Hz) | % Diff from 94 Hz (%) |
| | | Outer-Perimeter BC | | Inner-Perimeter BC | | | |
Simply Supported	Clamped	Alternating Nodes	All Nodes	Alternating Nodes	All Nodes		
X						56.9	40
X		X				95.4	1.1
X			X			97.5	3.3
X				X		103.7	9.9
X					X	104.1	10
X		X		X		103.8	10
X		X			X	104.1	10
X			X	X		104.3	11
X			X		X	105.2	11
	X					97.8	3.6
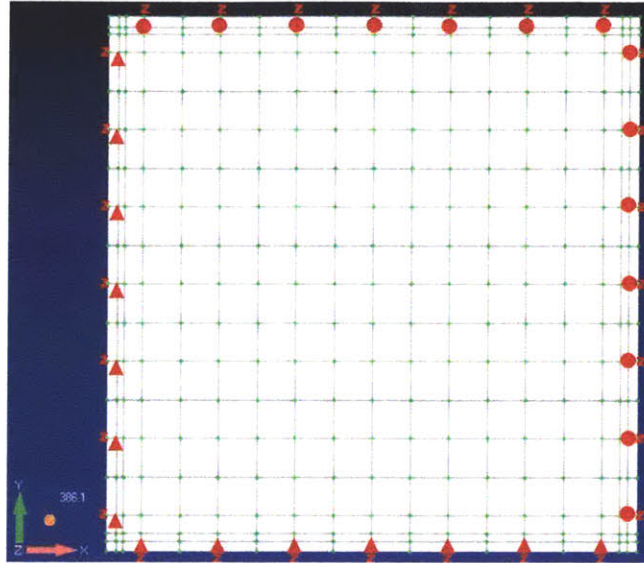
Figure 5-11: Panel Boundary Condition Selected from Trade Study: Simply-Supported Fasteners Paired with Alternating Z-translation Constraints along the Panel's Outer-Perimeter

5.4 Results and Error Analysis

5.4.1   Results

In accordance with the defined experimental procedures, the panel and three boxes were tested using a modally tuned impulse hammer kit. The test setup and corresponding frequency response plots are shown in the figures on the following page. In the response plots, the green line is the impulse provided by the hammer, and the yellow line is the panel response.
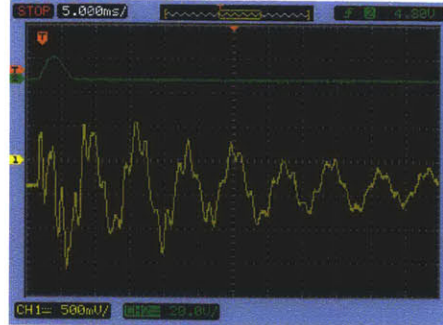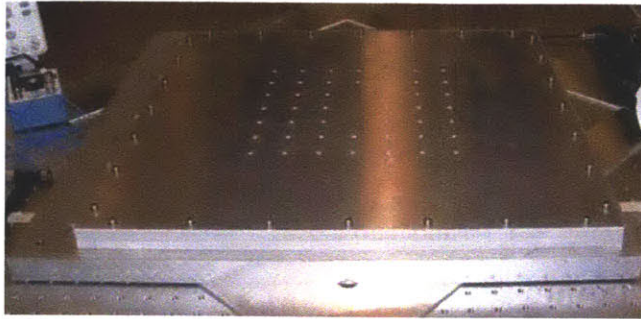
Figure 5-12: Panel (LEFT) and Corresponding Frequency Response Plot (RIGHT).
FNF = 94 Hz.
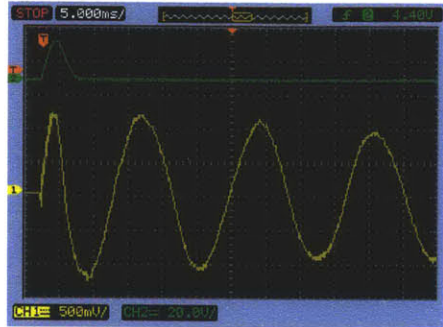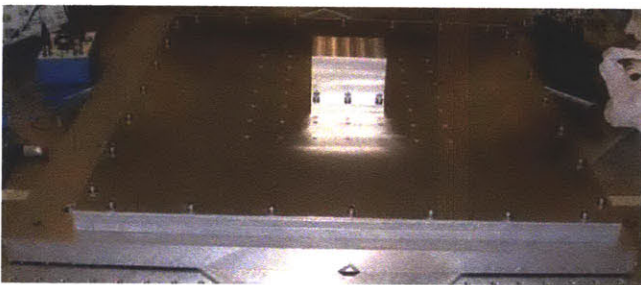
Figure 5-13: Panel with 3in x 3in Box (LT) and Corresponding Frequency Response Plot (RT).
FNF = 59 Hz.
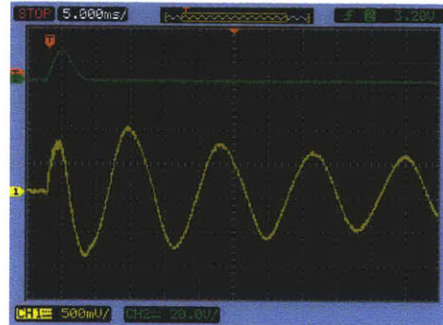
Figure 5-14: Panel with 6in x 6in Box (LT) and Corresponding Frequency Response Plot (RT).
FNF = 75 Hz.
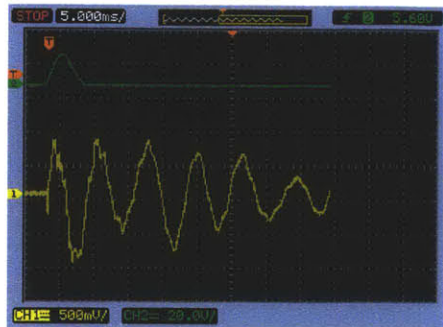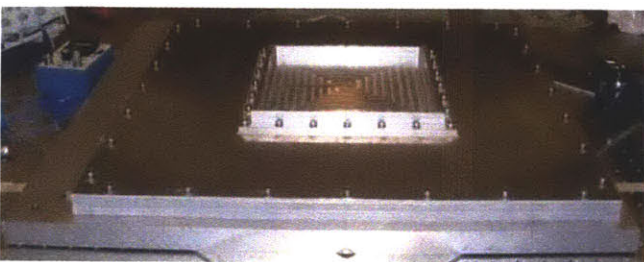
Figure 5-15: Panel with 9in x 9in Box (LT) and Corresponding Frequency Response Plot (RT).
FNF = 143 Hz.

After satisfying both model checks and calibrating the finite element model to match the panel's experimentally-determined FNF, modal analysis is performed for each box size using the five plate-box modeling techniques discussed in the Background and Methods section. The results of these analyses are summarized in Figure 5-16 and Table 5-3.
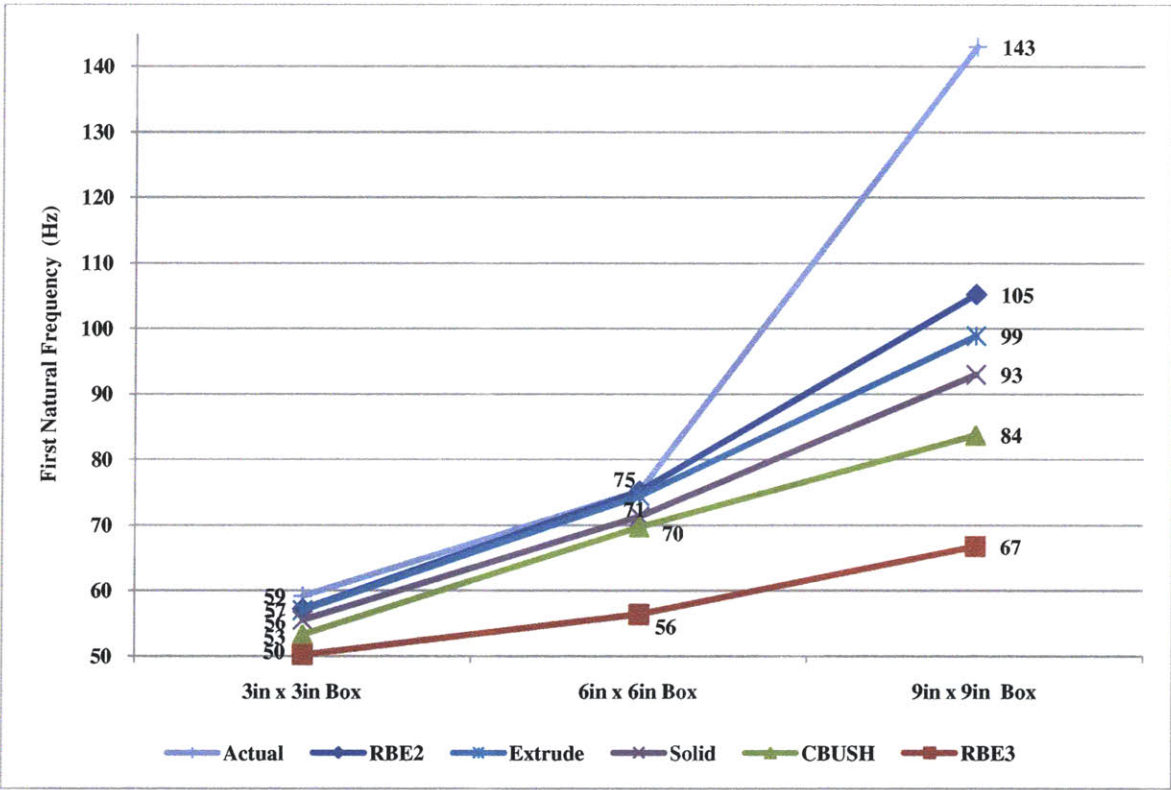
Figure 5-16: Panel Mode as a Function of Box Size and Modeling Method

Table 5-3: Predicted Panel FNF and Percent Difference from Actual FNF

	3in x 3in Box		6in x 6in Box		9in x 9in Box	
	FNF (Hz)	% Diff from 59 Hz (%)	FNF (Hz)	% Diff from 75 Hz (%)	FNF (Hz)	% Diff from 143 Hz (%)
RBE2	57.2	3.1	75.2	0.25	105.2	26.4
Extrude	57.0	3.4	74.5	0.68	98.9	30.8
Solid	55.5	5.9	71.3	4.9	93.0	35.0
CBUSH	53.3	9.7	69.7	7.1	83.7	41.4
RBE3	50.2	14	56.4	25	66.8	53.3

5.4.2   Error Analysis

Upon first observation, it is evident that three of the models- RBE2, Extrude, and Solid- are within the desired 5% accuracy for the 3in x 3in and 6in x 6in boxes, but all five models quickly diverge from truth once the box footprint grows to 9in x 9in. To understand this occurrence, further investigation is required with an emphasis on the RBE2 element, which consistently provides the closest approximation of the actual panel.

The views in Figure 5-17 show an exaggerated view at maximum deflection of the panel with the 9in x 9in box attached using RBE2 elements. The FNF of the panel in Figure 5-17 is 95.4Hz (33% difference from 143Hz). This view illustrates that the RBE2 elements do not rigidize across the box footprint as would be expected when the panel deforms in the +Z direction. This view indicates that while the RBE2 elements provide rigid connections to the fastener locations, the model does not take into account the interference condition between the box and plate. Considering the panel's motion over one cycle helps clarify this scenario. When the plate deflects in the –Z axis, the deformation should be similar that shown in Figure 5-17. However, when the plate deflects along the +Z axis, the rigid box should prevent deflection at the center of the panel as seen in Figure 5-18. In this scenario, the panel FNF is 105.4Hz (27% difference from 143Hz). The boundary condition used to create the model shown in Figure 5-18 is created by connecting all nodes shared across the footprint of the 9in x 9in box to the panel using RBE2 elements. The interaction just described is non-linear and is not accurately captured by either of the models shown in Figure 5-17 or Figure 5-18.
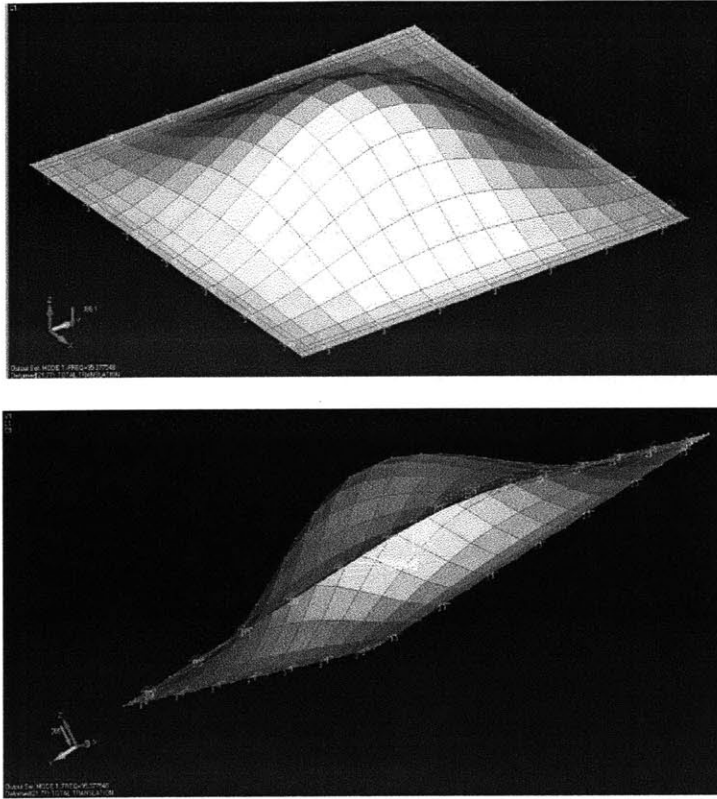
Figure 5-17: Deformed Panel with 9in x 9in Box Attached at Fastener Locations Using RBE2 Elements
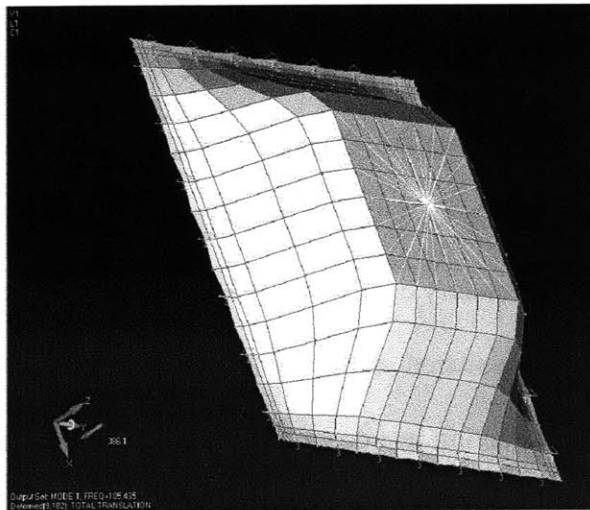
Figure 5-18: Deformed Panel with 9in x 9in Box Attached Using RBE2 Elements Across Entire Box Footprint

In an effort to recalibrate the panel model, a trade study was conducted. The most

conservative boundary condition possible was imposed on the model by (1) connecting all nodes

108

shared across the footprint of the 9in x 9in box to the panel using RBE2 elements and by (2) constraining the panel in all axes in both translation and rotation (i.e. clamping the boundary condition) along the inner-perimeter of the interface between the panel and test frame. As shown in Figure 5-19, these boundary conditions elevated the predicted FNF to 134.8Hz, which is 5.6% less than the actual FNF of 143Hz.
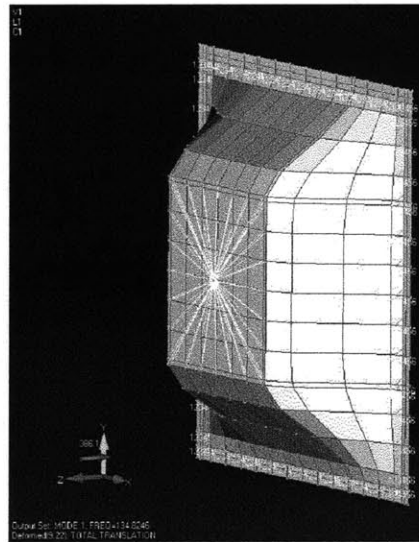
Figure 5-19: Deformed View of Panel Clamped Along Inner-Perimeter with RBE2 Elements connecting 9in x 9in Box Across Entire Footprint

In a final effort to understand the non-linearities of the panel with a 9in x 9in box attached, a detailed study of the panel dynamics was conducted. The panel was struck in five different locations as summarized in Figure 5-20 and Table 5-4. A total of eighty-three cycles were measured producing an average FNF of 143Hz with a standard deviation of 9.6Hz. This analysis is useful in that it increases confidence that (1) the panel FNF is in fact dramatically higher than predicted by the models and (2) the panel is relatively insensitive to the location at which it is struck. Interestingly, note that while the overall average remains relatively unchanged, the standard deviation is consistently higher when the hammer strike is applied off-center. This is

likely explained by the increased excitation of higher-order modes resulting in locally-shifted peak locations for the dominant first mode.
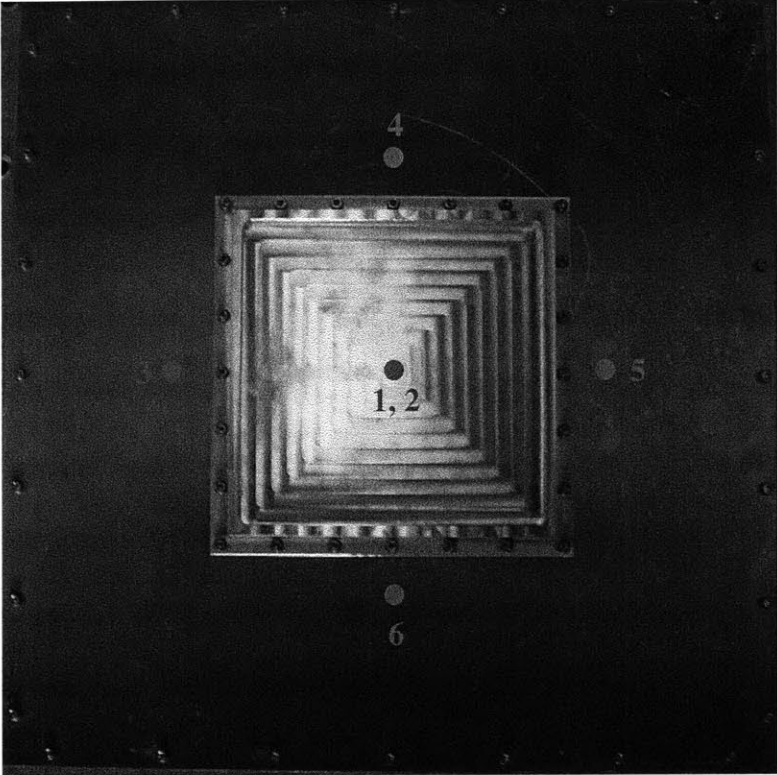
Figure 5-20: Panel Strike Zones with 9in x 9in Box Attached

Table 5-4: Statistical Summary of Strike Zone Test

Strike Zone	# Cycles (#)	Avg FNF (Hz)	Stnd Dev (Hz)
1	13	141	3.5
2	15	142	3.1
3	12	144	8.8
4	11	144	10.8
5	14	141	9.2
6	18	144	15.4
Overall	83	143	9.6

5.5 Conclusions

The objective of this experiment was to identify analytical and numerical modeling techniques that agree to within 5% of experimental results. These findings provide guidance in performing modal analysis for a panel with rigid, surface-mounted components. This objective was achieved by conducting an experiment using an isotropic panel and three boxes of approximately equal mass but varying surface coverage and comparing experimental results to analytical and numerical solutions. The QoIs in this experiment were panel FNF and component footprint. Understanding the relationship between these QoIs is both important and challenging due to the dynamic trade between component mass and surface area; increasing mass drives a decrease in the panel's FNF, while the added stiffness gained by increasing component surface coverage increases FNF.

The key findings of this experiment are summarized as follows:

- With the exception of the analytical solution for the clamped boundary condition, all analytical and numerical modeling techniques considered in this experiment provided a conservative estimate of the panel's FNF.

- Although non-conservative, the clamped analytical solution provided a closer estimate of the panel's FNF than did the simply supported solution for the boundary conditions used this experiment.

- Using the calibrated panel and modeling the box as a concentrated mass attached with RBE2 elements is an accurate and computationally efficient method for modeling box-panel interactions when:

  1. The box is approximately centered on the panel.

2. The box and panel are approximately square.

3. The box covers less than or equal to approximately 9% of the panel's surface (i.e. the 6in x 6in box covers 9% of the 20in x 20in panel).

- Beyond approximately 9% panel coverage, non-linearities between the panel and box require a higher-fidelity model that is preferably accompanied by test data.

Future work to build on this experiment should begin by further exploring the non-linear relationship between box mass and surface coverage that exists beyond 9% panel coverage. In addition, expanding the experiment's quantities of interest to also include mass would help to more fully characterize this design problem. In completing this parameter sweep, it would be highly useful to continue to identify conditions under which analytical solutions are valid. Lastly, confirming the assumption that this analysis applies to all isotropic square plates by testing both isogrid and composite structures would help to expand the confidence and utility of this experiment to modern aerospace structures.

Chapter 6 - Conclusion and Future Work

6.1 Thesis Summary

In response to persistent cost and schedule overruns, stochastic process decision methods are a radically different approach for managing the development of complex systems. The stochastic process view of system development considers uncertainty as the greatest threat to achieving project objectives. Uncertainty is captured numerically by identifying and measuring the QoIs that drive system performance. QoI quantification enables application of stochastic processes to estimate the overall state of system development. This knowledge enables technology developers to identify and strategically reduce the greatest contributors of uncertainty, thereby achieving improved cost and schedule performance.

The primary objective of this thesis is to provide a basis for testing and applying stochastic process decision methods to real systems. Additional objectives of this thesis are to document the preliminary design of the REXIS x-ray spectrometer and present the findings of a structural dynamics experiment. Chapter 3 and the discussion of the CASTOR satellite provides an example for identifying QoIs and performing basic uncertainty analysis. In chapter 4, the REXIS preliminary design is organized in preparation for applying stochastic process methods to system development, and the structural dynamics experiment in chapter 5 illustrates several analysis techniques commonly employed to evaluate the impact of QoIs on system performance.

6.2 Contributions

This thesis defines the Quantity of Interest and contains the necessary data and analysis for testing stochastic process decision methods on real systems. Using the historical development of the CASTOR satellite, this thesis enables the transition from theory to application to test the utility of stochastic process decision methods on a real system. Furthermore, this thesis serves as the design document for the REXIS x-ray spectrometer. Through the analysis contained in chapter four, future students and faculty on the REXIS team are equipped with the most current knowledge of the REXIS design as of May 2011 in preparation for detailed design efforts beginning in fall 2011. Lastly, the structural dynamics experiment in this thesis provides guidance to spacecraft structural engineers on the appropriate methods for modeling the modal effects of a center-mounted component on an isotropic plate as is commonly encountered in spacecraft design.

6.3 Future Work

Stochastic process decision methods offer great potential for enhancing complex system development. The success of stochastic processes will to a great extent be determined by ability to translate high-level theory into a widely-applicable framework. The next step in advancing stochastic process decision methods is to transition beyond retrospective analyses and begin applying these methods to real systems actively under development. REXIS, and to a limited extent, CASTOR, offer this needed opportunity. The CASTOR and REXIS student projects provide a low-risk opportunity to collect data in-situ, impose changes based on model estimates, and measure the effects of changes on system uncertainty. The critical element required for success is to maintain consistent feedback from the various program subsystems to ensure accurate state estimation is achieved.

References

[1] "META-II Broad Agency Announcement." Arlington: DARPA, Apr. 2010. pg. 4.

[2] "Defence spending in a time of austerity." *The Economist*. 26 Aug. 2010.
<http://www.economist.com/node/16886851>.

[3] Buede, Dennis. *The Engineering Design of Systems*. Fairfax: John Wiley & Sons, 2000.

[4] Brill, James. "Systems Engineering – A Retrospective View." *Systems Engineering*: Vol. 1,
No. 4. pp. 258-266.

[5] Weigel, Annalisa. "Engineering and Politics in Space Systems: Developing a more
integrated view." MIT. ESD.83 Course Notes. Fall 2000.

[6] Allaire, Douglas, Karen Willcox, and John Deyst. "On the Application of Estimation
Theory to Complex System Design Under Uncertainty." SIAM Conference on
Computational Science and Engineering. Reno. 1 Mar. 2011.

[7] Deyst, John. "The Application of Estimation Theory to Managing Risk in Product
Developments." IEEE. Jul. 2002.

[8] Mansuripur, Masud. Introduction to Information Theory. New Jersey: Prentice Hall, 1987.
pg. 13.

[9] Zschornack, Günter. *Handbook of X-Ray Data*. Berlin: Springer-Verlag, 2007.

[10] "OSIRIS-REx Design Reference Mission." University of Arizona. 11-13 May 2010.

[11] "OSIRIS-REx: A New Frontiers Proposal." University of Arizona. NASA. Slide 7.

[12] "OSIRIS-REx Spacecraft." Lockheed Martin Corporation. Dec. 2010.

[13] Boehm et al. COCOMO II: MODEL DEFINITION. Chapter 2. University of Southern
California, 2000. pp. 48-68.

[14] "Nanosat-6 User's Guide." University Nanosat-6 Program, 2009. pg. 42.

[15] "Secondary Payload Planner's Guide For Use On The EELV Secondary Payload Adapter."
DoD Space Test Program, 2006. pg. 12.

[16] *Metallic Materials Properties Development and Standardization* (MMPDS-03). Federal
Aviation Administration, 2006. pg. 3-306.

[17] Blevins, Robert. *Formulas for Natural Frequency and Mode Shape*. New York: Krieger
Publishing Company, 1979. pp. 252-261.

[18] "FR-4." Wikipedia, 26 Jan. 2011. Accessed: 24 Feb. 2011.
<http://en.wikipedia.org/wiki/FR-4>.

[19] "G10 FR4 Technical Specifications." JJ Orly, 2009. Accessed: 24 Feb. 2011.
<http://www.jjorly.com/g10_fr4_technical_specifications_data.htm>.

[20] "NASA OSIRIS-REx Student Collaboration Experiment." University of Arizona, 30 Mar. 2010.

[21] Busboom, A., H. Elders-Boll, and H. D. Schotten. "Uniformly Redundant Arrays."
Experimental Astronomy 8, 1998. pp. 97-123.

[22] Keith C. Gendreau. "X-ray CCDs for Space Applications: Calibration, Radiation Hardness and Use for Measuring the Spectrum of the Cosmic X-ray Background." MIT PhD Thesis, 1995.

[23] M. Bautz, S. Kissel, B. LaMarr and G. Prigozhin. "Back-illuminated CCDs for Astro-E2 XIS?" 10 Mar. 2004.

[24] Boone, Katy. "Suzaku." 30 Dec. 2010. Accessed: 19 Apr. 2011.
<http://www.nasa.gov/mission_pages/astro-e2/main/index.html>.

[25] HoneyBee Robotics, 20 Feb 2011. Accessed: 20 Feb 2011.
<http://www.honeybeerobotics.com/index.php>.

[26] Sarafin, Thomas. *Spacecraft Structures and Mechanisms*. Torrance, CA: Microcosm Inc., 1995. pp. 217-218.

[27] Devore, Jay L. *Probability and Statistics for Engineering and the Sciences*. 6th Ed. Belmont, CA: Brooks/Cole, 2004. pg. 135.

[28] Madachy, Ray. COCOMO II – Constructive Cost Model Online Calculator. Naval Post Graduate School. Accessed: 6 Dec. 2010. <http://csse.usc.edu/tools/COCOMOII.php>.

[29] "Secondary Payload Planner's Guide for use on the EELV Secondary Payload Adapter." DoD Space Test Program. Jul. 2006. pp. 6-12.

[30] Doukas, Peter. Personal Interview. 20 Jul. 2010.

[31] Wertz, James, and Wiley Larson. *Space Mission Analysis and Design*. Hawthorne: Microcosm, 1999. pg. 432.

Appendix A - N-Squared Diagram Component Information

Solar Flux- Mean solar flux is $1{,}367\frac{W}{m^2}$. Solar flux varies between $1{,}322\frac{W}{m^2}$ and $1{,}414\frac{W}{m^2}$ (±3.4%) based on Earth's distance from the sun [31].

Solar Panels- Uncertainty is estimated at -50% based on previous test data. In this test, the team's solar panel produced only 50% of the anticipated power. The team is currently investigating alternative methods to assemble the solar panel to minimize inefficiencies.

Maximum Peak Power Tracker (MPPT)- SunSaver MPPT by Morningstar Corporation

- Voltage is set by battery voltage: 20-36V
- Max Current: ≤15A
- Efficiency: 91% to 97.5%
- Spec Sheet: http://www.morningstarcorp.com/en/support/library/SSMPPT_ENG7_10.pdf

Power Propulsion Unit (PPU)- Two Converters and one BuckPuck

1) Converter: 24V to 15V by Vicor

- Voltage Accuracy: ±1%
- Max Current: ≤8.67A
- Efficiency: ≤89%
- Spec Sheet: http://cdn.vicorpower.com/documents/datasheets/ds_24vin-micro-family.pdf

2) 24V to 200V by American Power Design

- Voltage Accuracy: ±4%
- Max Current: ≤750mA
- Efficiency: ≤90%
- Spec Sheet: http://www.apowerdesign.com/pdf/h150.pdf

3) 500mA BuckPuck by LEDdynamics

- Current Accuracy: ±5%
- Voltage: 6-32V
- Efficiency: ≤95%
- Spec Sheet: http://www.ledsupply.com/03021-d-i-500.php

Tank- Luxfor L45J

- Knowledge of tank pressure to ±1% at fill and ±3% on orbit is an assumption
- Service Pressure: 4500psi (Maximum)
- Spec Sheet:
  http://www.luxfercylinders.com/products/lifesupport/specifications/us_imperial.shtml

Regulator- UPR1 by GO Regulators

- ±10% accuracy is an assumption
- Spec Sheet: http://www.goreg.com/products/regulators/single/pr1/index.htm

Flow Controllers (Flow Cntrls)- FMA3204ST by Omega

- Power Rqmt: 12-15V @ 230mA
- Rated Flow: 0.4 to 20 sccm
- Flow Accuracy: ±1% within (10 to 100% rated flow)
- Spec Sheet: http://www.omega.com/manuals/manualpdf/M4271.pdf

Cathode- Produced by Busek

- Voltage Range: 20-36V
- Current: 0.5A

Anode- Custom MIT Space Propulsion Lab design

- Voltage Range: 46-300V
- Current: 0.36A

Thrust- Two sources of uncertainty

- Accuracy of the thrust balance in the vacuum chamber: ±10%
- Thrust produced by the experimental thruster: -30%
- Both of the above estimates are assumptions. The thrust balance uncertainty is a Gaussian distribution. The thrust uncertainty is one-sided as the current thrust estimates are derived from theoretical performance under ideal conditions.

Appendix B - REXIS Proposal

REXIS – Regolith X-ray Imaging Spectrometer

Student Collaboration Experiment for OSIRIS-REx

A Joint Proposal by:

Massachusetts Institute of Technology and

The Harvard College Observatory, Harvard-Smithsonian Center for Astrophysics

Abstract

REXIS provides a significant scientific enhancement to the OSIRIS-REx mission by obtaining an X-ray (0.3-7.5 keV) global map of the elemental abundance of the asteroid 1999 RQ36, thereby providing a complementary understanding of the globally representative context of the returned sample. Because REXIS is derived from Suzaku flight heritage, REXIS fulfills its objectives with low risk. REXIS will be created through MIT's landmark Conceive, Design, Implement, and Operate (**CDIO**) student curriculum that has built and flown packages on the Shuttle and International Space Station. Over 15 semesters, more than 100 undergraduate, and more than 10 graduate students from MIT and Harvard are expected to participate in the REXIS project.

I. REXIS Science and Measurement Objectives

Sample return is the principal objective of the OSIRIS-REx mission. Maximizing the science yield from the sample analysis requires the best possible asteroid context for the returned sample. Fundamentally, we must have the best possible knowledge for the representative context of the sample and sample site(s) relative to the global surface composition of asteroid 1999 RQ36. The REXIS science objective is to complement onboard mineral mapping by adding spatially resolved elemental abundance mapping achieved through X-ray spectrometry, an objective with heritage proven by the NEAR mission to Eros.

By using a novel wide-field coded aperture imaging with a small array of 4 CCD image detectors for the measurement of 0.3-7.5 keV X-rays, REXIS will map excess concentrations (>2x with >~10-20 m size) of multiple elements (O-K, Fe-L, Mg-K, Al-K, Si-K, etc.) on the asteroid surface with a resolution of 4.3 m / pixel during Phase 5B.

II. Technical Description

IIa. REXIS Technical Approach and Implementation

REXIS is a coded aperture soft X-ray (0.3 – 7.5 keV) telescope that images X-ray fluorescence line emission produced by the interaction of solar X-rays and the solar wind with the regolith of the asteroid. Table 1 presents the physical parameters for REXIS. Images are formed with 21` resolution (4.3 m spatial resolution at a distance of 700 m). The imaging X-ray detectors are a 2 x 2 array of CCDs (CCID-41 with Suzaku-XIS heritage), each with their 1K x 1K 24μm pixels binned by a factor of 32 into 0.768 x 0.768 mm "effective" pixels. Imaging is achieved by

correlating the detected X-ray image with a 64 x 64 element random mask (1.536 mm pixels). REXIS will store each X-ray event in order to maximize the data storage usage and to minimize the risk. The pixels will be addressed in 64 x 64 bins and the 0.3 – 7.5 keV range will be covered by 5 broad bands and 11 narrow line bands. A 24 sec resolution time tag will be interleaved with the event data to account for asteroid rotation. Images will be reconstructed on the ground after downlink of the event list (individual image has a FOV of ~401 m x 401 m before co-adding). A 3D view of the instrument concept is shown in Figure 1. Images are formed simultaneously in 16 energy bands centered on the dominant lines of abundant surface elements from O-K (0.5 keV) to Fe-Kβ (7 keV) as well the representative continuum. During phase 5B of the OSIRIS-REx mission, 21 day orbit 700 m from the surface of asteroid, a minimum of approximately 133 events/asteroid pixel/energy bin are expected on average; enough to obtain significant constraints on element abundances at scales larger than 10 m (Figure 2).

The REXIS investigation would benefit from the inclusion of a small solar Si-PIN X-ray sensor such as has accompanied X-ray experiments on the SMART-1 and MESSENGER missions. Preliminary investigation indicates that this is likely to be feasible with currently available resources but detailed design and accommodation of such a device would be the subject of a Phase B study.

Parameter	System	Value	Comments
Mass	Support Structures/ Mask and Shields	1.13 kg	Optical bench (0.35 kg), side shield (0.32 kg), mask and mount frame (0.45 kg)
	Detector & electronics	0.62 kg	4xCCD and mount frame (0.07 kg), radiation cover and slide mechanism (0.20 kg), electronics boards (0.35 kg)
	Avionics & OSIRIS Interface	0.90 kg	PMAD, C&DH boards, interface structure, etc
	Mass Total	**2.65 kg**	
Power	Detectors & Electronics	5W	CCD Detector and analog electronics (1.5W). Digital electronics (3.5W).
	Thermal Control	2W	Allocated, but not anticipated necessary.
	Power Total	**7 W**	
Data	Readout rate	24 s	Temporal resolution of the stored event data
	Total Photons	50M	Under 100 MB with 4 bit energy + 12 bit pixel interleaved with 18 bit time tags for 24 sec res.

Table B-1: A short summary of the physical parameters, power and data requirements for the REXIS instrument. REXIS will provide high science return and outstanding student opportunities with low demand on resources of mass, power, and telemetry.
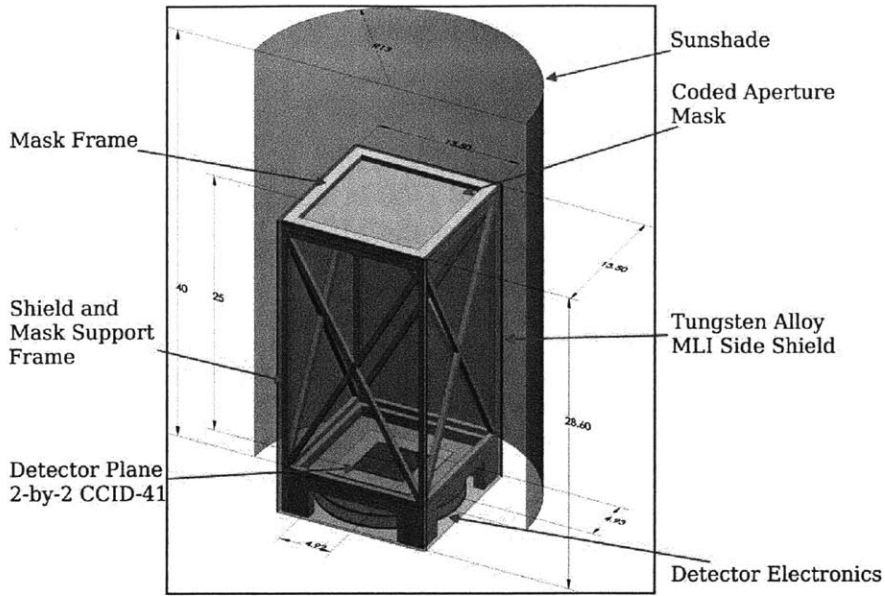
Figure B-1: REXIS 3D model, with dimensions 13.5 x 13.5 x 28.6 cm. Detector electronics and interface to the main spacecraft are housed beneath the optical bench immediately beneath the detector plane. The detector plane is composed of a 2 x 2 array of CCID-41 CCDs for a total detector size of 4.98 cm x 4.98 cm. The mask is suspended above the optical bench on a lightweight / durable frame (Al or carbon fiber). The mask is composed of a single 0.030 mm thick Au layer suspended in a square frame which is affixed directly to the frame. A tungsten alloy shield and Mylar layer extends around the mask tower. A solar shield consisting of an aluminized Mylar sheet on a lightweight frame, in conjunction with a radiator affixed to the spacecraft cold face (not pictured) maintain a maximum CCD operating temperature of -60 deg. C.
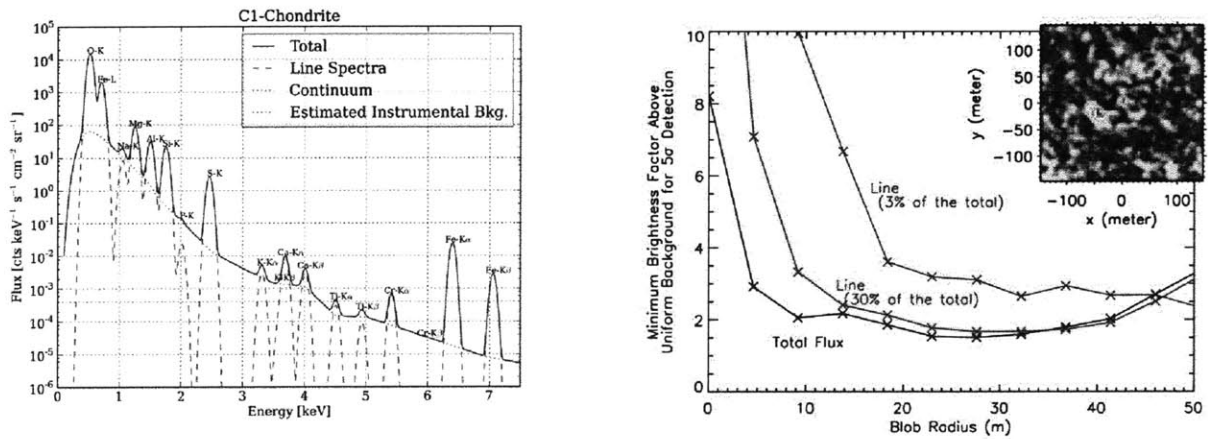
Figure B-2: **(Top)** The simulated X-ray fluorescence spectrum from regolith of a C1 carbonaceous chondrite for the quiescent Sun for the *REXIS* instrument with the asteroid at a heliocentric distance of 1 AU. Increased solar activity can increase fluxes by 2 to 4 orders of magnitude over those shown. The instrumental background estimate shown above has been adopted from (Fraser, et.al 2010) **(Bottom)** Minimal detectable (5σ) excess of a high concentration surface unit vs. unit radius (m) for the total flux (black) and a lines constituting 3% (blue) and 30% (red) of the total flux (c.f. 1-40% of the total for the 5 brightest observable fluorescence lines (see Table 2)). The inset shows a simulated image from 700m of a region containing three units with factors of 5, 6, and 10 higher concentration of O than the surrounding region reconstructed with the preliminary random mask design.

121

IIb. REXIS Simulations and Expected Results

X-ray fluorescence spectra of the lunar regolith have been measured with the *Chandra* X-ray Observatory at high spatial resolution but ~300eV spectral resolution, with CCDs similar to those proposed for REXIS (Wargelin et al. 2004, ApJ, 607, 596). For the prediction of the count rates expected for REXIS during phase 5B (700 m standoff distance from the surface of RQ36) we have utilized simulations carried out for the MIXS (Mercury Imaging X-Ray spectrometer) on Beppicolombo (c.f. Fraser et al. 2010, P&SS, 58, 79F) scaling the result to account for the expected energy resolution of the BI CCID-41 detector plane (~80 eV FWHM) and the distance of *RQ36* from the sun (nominally 1 AU) The predicted X-ray spectrum is shown in Figure 2. (The simulation was verified using a separate lunar composition simulation and agree with Chandra lunar observations to within a factor of ~2). The 4.3 h rotation period of the asteroid was included and allows the full mapping of the surface to be conducted. With the 220 nm Al optical blocking filter CCD, to block the optical solar flux reflected from the asteroid, a total count rate of 7.3 cts/sec in the 1.0–7.5 keV band is predicted and 1037.5 cts/sec in the 0.3–1.0 keV band with the sun in a quiescent state. 2% of the events in the 0.3-1.0 keV band will be kept after the imposition of the 52M event total limit for 21 days of integration using an additional or software imposed filter. In non-imaging spectroscopic analysis, each of the most prominent lines (S-K, O-K, Mg-K, Al-K, etc.) is expected to be detectable within less than an hour of integration time, providing the relative abundance of elements within the whole asteroid (Table 2). Thus, spatially resolved spectra and composition of the surface of the asteroid will be possible. The average spectrum and composition over the illuminated asteroid surface will be obtainable through time resolved spectral information. On smaller scales (4.3 m single pixel) overabundances above a factor of 2 above the mean composition will be resolvable at 5σ from the full integration according to a set of preliminary simulations using a random mask pattern (Figure 2). Further optimization of the mask pattern (trade-off between coding noise from random mask and ghost images from URA), pixel size (trade-off between the total events and the coding-noise in case of the random mask) and the software event filter (for optimal line detection) may improve imaging sensitivity and are currently under study.

Element (Line)	Event Rate (s⁻¹)	Fraction of total data collected.	Minimum Integration Time for 5σ Detection (sec.)
O-K	13.8 (690.1)	0.49	1.84 (0.04)
Mg-K	2.19	0.08	13.7
S-K	0.07	0.002	370
Fe-L	1.26 (63.8)	0.05	21.2 (0.42)
Si-K	0.7	0.02	37.9

Table B-2: The expected minimum exposure time required for the 5 sigma detection of the fluorescence lines of selected elements during Phase 5B (700 km terminator orbit). The individual line strengths were rescaled from a simulation for the lunar regolith to properly account for the abundances expected in a C1 carbonaceous chondrite (c.f. Anders and Grevesse 1989; *Geochim Cosmochim Acta* 53, 197). The fraction of total collected events is shown after the implementation of a software filter which randomly culls 98% of the events below 1 keV in order to stay within data storage requirements. The minimum integration times and event rates shown in parentheses reflect the expected values in the absence of the software filter.

III. REXIS Risk Reduction Approach

To ensure success, REXIS inherits components extensively from HETE-2 SXC (Soft X-Ray Camera) and the Suzaku-XIS (X-Ray Imaging Spectrometer). Suzaku-XIS has been in continuous operation since its 2005 launch, HETE-2 (launched in 2000) remained operational for 6 years. REXIS will utilize 4 back-illuminated MIT Lincoln Laboratory (LL) CCID-41 CCDs, identical to those used in the Suzaku-XIS. Implementation in REXIS requires only minor modification of existing backend electronics. The physical structure of the 0.030 mm thick Au mask as well as the associated side shielding is inherited directly from HETE-2.

A full design study and evaluation will be carried out to ensure seamless operation of REXIS with the OSIRIS-REx spacecraft as well as instrument survivability in flight and launch. During this phase, a dedicated CCD lot will be fabricated to supply and test eight front-illuminated (FI) and eight back-illuminated (BI) CCID-41s. Given historic production yields, a single fabrication lot will provide ample CCD supplies for OSIRIS-REx, but in accordance with standard MIT Lincoln Laboratory practice for flight programs, the primary production lot will be 'shadowed' by a backup lot (delayed relative to the primary lot by about 1 month) to ensure adequate yield. This strategy has provided adequate supplies of high-quality CCDs, within schedule and budget, for all six flight CCD instruments MKI and MIT Lincoln Laboratory have jointly developed. The FI-CCDs will be used for integration into the design and engineering models of the REXIS instrument for initial testing of the instrument and design. After completion of end-to-end testing, the BI-CCD's will be integrated into two REXIS flight models and delivered to the OSIRIS-REx project. Finally a flight model and a flight spare will be constructed and undergo an end-to-end laboratory test before integration testing with the OSIRIS-REX spacecraft. CCDs are susceptible to damage from solar wind protons. To counter this, a one-time retractable Al CCD cover located immediately above the detector plane will be integrated to shield the CCD from these particles and ensure the viability of the detector plane throughout the asteroid operations. This critical part will undergo substantial risk analysis.

IV. REXIS Management and Student Oversight Plan

Four organizational elements bring strength to the REXIS payload: MIT Space Systems Laboratory (SSL), MIT Department of Earth Atmospheric and Planetary Sciences (EAPS), MIT Kavli Institute for Astrophysics and Space Research, and the Harvard College Observatory (HCO) - a member of the Harvard-Smithsonian Center for Astrophysics. All organizations (except Kavli Institute) will contribute students. EAPS and Kavli will provide scientific and technical consultation. HCO and SSL will design and test, with individual responsibilities delineated by system architecture; HCO will develop the spectrometer's digital electronics, while the SSL will produce the analog electronics and overall structure.

The MIT SSL will serve as the primary organizer of student participation through its multi-semester Conceive, Design, Implement and Operate (CDIO) curriculum. This curriculum is cross-listed between the Department of Aeronautics and Astronautics and EAPS at MIT and open to Harvard students for credit. CDIO immerses undergraduate and graduate students in the professional process of developing aerospace systems through requirements flow down, design, fabrication, test, and operations while documenting and communicating their progress to faculty and external reviewers. CDIO has created several highly successful payloads that have flown on the Space Transportation System and the International Space Station.

Several mechanisms are designed into the CDIO class structure to ensure system quality while maximizing student participation. As identified in Section 1.2.9, senior mentors with flight

program experience are assigned to each subsystem team. These mentors provide continuity throughout the program and will oversee the development of three payload models that serve to reduce risk while providing hands-on training to students in the **CDIO** curriculum throughout the timeline of the project: Design Model, Engineering Model, Flight model. The Design Model, will validate the functional capability of the design. The Engineering Model will refine fabrication, integration, and environmental test procedures. Finally, the Flight Model will be the deliverable. Two Flight Models will be delivered to provide a backup in the event of problems during carrier integration, as a ground unit for diagnosing issues during the mission, and as an opportunity to qualify the flight hardware to higher levels. The **CDIO** class has access to a professional clean room, electronics laboratory, and machine shop through the MIT SSL as well as environmental test facilities at MIT Lincoln Laboratory (vibration, thermal-vacuum, anechoic).

V. REXIS Additional Training Opportunities and Student Involvement

CDIO is open to all academic majors at Harvard and MIT and is routinely taken by thirty to sixty undergraduate students each semester. The workforce for the class is complemented year-round by students participating in the Undergraduate Research Opportunities Program (UROP) as well as the MIT Satellite Club. MIT and Harvard graduate students in the organizational structure (Section 1.2.9) will help mentor the additional **CDIO** students. REXIS will become integral to their graduate research. Broader outreach is anticipated through the Boston Museum of Science as well as through enrichment programs for K-12 students sponsored by the MIT Edgerton Center.

VI. REXIS Budget and Schedule

The *REXIS* Work Breakdown Structure (WBS) budget and schedule is presented in accompanying documentation. The high heritage for the major detector and electronic components enables strong reliability relative to cost risk.

VII. REXIS Key Personnel

REXIS senior and student key personnel are identified in Figure 3. Senior Scientist oversight and the proven **CDIO** academic structure provide the continuity for the progression of students through the multi-year project. We identify current students to fill leadership roles, representative of the quality of students who will perform throughout the mission timeline.
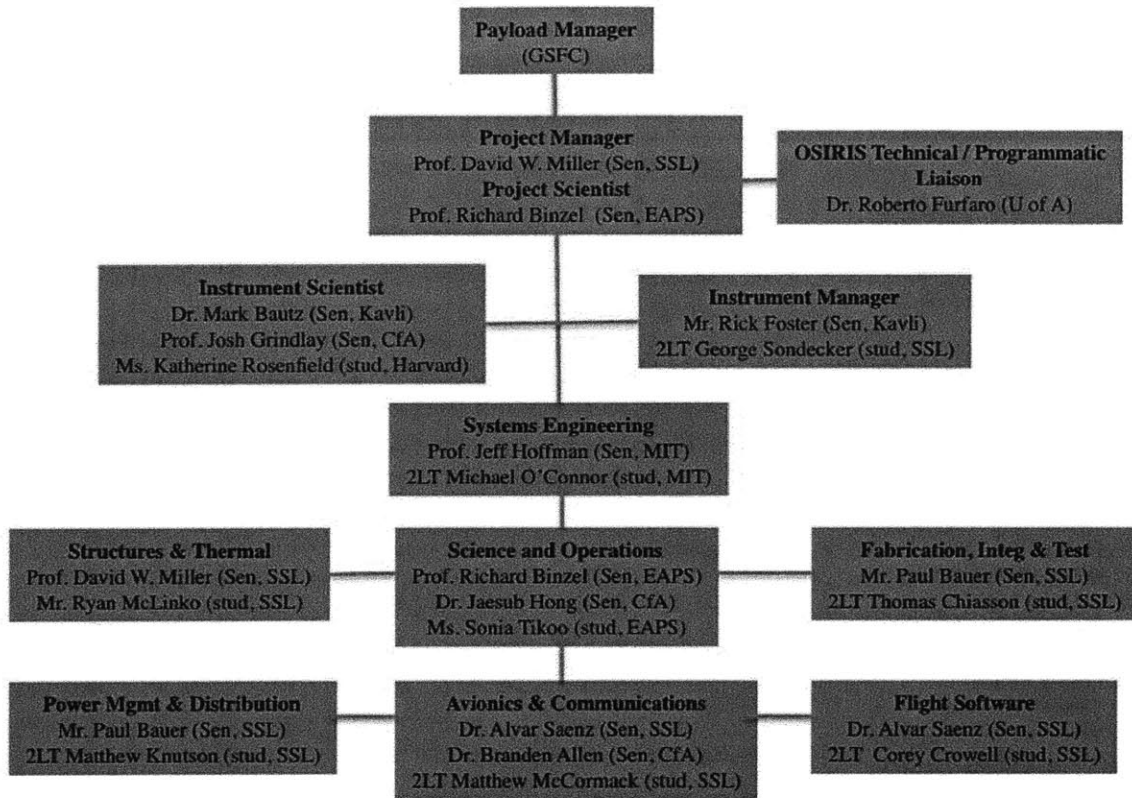
Figure B-3: REXIS Organization fully integrates the students working with and learning from their Senior Scientist advisors.

VIII. REXIS Summary

REXIS brings a new dimension in the global characterization of the asteroid target for understanding the representational context of the returned sample. REXIS brings the strengths of four groups within MIT and Harvard utilizing the flight proven Conceive, Design, Implement and Operate curriculum, with the potential to involve more than 100 students throughout the process. REXIS is based on flight heritage hardware, thereby minimizing all elements of technical risk, schedule risk, and cost risk.

Appendix C - REXIS Budget

Expense	Total Cost ($k)				
	GFY-11	GFY-12	GFY-13	GFY-14	GFY-15
Hardware					
Detector Plane Array					
CCD Test Detector	20				
CCID-41 Detectors		340			
Detector Processing			60		
Detector Packaging			160		
Solar Monitor					
Si PIN Detector		5	5	10	
Aluminum Blocking Filter		2	2	4	
Housing Fabrication		1	3	6	
Board Fabrication		5	10	20	
Mask					
Gold Mask Fabrication			15	30	
Avionics Board					
ASIC Fabrication			200	200	
Board Fabrication		5	10	20	
Power Board					
Board Fabrication		5	10	20	
Box Fabrication		1	4	8	
Tower and Mask Frame					
Tower Fabrication		0.5	4	8	
Mask Frame Fabrication		0.5	2	4	
Radiation Shield and Mechanism					
Shield Fabrication		0.1	0.5	1	
Shield Release Mechanism		1	10	20	
Thermal Shield and Radiator					
Shield Fabrication		0.5	1	2	
Thermal Coating		1	1	1	
Radiator Fabrication		1	5	10	
Thermal Strap		1	5	10	
Miscellaneous					
NAS Fasteners		1	1	2	
Wiring Harness and Connectors		1	5	10	
Conformal Coating		0.5	0.5	1	
Alondine Coating		0.5	0.5	1	
Test					
CCD Testing			50		
Vibration			4	4	8
Thermal Vacuum			4	4	8
Radiation			10	20	
Salary					
Faculty (x3)		93	93	93	93
Technical Staff (x4)	83	305	305	305	305
Post-Doctoral Researcher (x2)	27	102	102	102	102
Research Assistant (SM Candidate) (x4)	210	210	210	210	210
Miscellaneous Expenses					
Computing					
CAD Software	10	10	10	10	10
Finite Element Analysis Software	3	3	3	3	3
Thermal Analysis Software	5	5	5	5	5
Electronics Board Design Software	2	2	2	2	2
Travel	20	20	20	20	20
ANNUAL TOTALS:	380	1122.6	1332.5	1166	766
PROJECT TOTAL:	$4767.1k				

Appendix D - REXIS Schedule

Task Name	Dur"	Start	Finish
REXIS (REgolith X-ray Imaging Spectrometer)	1869	8/1/2011	9/12/2016
REXIS Key Milestones	1430	8/1/2011	7/1/2015
Phase B Bridge ATP (for Instrument Teams)	0	8/1/2011	8/1/2011
REXIS SRR (System Requirements Review)	0	12/9/2011	12/9/2011
Phase B ATP (Authorization to Proceed)	0	12/15/2011	12/15/2011
REXIS SDR (Systems Definition Review)	0	5/4/2012	5/4/2012
REXIS PDR (Preliminary Design Review)	0	12/7/2012	12/7/2012
REXIS CDR (Critical Design Review)	0	12/6/2013	12/6/2013
I&T Start (Integration and Test)	0	6/2/2014	6/2/2014
PER (Pre-Environmental Review)	0	12/5/2014	12/5/2014
PSR (Pre-Ship Review)	0	5/4/2015	5/4/2015
Delivery to ATLO (Assembly, Test & Launch Operations)	0	7/1/2015	7/1/2015
Phase B Bridge	135	8/1/2011	12/14/2011
Long Lead Procurements	480	9/19/2011	1/11/2013
CCID-41 Detector (Lincoln Lab) (8 Front-Illuminated, 8 Back-Illuminated)	480	9/19/2011	1/11/2013
Prepare Spec for Detector	11	9/19/2011	9/30/2011
Award Detector Procurement	4	11/28/2011	12/2/2011
Fabricate Detector	347	1/2/2012	12/14/2012
Deliver Detector	9	1/2/2013	1/11/2013
SCE Kickoff and Initial S/C Review	0	9/8/2011	9/8/2011
Initial Requirements Development	19	9/11/2011	9/30/2011
Contamination Risk Reduction	11	9/19/2011	9/30/2011
Inteface Document Definition	18	9/19/2011	10/7/2011
Establish Fileshare with Revision Control	4	8/22/2011	8/26/2011
Initial GSE Definition	18	10/31/2011	11/18/2011
Prepare SRR Package for REXIS	15	11/7/2011	11/22/2011
REXIS SRR	0	12/9/2011	12/9/2011
Instrument Systems Engineering	403	1/9/2012	2/15/2013
Requirements Development	627	1/9/2012	9/27/2013
Update Level 3 Requirements (Post SRR)	46	1/9/2012	2/24/2012
Deliver Updated REXIS Level 3 Requirements Document for I-SDR	0	2/24/2012	2/24/2012
Update Level 3 Requirements to Reflect Preliminary Design	18	9/10/2012	9/28/2012
Deliver Updated REXIS Level 3 Requirements Document for I-PDR	0	9/28/2012	9/28/2012
Update Level 3 Requirements to Reflect Critical Design	18	9/9/2013	9/27/2013
Deliver Updated REXIS Level 3 Requirements Document for I-CDR	0	9/27/2013	9/27/2013
Interface Definition	774	1/9/2012	2/21/2014
Update REXIS/Bus Interface (Post SRR)	46	1/9/2012	2/24/2012
Deliver REXIS Interface for I-SDR	0	2/24/2012	2/24/2012
Update REXIS/Bus to Reflect Preliminary Design	18	9/10/2012	9/28/2012
Deliver REXIS/Bus Interface for I-PDR	0	9/28/2012	9/28/2012
Post PDR Update of REXIS/Bus Interface to Reflect Critical Design	18	9/9/2013	9/27/2013
Deliver REXIS/BusInteface for I-CDR	0	9/27/2013	9/27/2013
Post I-CDR Update REXIS/Bus Interface to Reflect CDR Comments	46	1/6/2014	2/21/2014
Simulators	522	9/12/2011	2/15/2013
Develop REXIS H/W Instrument Simulator (ETU-1) for STL	508	9/12/2011	2/1/2013
Deliver H/W Simulator (ETU-1) to STL	0	2/15/2013	2/15/2013
Develop REXIS S/W Instrument Simulator for STL	347	2/20/2012	2/1/2013
Deliver REXIS S/W Instrument Simulator for STL	0	2/15/2013	2/15/2013
Prepare REXIS SDR Package	11	4/16/2012	4/27/2012
REXIS SDR	0	5/4/2012	5/4/2012

Task Name	Dur*	Start	Finish
REXIS Analysis/Modeling	1278	9/12/2011	3/13/2015
Instrument Structural Model Development	903	9/12/2011	3/3/2014
Develop ETU-1 CAD Model	88	9/12/2011	12/9/2011
ETU-1 CAD Freeze	0	4/8/2012	4/8/2012
ETU-2 Updates to ETU-1 CAD Model	39	2/4/2013	3/15/2013
ETU-2 CAD Freeze	0	5/17/2013	5/17/2013
Flight Updates to ETU-2 CAD Model	28	2/3/2014	3/3/2014
Flight Model CAD Freeze	0	3/3/2014	3/3/2014
Instrument Finite Element Model Development	1103	2/6/2012	2/13/2015
Develop ETU-1 Finite Element Model	39	2/6/2012	3/16/2012
Deliver Finite Element Model for PDR	0	8/24/2012	8/24/2012
Correlate ETU-1 Coupled Loads Model with Vibe Test Data	11	2/4/2013	2/15/2013
ETU-2 Updates to ETU-1 Finite Element Model	46	3/18/2013	5/3/2013
Correlate ETU-2 Finite Element Model with Vibe Test Data	11	2/3/2014	2/14/2014
Deliver Finite Element Model for CDR	0	5/3/2013	5/3/2013
Flight Updates to ETU-2 Finite Element Model	25	3/3/2014	3/28/2014
Correlate Flight Finite Element Model with Vibe Test Data	11	2/2/2015	2/13/2015
Instrument Thermal Model Development	1131	2/6/2012	3/13/2015
Develop ETU-1 Thermal Model	39	2/6/2012	3/16/2012
Correlate ETU-1 Thermal Model with Thermal Test Data	11	2/4/2013	2/15/2013
ETU-2 Updates to ETU-1 Thermal Model	46	3/18/2013	5/3/2013
Correlate ETU-2 Thermal Model with Thermal Test Data	11	2/3/2014	2/14/2014
Flight Updates to ETU-2 Thermal Model	25	3/3/2014	3/28/2014
Correlate Flight Thermal Model with Thermal Test Data	11	3/2/2015	3/13/2015
Instrument Development	1096	9/12/2011	9/12/2014
Prepare I-PDR Package for REXIS	11	11/12/2012	11/23/2012
REXIS PDR	0	12/7/2012	12/7/2012
Prepare I-CDR Package for REXIS	11	11/11/2013	11/22/2013
REXIS I-CDR Package	0	12/6/2013	12/6/2013
REXIS Electronics Box (E-Box)	1033	9/12/2011	7/11/2014
ETU-1	333	9/12/2011	8/10/2012
Design ETU-1 Enclosure	11	9/12/2011	9/23/2011
Resolve Detector Thermal and Mechanical Interface	18	9/26/2011	10/14/2011
E-Box Thermal Analysis	4	2/6/2012	2/10/2012
E-Box Structural Analysis	4	2/6/2012	2/10/2012
Develop E-Box Fabrication Drawings	2	4/11/2012	4/13/2012
Fabricate ETU-1 Enclosure	39	6/11/2012	7/20/2012
Inspect and QA ETU-1 Enclosure	0	7/23/2012	7/23/2012
Assemble ETU-1 E-Box	11	7/23/2012	8/3/2012
Deliver ETU-1 E-Box	0	8/10/2012	8/10/2012
ETU-2	186	2/4/2013	8/9/2013
Update ETU-1 Enclosure Design	8	2/4/2013	2/12/2013
Update Detector Thermal and Mechanical Interface	9	2/13/2013	2/22/2013
Develop E-Box Fabrication Drawings	4	4/29/2013	5/3/2013
E-Box Thermal Analysis	11	3/18/2013	3/29/2013
E-Box Structural Analysis	11	3/18/2013	3/29/2013
Fabricate ETU-2 Enclosure	39	6/10/2013	7/19/2013
Fabricate E-Box Harnessing	18	6/10/2013	6/28/2013
Inspect and QA ETU-2 Enclosure	0	7/22/2013	7/22/2013
Assemble ETU-2 E-Box	11	7/29/2013	8/9/2013
Deliver ETU-2 E-Box	0	8/9/2013	8/9/2013

Task Name	Dur*	Start	Finish
Flight	162	2/13/2014	7/25/2014
Update ETU-2 Enclosure Design	11	2/3/2014	2/14/2014
Update Detector Thermal and Mechanical Interface	4	2/13/2014	2/17/2014
Develop E-Box Fabrication Drawings	4	3/31/2014	4/4/2014
E-Box Thermal Analysis	4	3/3/2014	3/7/2014
E-Box Structural Analysis	4	3/3/2014	3/7/2014
Procure Flight Enclosures	4	4/21/2014	4/25/2014
Fabricate Flight Enclosures	32	4/28/2014	5/30/2014
Fabricate E-Box Harnessing	32	4/28/2014	5/30/2014
Apply Alodine Coating	11	6/2/2014	6/13/2014
Inspect and QA Flight Enclosures	0	6/16/2014	6/16/2014
Assemble Flight E-Boxes	18	6/23/2014	7/11/2014
Deliver Flight E-Boxes	0	7/11/2014	7/11/2014
REXIS Tower and Mask Frame	1033	9/26/2011	7/25/2014
ETU-1	319	9/26/2011	8/10/2012
Design ETU-1 Tower and Mask Frame	11	9/26/2011	10/7/2011
Develop Tower and Mask Frame Fabrication Drawings	1	4/14/2012	4/15/2012
Tower and Mask Frame Thermal Analysis	4	2/13/2012	2/17/2012
Tower and Mask Frame Structural Analysis	4	2/13/2012	2/17/2012
Fabricate ETU-1 Tower and Mask Frame	39	6/11/2012	7/20/2012
Inspect and QA ETU-1 Tower and Mask Frame	0	7/23/2012	7/23/2012
Assemble ETU-1 Tower and Mask Frame	7	8/3/2012	8/10/2012
Deliver ETU-1 Tower and Mask Frame	0	8/10/2012	8/10/2012
ETU-2	184	2/13/2013	8/16/2013
Update ETU-1 Enclosure Design	2	2/13/2013	2/15/2013
Develop E-Box Fabrication Drawings	2	5/6/2013	5/8/2013
E-Box Thermal Analysis	11	3/18/2013	3/29/2013
E-Box Structural Analysis	11	3/18/2013	3/29/2013
Fabricate ETU-2 Enclosure	39	6/10/2013	7/19/2013
Inspect and QA ETU-2 Enclosure	0	7/23/2013	7/23/2013
Assemble ETU-2 E-Box	4	8/12/2013	8/16/2013
Deliver ETU-2 E-Box	0	8/16/2013	8/16/2013
Flight	158	2/17/2014	7/25/2014
Update ETU-2 Enclosure Design	2	2/17/2014	2/19/2014
Develop E-Box Fabrication Drawings	2	4/7/2014	4/9/2014
E-Box Thermal Analysis	2	3/10/2014	3/12/2014
E-Box Structural Analysis	2	3/10/2014	3/12/2014
Procure Flight Enclosures	4	4/21/2014	4/25/2014
Fabricate Flight Enclosures	32	4/28/2014	5/30/2014
Apply Alodine Coating	11	6/2/2014	6/13/2014
Inspect and QA Flight Enclosures	0	6/17/2014	6/17/2014
Assemble Flight E-Boxes	11	7/14/2014	7/25/2014
Deliver Flight E-Boxes	0	7/25/2014	7/25/2014

Task Name	Dur"	Start	Finish
REXIS Avionics Board	1040	9/12/2011	7/18/2014
Design Avionics Board	60	9/12/2011	11/11/2011
Draw Board Schematic	4	11/14/2011	11/18/2011
Develop ETU-1 Bread Board	11	2/6/2012	2/17/2012
Establish ETU-1 Basic Software Functionality	25	2/20/2012	3/16/2012
ETU-2	480	4/2/2012	7/26/2013
Update ETU-1 Avionics Board Design	25	4/2/2012	4/27/2012
Draw Avionics Board Schematic	4	4/30/2012	5/4/2012
Develop ETU-2 Bread Board	11	5/7/2012	5/18/2012
Establish Mature Software Functionality	109	6/11/2012	9/28/2012
Design ETU-2 ASIC	25	10/1/2012	10/26/2012
Procure ETU-2 ASIC	11	11/5/2012	11/16/2012
Fabricate ETU-2 ASIC	130	1/7/2013	5/17/2013
Fabricate ETU-2 Avionics Board	45	5/29/2013	7/13/2013
Conformal Coat ETU-2 Avionics Board	11	7/15/2013	7/26/2013
Deliver ETU-2 Avionics Board	0	7/26/2013	7/26/2013
Flight	305	9/16/2013	7/18/2014
Update ETU-2 Avionics Board Design	39	9/16/2013	10/25/2013
Draw Board Schematic	4	10/28/2013	11/1/2013
Update ETU-2 ASIC Design	18	11/4/2013	11/22/2013
Complete Software Development	109	1/13/2014	5/2/2014
Procure Flight ASIC	4	1/13/2014	1/17/2014
Fabricate Flight ASIC	123	1/20/2014	5/23/2014
Fabricate Flight Avionics Board	18	6/2/2014	6/20/2014
Conformal Coat Flight Avionics Board	25	6/23/2014	7/18/2014
Deliver Flight Avioncs Board	0	7/18/2014	7/18/2014
REXIS Power Board	1040	9/12/2011	7/18/2014
ETU-1	158	9/12/2011	2/17/2012
Design Power Board	60	9/12/2011	11/11/2011
Draw Power Board Schematic	4	11/14/2011	11/18/2011
Develop ETU-1 Bread Board	11	2/6/2012	2/17/2012
ETU-2	312	9/17/2012	7/26/2013
Update ETU-1 Power Board Design	39	9/17/2012	10/26/2012
Draw Power Board Schematic	4	10/29/2012	11/2/2012
Develop ETU-2 Bread Board	11	11/5/2012	11/16/2012
Procure ETU-2 Power Board	11	5/6/2013	5/17/2013
Fabricate ETU-2 Power Board	45	5/29/2013	7/13/2013
Conformal Coat ETU-2 Power Board	11	7/15/2013	7/26/2013
Deliver ETU-2 Power Board	0	7/26/2013	7/26/2013
Flight	305	9/16/2013	7/18/2014
Update ETU-2 Power Board Design	39	9/16/2013	10/25/2013
Draw Power Board Schematic	4	10/28/2013	11/1/2013
Develop Flight Bread Board	11	11/4/2013	11/15/2013
Procure Flight Power Board	4	1/19/2014	1/23/2014
Fabricate Flight Power Board	18	2/2/2014	2/20/2014
Conformal Coat Flight Power Board	25	6/23/2014	7/18/2014
Deliver Flight Power Board	0	7/18/2014	7/18/2014

130

Task Name	Dur*	Start	Finish
REXIS Mask	942	10/3/2011	5/2/2014
Run Mask Simulations	25	10/3/2011	10/28/2011
Select Mask Design	4	10/31/2011	11/4/2011
Identify Mask Vendor	11	11/7/2011	11/18/2011
ETU-2	88	2/4/2013	5/3/2013
Procure Mask	11	2/4/2013	2/15/2013
Fabricate Mask	67	2/18/2013	4/26/2013
Inspect and QA Mask	4	4/29/2013	5/3/2013
Deliver ETU-2 Mask	0	5/3/2013	5/3/2013
Flight	88	2/3/2014	5/2/2014
Update Mask Design	11	2/3/2014	2/14/2014
Procure Mask	4	2/17/2014	2/21/2014
Fabricate Mask	67	2/24/2014	5/2/2014
Inspect and QA Mask	0	5/2/2014	5/2/2014
Deliver Flight Mask	0	5/2/2014	5/2/2014
REXIS Detector Plane Array	1026	10/10/2011	8/1/2014
ETU-1	291	10/10/2011	7/27/2012
Design ETU-1 Detector Plane	11	10/10/2011	10/21/2011
Develop Fabrication Drawings and Electrical Schematics	1	4/16/2012	4/17/2012
Detector Plane Thermal Analysis	4	2/20/2012	2/24/2012
Detector Plane Structural Analysis	4	2/20/2012	2/24/2012
Fabricate Detector Plane	18	6/11/2012	6/29/2012
Inspect and QA Detecor Plane	0	7/2/2012	7/2/2012
Assemble Solar Detector Plane	18	7/9/2012	7/27/2012
Deliver ETU-1 Detector Plane	0	7/27/2012	7/27/2012
ETU-2	184	2/18/2013	8/21/2013
Update ETU-1 Detector Plane Design	2	2/18/2013	2/20/2013
Develop Fabrication Drawings and Electrical Schematics	0	5/9/2013	5/9/2013
Update Detector Plane Thermal Analysis	4	4/1/2013	4/5/2013
Update Detector Plane Structural Analysis	4	4/1/2013	4/5/2013
Fabricate Detector Plane	39	6/10/2013	7/19/2013
Inspect and QA Detecor Plane	0	7/24/2013	7/24/2013
Assemble Solar Detector Plane	2	8/19/2013	8/21/2013
Deliver ETU-2 Detector Plane Array	0	8/21/2013	8/21/2013
Flight	162	2/20/2014	8/1/2014
Update ETU-2 Detector Plane Design	1	2/20/2014	2/21/2014
Develop Fabrication Drawings and Electrical Schematics	0	4/14/2014	4/14/2014
Update Detector Plane Thermal Analysis	1	3/13/2014	3/14/2014
Update Detector Plane Structural Analysis	1	3/13/2014	3/14/2014
Fabricate Detector Planes	32	4/28/2014	5/30/2014
Inspect and QA Detecor Planes	0	6/4/2014	6/4/2014
Assemble Solar Detector Planes	4	7/28/2014	8/1/2014
Deliver Flight Detector Plane Arrays	0	8/1/2014	8/1/2014
REXIS Radiation Shield and Mechanism	1019	10/24/2011	8/8/2014
ETU-1	270	10/24/2011	7/20/2012
Design Radiation Shield and Mechanism	4	10/24/2011	10/28/2011
Develop Radiation Shield and Mechanism Fabrication Drawings	0	4/18/2012	4/18/2012
Radiation Shield and Mechanism Structural Analysis	2	2/27/2012	2/29/2012
Radiation Shield and Mechanism Thermal Analysis	2	2/27/2012	2/29/2012
Procure Radiation Shield Mechanism	28	6/11/2012	7/9/2012
Fabricate Radiation Shield	4	7/9/2012	7/13/2012
Inspect and QA Radiation Shield and Mechanism	0	7/16/2012	7/16/2012
Assemble Radiation Shield and Mechanism	3	7/17/2012	7/20/2012
Deliver ETU-1 Radiation Shield and Mechanism	0	7/20/2012	7/20/2012

Task Name	Dur*	Start	Finish
ETU-2	372	4/8/2013	4/15/2014
Develop Radiation Shield and Mechanism Fabrication Drawings	4	5/10/2010	5/14/2010
Update Radiation Shield and Mechanism Structural Analysis	2	4/8/2013	4/10/2013
Procure Radiation Shield Mechanism	32	4/8/2013	5/10/2013
Fabricate Radiation Shield	39	6/10/2013	7/19/2013
Inspect and QA Radiation Shield and Mechanism	0	7/24/2013	7/24/2013
Assemble Radiation Shield and Mechanism	1	8/22/2013	8/23/2013
Deliver ETU-2 Radiation Shield and Mechanism	0	8/23/2013	8/23/2013
Flight	165	2/24/2014	8/8/2014
Update ETU-2 Radiation Shield and Mechanism Design	1	2/24/2014	2/25/2014
Develop Radiation Shield and Mechanism Fabrication Drawings	0	4/15/2014	4/15/2014
Update Radiation Shield and Mechanism Structural Analysis	0	3/17/2014	3/17/2014
Procure Radiation Shield Mechanism	32	4/28/2014	5/30/2014
Fabricate Radiation Shield	32	4/28/2014	5/30/2014
Apply Alodine Coating	11	6/2/2014	6/13/2014
Inspect and QA Radiation Shield and Mechanism	0	6/18/2014	6/18/2014
Assemble Radiation Shield and Mechanism	4	8/4/2014	8/8/2014
Deliver ETU-2 Radiation Shield and Mechanism	0	8/8/2014	8/8/2014
REXIS Solar Monitor	1026	10/31/2011	8/22/2014
ETU-1	277	10/31/2011	8/3/2012
Design ETU-1 Solar Monitor Housing	4	10/31/2011	11/4/2011
Develop Solar Monitor Box Fabrication Drawings	0	4/19/2012	4/19/2012
Solar Monitor Thermal Analysis	8	3/1/2012	3/9/2012
Solar Monitor Structural Analysis	8	3/1/2012	3/9/2012
Procure Si-PIN Detector	25	6/11/2012	7/6/2012
Fabricate Solar Monitor Housing	4	7/16/2012	7/20/2012
Inspect and QA Solar Monitor Housing	0	7/23/2012	7/23/2012
Assemble Solar Monitor	10	7/24/2012	8/3/2012
Deliver ETU-1 Solar Monitor	0	8/3/2012	8/3/2012
ETU-2	181	2/28/2013	8/28/2013
Update ETU-1 Solar Monitor Housing Design	8	2/28/2013	3/8/2013
Update Si-PIN Detector Thermal and Mechanical Interface	4	3/11/2013	3/15/2013
Develop Solar Monitor Box Fabrication Drawings	2	5/15/2013	5/17/2013
Update Solar Monitor Thermal Analysis	8	4/11/2013	4/19/2013
Update Solar Monitor Structural Analysis	8	4/11/2013	4/19/2013
Procure Si-PIN Detector	60	5/20/2013	7/19/2013
Fabricate Solar Monitor Housing	39	6/10/2013	7/19/2013
Inspect and QA Solar Monitor Housing	0	7/25/2013	7/25/2013
Assemble Solar Monitor	2	8/26/2013	8/28/2013
Deliver ETU-2 Solar Monitor	0	8/28/2013	8/28/2013
Flight	178	2/25/2014	8/22/2014
Update ETU-2 Solar Monitor Housing Design	2	2/25/2014	2/27/2014
Update Si-PIN Detector Thermal and Mechanical Interface	7	2/28/2014	3/7/2014
Develop Solar Monitor Box Fabrication Drawings	2	3/18/2014	3/20/2014
Update Solar Monitor Thermal Analysis	1	3/18/2014	3/19/2014
Update Solar Monitor Structural Analysis	1	4/16/2014	4/17/2014
Procure Si-PIN Detectors	53	4/7/2014	5/30/2014
Fabricate Solar Monitor Housing	60	3/31/2014	5/30/2014
Apply Alodine Coating	11	6/2/2014	6/13/2014
Inspect and QA Solar Monitor Housing	0	6/18/2014	6/18/2014
Assemble Solar Monitor	11	8/11/2014	8/22/2014
Deliver Flight Solar Monitors	0	8/22/2014	8/22/2014

Task Name	Dur"	Start	Finish
REXIS Thermal Shield and Radiator	581	4/20/2012	11/22/2013
Design ETU-1 Thermal Shield / Radiator	11	11/7/2011	11/18/2011
Develop Thermal Shield / Radiator Fabrication Drawings	0	4/20/2012	4/20/2012
Thermal Shield / Radiator Thermal Analysis	4	3/12/2012	3/16/2012
Thermal Shield Structural Analysis	4	3/12/2012	3/16/2012
Fabricate Thermal Shield / Radiator	4	7/23/2012	7/27/2012
Inspect and QA Thermal Shield / Radiator	0	7/30/2012	7/30/2012
Assemble Thermal Shield / Radiator	10	7/31/2012	8/10/2012
Deliver ETU-1 Thermal Shield / Radiator	0	8/10/2012	8/10/2012
ETU-2	180	3/10/2013	9/6/2013
Update ETU-1 Thermal Shield / Radiator Design	5	3/10/2013	3/15/2013
Develop Thermal Shield / Radiator Fabrication Drawings	2	5/20/2013	5/22/2013
Update Thermal Shield / Radiator Thermal Analysis	4	4/22/2013	4/26/2013
Update Thermal Shield / Radiator Structural Analysis	4	4/22/2013	4/26/2013
Fabricate Thermal Shield / Radiator	39	6/10/2013	7/19/2013
Inspect and QA Thermal Shield / Radiator	0	7/26/2013	7/26/2013
Assemble Thermal Shield / Radiator	8	8/29/2013	9/6/2013
Deliver ETU-2 Thermal Shield / Radiator	0	9/6/2013	9/6/2013
Flight	196	2/28/2014	9/12/2014
Update ETU-2 Thermal Shield / Radiator Design	3	2/28/2014	3/3/2014
Develop Thermal Shield / Radiator Fabrication Drawings	0	4/18/2014	4/18/2014
Update Thermal Shield / Radiator Thermal Analysis	1	3/20/2014	3/21/2014
Update Thermal Shield / Radiator Structural Analysis	1	3/20/2014	3/21/2014
Fabricate Thermal Shields / Radiators	53	4/7/2014	5/30/2014
Inspect and QA Thermal Shields / Radiators	0	6/19/2014	6/19/2014
Assemble Thermal Shields / Radiators	18	8/25/2014	9/12/2014
Deliver Flight Thermal Shields / Radiators	0	9/12/2014	9/12/2014
REXIS Assembly/Integration, & Test	949	7/23/2012	2/27/2015
REXIS GSE	67	9/16/2013	11/22/2013
Design Shipping Container	18	9/16/2013	10/4/2013
Design Electrical GSE	11	9/16/2013	9/27/2013
Design Vibe Fixture	4	10/7/2013	10/11/2013
Fabricate Shipping Containers	25	10/14/2013	11/8/2013
Fabricate Electrical GSE	11	10/14/2013	10/25/2013
Fabricate Vibe Fixture	11	11/11/2013	11/22/2013
Assembly/Integration	830	7/23/2012	10/31/2014
Assemble ETU-1	67	7/23/2012	9/28/2012
Inspect and QA ETU-1	4	10/1/2012	10/5/2012
Assemble ETU-2	67	7/29/2013	10/4/2013
Inspsect and QA ETU-2	4	10/7/2013	10/11/2013
Kit Flight Parts	11	9/15/2014	9/26/2014
Assemble Flight Models	116	6/23/2014	10/17/2014
Inspect and QA Flight Models	11	10/20/2014	10/31/2014
REXIS PER Preparation	11	11/10/2014	11/21/2014
REXIS PER	0	12/5/2014	12/5/2014
Test	781	1/7/2013	2/27/2015
ETU-1 Vibe Test	25	1/7/2013	2/1/2013
ETU-1 Thermal-Vacuum Test	25	1/7/2013	2/1/2013
ETU-2 Vibe Test	25	1/6/2014	1/31/2014
ETU-2 Thermal-Vacuum Test	25	1/5/2015	1/30/2015
ETU-2 Radiation Test	25	2/2/2015	2/27/2015
Flight Vibe Test	28	1/2/2015	1/30/2015
Flight Thermal-Vacuum Test	25	2/2/2015	2/27/2015
Schdule Margin	110	3/2/2015	6/20/2015
REXIS PSR Preparation	17	4/13/2015	4/30/2015
REXIS PSR	0	5/4/2015	5/4/2015
Pack REXIS	11	6/6/2015	6/17/2015
Pack GSE	11	6/6/2015	6/17/2015
Ship REXIS and GSE	0	6/20/2015	6/20/2015
REXIS Delivered to ATLO	0	7/1/2015	7/1/2015

Appendix E - COCOMO II Inputs

Software Size   Sizing Method Source Lines of Code ▾

	SLOC	% Design Modified	% Code Modified	% Integration Required	Assessment and Assimilation (0% - 8%)	Software Understanding (0% - 50%)	Unfamiliarity (0-1)
New	4000						
Reused	3000	0	0				
Modified							

Software Scale Drivers

Precedentedness	Nominal ▾	Architecture / Risk Resolution	Nominal ▾	Process Maturity	Very Low ▾
Development Flexibility	Very Low ▾	Team Cohesion	Low ▾		

Software Cost Drivers

Product		Personnel		Platform	
Required Software Reliability	High ▾	Analyst Capability	Very Low ▾	Time Constraint	Nominal ▾
Data Base Size	Nominal ▾	Programmer Capability	Very Low ▾	Storage Constraint	Very High ▾
Product Complexity	Nominal ▾	Personnel Continuity	Very Low ▾	Platform Volatility	Low ▾
Developed for Reusability	High ▾	Application Experience	Very Low ▾		
Documentation Match to Lifecycle Needs	Very High ▾	Platform Experience	Very Low ▾	**Project**	
		Language and Toolset Experience	Low ▾	Use of Software Tools	Nominal ▾
				Multisite Development	Nominal ▾
				Required Development Schedule	Nominal ▾

Figure E-1: COCOMO II Inputs for Student and Faculty Software Development [28]

Software Size   Sizing Method Source Lines of Code ▾

	SLOC	% Design Modified	% Code Modified	% Integration Required	Assessment and Assimilation (0% - 8%)	Software Understanding (0% - 50%)	Unfamiliarity (0-1)
New	4000						
Reused	3000	0	0				
Modified							

Software Scale Drivers

Precedentedness	Nominal ▾	Architecture / Risk Resolution	Nominal ▾	Process Maturity	Very Low ▾
Development Flexibility	Very Low ▾	Team Cohesion	Low ▾		

Software Cost Drivers

Product		Personnel		Platform	
Required Software Reliability	High ▾	Analyst Capability	Very Low ▾	Time Constraint	Nominal ▾
Data Base Size	Nominal ▾	Programmer Capability	Very Low ▾	Storage Constraint	Very High ▾
Product Complexity	Nominal ▾	Personnel Continuity	Very Low ▾	Platform Volatility	Low ▾
Developed for Reusability	High ▾	Application Experience	Very Low ▾		
Documentation Match to Lifecycle Needs	Very High ▾	Platform Experience	Very Low ▾	**Project**	
		Language and Toolset Experience	Low ▾	Use of Software Tools	Nominal ▾
				Multisite Development	Nominal ▾
				Required Development Schedule	Nominal ▾

Figure E-2: COCOMO II Inputs for the Addition of a Professional Software Engineer to the REXIS Software Team [28]

134

Software Size   Sizing Method Source Lines of Code ▼

	SLOC	% Design Modified	% Code Modified	% Integration Required	Assessment and Assimilation (0% - 8%)	Software Understanding (0% - 50%)	Unfamiliarity (0-1)
New	4000						
Reused	3000	0	0				
Modified							

Software Scale Drivers

Precedentedness	Nominal ▼	Architecture / Risk Resolution	Nominal ▼	Process Maturity	Nominal ▼
Development Flexibility	Very Low ▼	Team Cohesion	Low ▼		

Software Cost Drivers

| Product		Personnel		Platform	
Required Software Reliability	High ▼	Analyst Capability	Nominal ▼	Time Constraint	Nominal ▼
Data Base Size	Nominal ▼	Programmer Capability	Nominal ▼	Storage Constraint	Very High ▼
Product Complexity	Nominal ▼	Personnel Continuity	Nominal ▼	Platform Volatility	Low ▼
Developed for Reusability	High ▼	Application Experience	Nominal ▼		
Documentation Match to Lifecycle Needs	Very High ▼	Platform Experience	Nominal ▼	**Project**	
		Language and Toolset Experience	Nominal ▼	Use of Software Tools	Nominal ▼
				Multisite Development	Nominal ▼
				Required Development Schedule	Nominal ▼

Figure E-3: COCOMO II Inputs Assuming Software Development is Outsourced [28]

Appendix F - SPENVIS Inputs

Assigning inputs to SPENVIS may not be an intuitive process to a beginner.   The following instructions provide step-by-step guidance for conducting the analysis in section 4.6.3.

Step 1: Develop Spacecraft Trajectory

From the SPENVIS model interface, select "Coordinate generators" > "Space trajectories"
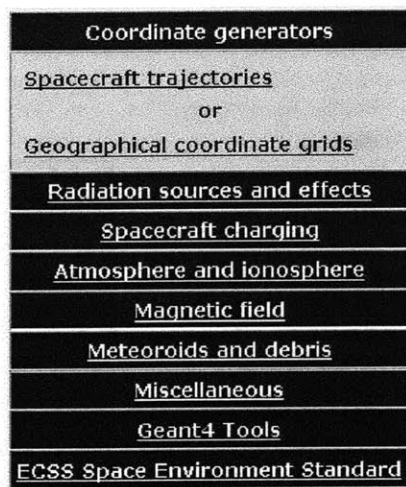
Complete the next three input windows as shown:

Hit "Run" and then select "UP" in the upper left corner.

Step 2: From the SPENVIS model interface, select "Radiation sources and effects," and complete the following input windows as shown below. After applying the entries for A and B, hit "UP" in the upper left corner of the interface. After applying the entries for C, hit "Run."

Coordinate generators
Radiation sources and effects

Radiation sources

A   Trapped proton and electron fluxes

Trapped proton flux anisotropy

B   Long-term solar particle fluences

Short-term solar particle fluxes (only for SEU)

Galactic cosmic ray fluxes

Solar cell radiation damage

Damage equivalent fluences for solar cells

NIEL based damage equivalent fluences for solar cells (MC-SCREAM)

Long-term radiation doses

Ionizing dose for simple geometries

C   Non-ionizing energy loss for simple geometries

Single event effects

LET spectra and SEU rates

Spacecraft charging
Atmosphere and ionosphere
Magnetic field
Meteoroids and debris
Miscellaneous
Geant4 Tools
ECSS Space Environment Standard

A: Trapped proton and electron fluxes.

Trapped radiation models

Proton model:	AP-8 ▾	Electron model :	AE-8 ▾
Model version:	solar minimum ▾	Model version:	solar minimum ▾
Model developed by:		Model developed by:	

NSSDC   NSSDC

Reset   Run

B: Long-term solar particle fluences.

Solar particle model:	JPL ▾
Confidence level [%]:	95.0
Magnetic shielding: no	

Reset   Run

Model developed by

JPL

C: Non-ionizing energy loss for simple geometries.

Shielding depths:	default values ▾
Damage factor [g(Si) MeV⁻¹]:	2.0E-12

Reset   Run

Tool developed by

BIRA-IASB

Step 3: After hitting run for "C," the following window will appear. Check the box next to "Summary plots…" as shown below. Then click the "Plot as" button.

Tables	Plots
Report file **Shielded proton spectra and NIEL parameters** 🖼	
New plots	
☐ Shielded fluence spectra of solar protons and trapped protons for [mission segment 1 ▾] ☑ Summary plots of NIEL, equivalent fluence and relative degradation as a function of Al shield radius	
[Plot as] Portable Network Graphics (PNG) ▾	

Step 4: After hitting the "Plot as" button, a series of plots will be listed as shown below. Select "Relative degradation (png)" to obtain the plot shown in Figure 4-11 for the 95% JPL model.

Tables	Plots
Report file **Shielded proton spectra and NIEL parameters** 🖼	**Non-ionising energy loss (png)** **Equivalent proton fluence (png)** **Relative degradation (png)**
New plots	
☐ Shielded fluence spectra of solar protons and trapped protons for [mission segment 1 ▾] ☑ Summary plots of NIEL, equivalent fluence and relative degradation as a function of Al shield radius	
[Plot as] Portable Network Graphics (PNG) ▾	

139

Appendix G - Collimator Simulation Code

```
;;;;;;;;;;;;;;;;;;;;;;;;;;;;;;;;;;;;;;;;;;;;;;;;;;;;;;;;;;;;;;;;;;;;;;;;;;;;;;;
; Filename: countbat.pro
; Filetype: .pro
; Project: REXIS  Colimator Analysis
; Author: George Sondecker (gsond@mit.edu)
; Mod Date: 2 Mar 2011
; Purpose: Builds arrays from run file outputs
; Usage: Calls: countrun.pro
;        Called From: None
;;;;;;;;;;;;;;;;;;;;;;;;;;;;;;;;;;;;;;;;;;;;;;;;;;;;;;;;;;;;;;;;;;;;;;;;;;;;;;;
; Compile countpro.pro func
.r countpro.pro

; Parameter Values
w_d = 4.92          ; detector width (cm)
w_m = w_d*2         ; mask width (cm)
dist_d2m = 25 .     ; detector to mask distance (cm)
dist_sc2ast = 700.  ; spacecraft to asteroid surface distance (m)
flux = 27.          ; detector flux (ct/sec)
dur = 21.           ; duration (earth days)

; Concentration Factor  (Select array based on plotting scenario)
;conc_arr = 10^(findgen(2000)/1000-1)     ; Use for Sigma.ps
;conc_arr = [0.1, 0.5, 1., 2., 5., 10.]   ; Use for Rad-Count.ps
conc_arr = 10^(findgen(300)/100-1)        ; Use for Conc-Count.ps

; Blob Radius (m)  (Select array based on plotting scenario)
;blob_rad_arr = findgen(2060)/10+1        ; Use for Sigma.ps
;blob_rad_arr = findgen(300)+1            ; Use for Rad-Count.ps
blob_rad_arr = [2.4, 25., 50., 100., 206., 232.]   ; Use for Conc-Count.ps

m = n_elements(conc_arr)         ; number of elements in conc array
n = n_elements(blob_rad_arr)     ; number of elements in SA_blob array
SM = 5.           ; sigma multiplier (constant)

; Compile and run the count run file
.r countrun.pro

; Save the Results

save,file='ColResults.idl'
```

```
;;;;;;;;;;;;;;;;;;;;;;;;;;;;;;;;;;;;;;;;;;;;;;;;;;;;;;;;;;;;;;;;;;;;;;;;;;;;
;;;;;;;;;;;;;;;;;;;;;;;;;;;;;;;;;;;;;;;;;;;;;;;;;;;;;
; Filename: countrun.pro
; Filetype: .pro
; Project: REXIS  Colimator Analysis
; Author: George Sondecker (gsond@mit.edu)
; Mod Date: 2 Mar 2011
; Purpose: Compiles and runs count function.
; Usage: Calls: SA.run
;       Called From: None Purpose: Compiles and runs count calculation.
; Usage: Calls: count-pro.pro
;       Called From: count-bat.pro
;;;;;;;;;;;;;;;;;;;;;;;;;;;;;;;;;;;;;;;;;;;;;;;;;;;;;;;;;;;;;;;;
;;;;;;;;;;;;;;;;;;;;;;;;;;;;;;;;;;;;;;;;;;;;;;;;;;;;;;;;;;;
; Create Arrays
ActCount_arr = fltarr(m,n) ; Actual Count (photons)
Thresh_arr = fltarr(m,n)    ; Deficit Threshold (photons)
ET_arr = intarr(m,n)        ; Detectable Deficit or Excess
                            ; Deficit = -1, Undetectable = 0, Excess = 1
Sigma_arr = fltarr(m,n)     ; Sigma Multiplier Array

; Loops to compute all concentration and blob surface areas
FOR i=0,m-1 DO BEGIN
conc = conc_arr[i]
  FOR j=0,n-1 DO BEGIN
    blob_rad = blob_rad_arr[j]
    CountOut = countpro(conc, blob_rad, w_d=w_d, w_m=w_m, dist_d2m=dist_d2m, $
          dist_sc2ast=dist_sc2ast, flux=flux, dur=dur, SM=SM)
    ActCount_arr[i,j] = CountOut[0]
    Thresh_arr[i,j] = CountOut[1]
    Sigma_arr[i,j] = CountOut[2]
    ET_arr[i,j] = CountOut[3]
    ;print,conc,SA_blob,[CountOut[0:1]/NomCount-1, CountOut]
  ENDFOR
ENDFOR

END
```

```
;:::::::::::::::::::::::::::::::::::::::::::::::::::::
;;;;;;;;;;;;;;;;;;;;;;;;;;;;;;;;;;;;;;;;;;;;;;;;;;;;;;
; Filename: countpro.pro
; Filetype: .pro
; Project: REXIS  Colimator Analysis
; Author: George Sondecker (gsond@mit.edu)
; Mod Date: 2 Mar 2011
; Purpose: Function calculates REXIS FOV and Asteroid Surface Area Coverage
; Usage: Calls: None
;       Called From: SA.run
;:::::::::::::::::::::::::::::::::::::::::::::::::::::
;;;;;;;;;;;;;;;;;;;;;;;;;;;;;;;;;;;;;;;;;;;;;;;;;;;;;;
FUNCTION countpro, conc, blob_rad, w_d=w_d, w_m=w_m, dist_d2m=dist_d2m,$
dist_sc2ast=dist_sc2ast, flux=flux, dur=dur, SM=SM

; Calculate Fully-Coded Half Angle (HA) and Field of View (FOV) (rad)
HA_full = atan(((w_m-w_d)/2.)/dist_d2m)
FOV_full = 2.*HA_full

; Calculate Full-Width-Half-Max (FWHM) Half Angle (HA) and Field of
; View (FOV) (rad)
HA_fwhm = atan((w_m/2.)/dist_d2m)
FOV_fwhm = 2.*HA_fwhm

; Calculate Full-Width-Zero Intensity (FWZI) Half Angle (HA) and Field of
; View (FOV) (rad)
HA_fwzi = atan(((w_m+w_d)/2.)/dist_d2m)
FOV_fwzi = 2.*HA_fwzi

; Calculate Surface Length (l) (m) and Surface Area (SA) (m^2) for
; Fully-Coded FOV
l_full = 2.*dist_sc2ast*tan(HA_full)
SA_full = l_full^2.

; Calculate Surface Length (l) (m) and Surface Area (SA) (m^2) for
; FWHM FOV
l_fwhm = 2.*dist_sc2ast*tan(HA_fwhm)
SA_fwhm = l_fwhm^2.

; Calculate Surface Length (l) (m) and Surface Area (SA) (m^2) for
; FWZI FOV
l_fwzi = 2.*dist_sc2ast*tan(HA_fwzi)
SA_fwzi = l_fwzi^2.

; Calculate Expected Patch Count and Std Dev assuming Poisson Distribution
dur_s = dur*24*3600                 ; duration (seconds)
dur_patch = dur_s*FOV_fwzi/(2*!pi)   ; duration at patch
NomCount = flux*dur_patch
```

```
NC_StDev = sqrt(NomCount)

; Calculate Reflected Flux per Square Meter as seen by the Detector
unit_flux = flux/SA_fwzi           ; ct/(sec*m^2)

; Calculate Excess and Deficit
IF conc GE 1. THEN BEGIN                              ;Excess
  ActCount = unit_flux*(SA_fwzi+!pi*blob_rad^2*(conc-1))*dur_patch    ;Count
  ;AC_StDev = sqrt(ActCount)                          ;Std Dev
  Thresh = NomCount+SM*NC_StDev                           ;Threshold
  Sigma = (ActCount-NomCount)/NC_StDev                      ;Sigma
    IF ActCount GE Thresh THEN BEGIN
      ET = 1              ; EXCESS
    ENDIF ELSE BEGIN
      ET = 0              ; EXCESS,but does not exceed threshold.
    ENDELSE
ENDIF ELSE BEGIN                                      ;Deficit
  ActCount = unit_flux*(SA_fwzi-!pi*blob_rad^2*(1-conc))*dur_patch    ;Count
  ActCount = ActCount>0.                             ;Make Positive.
  ;AC_StDev = sqrt(ActCount)                          ;Std Dev
  Thresh = NomCount-SM*NC_StDev                           ;Threshold
  Sigma = (NomCount-ActCount)/NC_StDev                      ;Sigma
    IF ActCount LE Thresh THEN BEGIN
      ET = -1             ; DEFICIT
    ENDIF ELSE BEGIN
      ET = 0              ; DEFICIT, but does not exceed threshold.
    ENDELSE
ENDELSE

; Return Values of Interest
RETURN,[ActCount, Thresh, Sigma, ET]

END
```

```
;;;;;;;;;;;;;;;;;;;;;;;;;;;;;;;;;;;;;;;;;;;;;;;;;;;;;;;;;;
; Filename: plotbat.pro
; Filetype: .pro
; Project: REXIS  Colimator Analysis
; Author: George Sondecker (gsond@mit.edu)
; Mod Date:  2 Mar 2011
; Purpose: Builds arrays from run file outputs
; Usage: Calls: deviceps
;       Called From: None
;;;;;;;;;;;;;;;;;;;;;;;;;;;;;;;;;;;;;;;;;;;;;;;;;;;;;;;;;
; Save the Results
restore,'ColResults.idl'

; ps mode
@ps

; Initialize Color Palette
loadct,39 ; rainbow

; Create Plot of Blob Radius vs Actual Count at discrete concentrations
deviceps, file='Rad-Count.ps'
plot, blob_rad_arr, /YLOG, ActCount_arr[2.,*], $
    XTIT = 'Blob Radius (m)',$
    YTIT = 'Expected Count (counts)',$
    XRANGE = [min(blob_rad_arr), max(blob_rad_arr)],$
    ;YRANGE = [min(ActCount_arr), max(ActCount_arr)],$
    YRANGE = [10.^5., 10.^8.],$
    line=0, col=1

oplot, blob_rad_arr, ActCount_arr[0.,*], line=1, col=200
oplot, blob_rad_arr, ActCount_arr[1.,*], line=2, col=165
oplot, blob_rad_arr, ActCount_arr[3.,*], line=3, col=100
oplot, blob_rad_arr, ActCount_arr[4.,*], line=4, col=50
oplot, blob_rad_arr, ActCount_arr[5.,*], line=5, col=250
legend,['conc=10', 'conc=5', 'conc=2', 'conc=1', 'conc=0.5', 'conc=0.1'],$
line=[5,4,3,0,2,1], textcol=[1,1,1,1,1,1], col=[250,50,100,1,165,200]

; Create Plot of Concentration vs Actual Count at discrete blob radii(m)
deviceps, file='Conc-Count.ps'
plot, /XLOG, conc_arr, /YLOG, ActCount_arr[*, 0.],$
    XTIT = 'Concentration (unitless)',$
    YTIT = 'Expected Count (counts)',$
    XRANGE = [min(conc_arr), max(conc_arr)],$
    YRANGE = [min(ActCount_arr), max(ActCount_arr)],$
    line=0, col=1
```

```
oplot, conc_arr, ActCount_arr[*, 1.],line=1, col=200
oplot, conc_arr, ActCount_arr[*, 2.],line=2, col=165
oplot, conc_arr, ActCount_arr[*, 3.],line=3, col=100
oplot, conc_arr, ActCount_arr[*, 4.],line=4, col=50
oplot, conc_arr, ActCount_arr[*, 5.],line=5, col=250
legend, ['Blob Radius = 232m',$
     'Blob Radius = 206m',$
     'Blob Radius = 100m',$
     'Blob Radius = 50m',$
     'Blob Radius = 25m',$
     'Blob Radius = 2.4m'],$
     line=[5,4,3,2,1,0],textcol=[1,1,1,1,1,1],col=[250,50,100,165,200,1]

; Create Sigma Plot
deviceps, file='Sigma.ps'
cm_tickn=['0','1','2','5','10','100']
cm_tickv=[0,1,2,5,10,100]

tvplot,$
     alog(transpose(sigma_arr)<100.+1),$
     xtit='Blob Radius (m)',ytit='Concentration (unitless)',$
     xr=[min(blob_rad_arr),max(blob_rad_arr)],xty=0,$
     yr=[0.1,10.1],yty=1,$
     cmap=[0.01,0.03,0.03,0.35], dir=4, $
     cm_tickn=cm_tickn, $
     cm_tickv=alog(cm_tickv+1.), $
     col=0,/noinvertps

; Create Plot of Actual Count (5 sigma) as a function of Blob Radius
; and Concentration

deviceps, file='Rad-Conc-5s.ps'
loadct,39 ; load color scale (rainbow)
tvplot,$
     transpose(et_arr),$
     xtit='Blob Radius (m)',ytit='Concentration (unitless)',$
     xr=[min(blob_rad_arr),max(blob_rad_arr)],xty=0,$
     yr=[0.1,10.1],yty=1,$
     col=0,/noinvertps

; Close deviceps
deviceps,/close
```
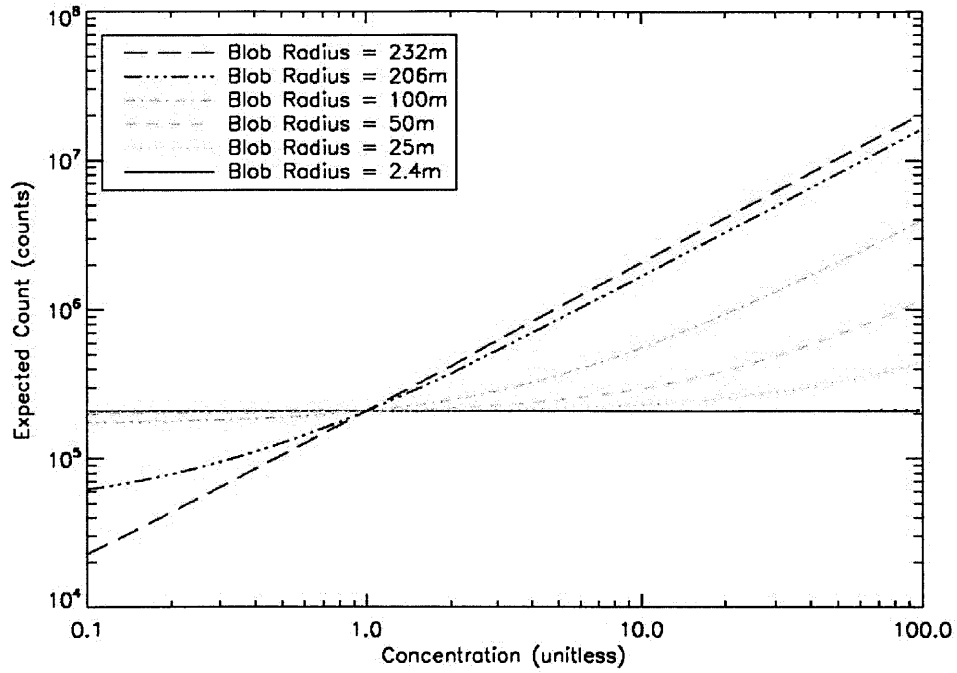
Appendix H - Collimator Simulation Results

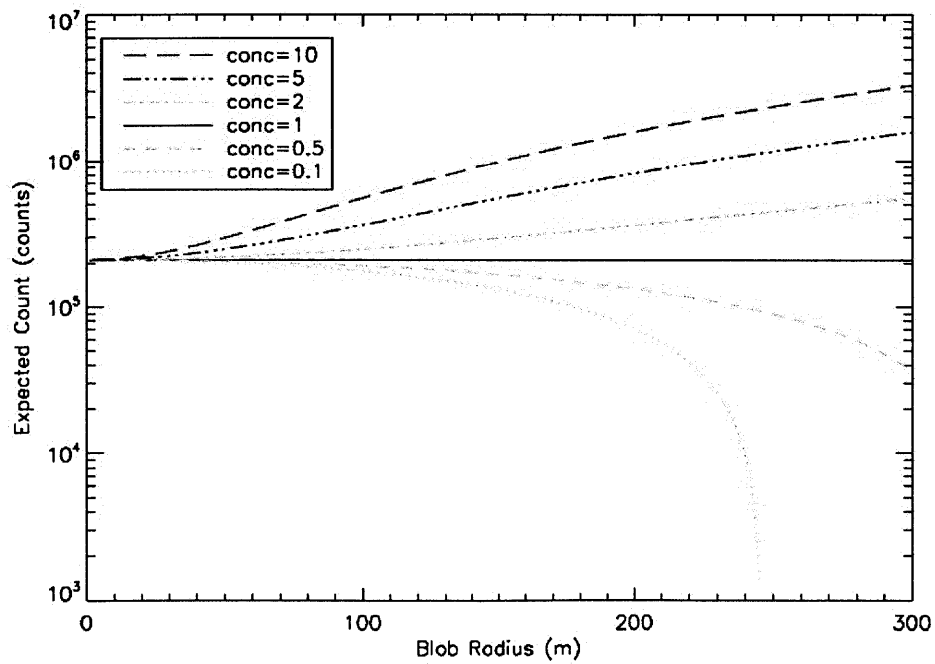Figure H-1: Expected Number of Counts at Detector for Various Concentrations of Iron

Figure H-2: Expected Number of Counts at Detector for Various Blob Sizes of Iron
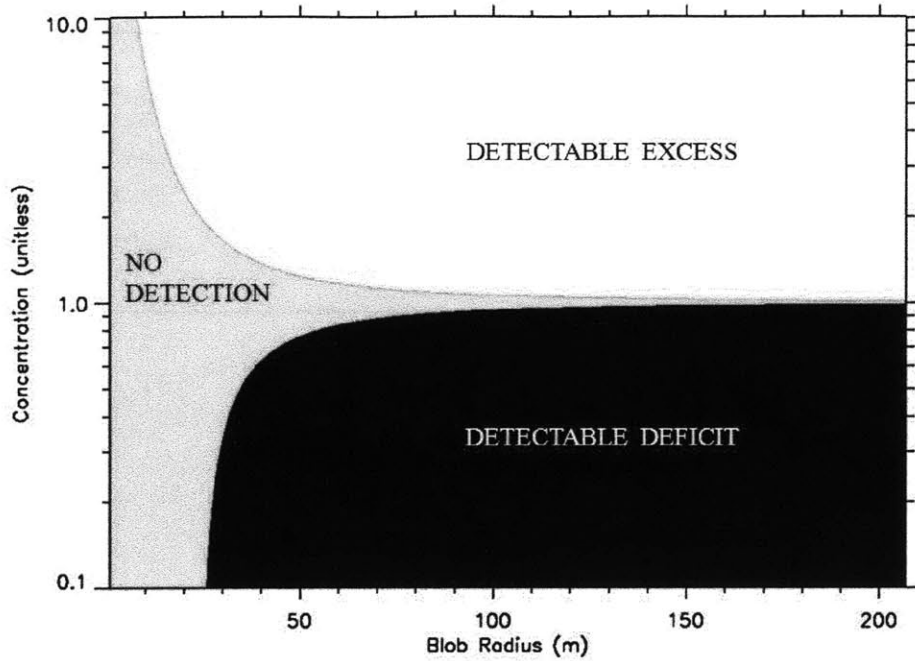
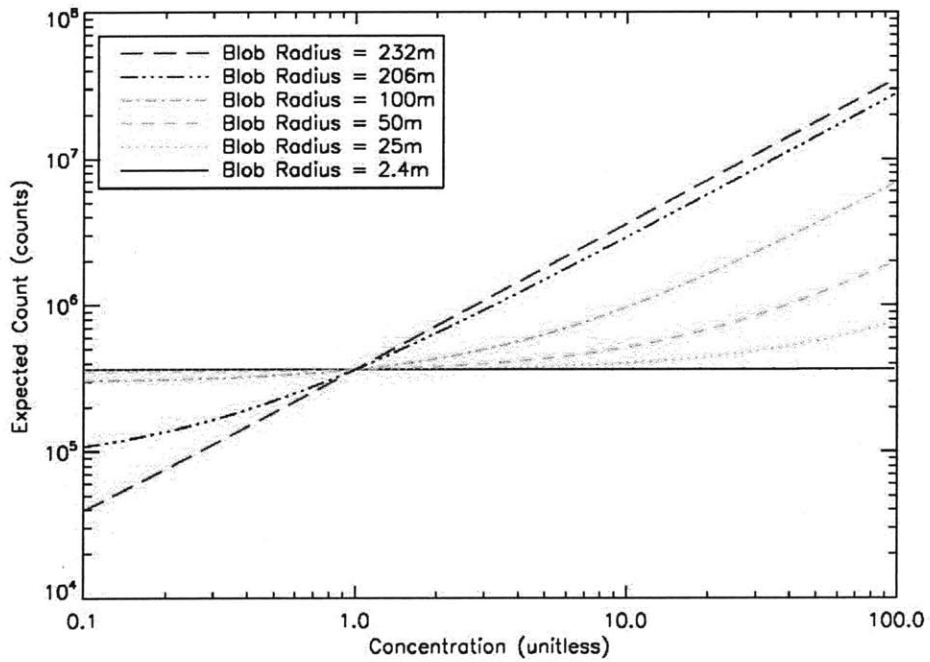Figure H-3: Detection of Iron at 5σ Confidence

Figure H-4: Expected Number of Counts at Detector for Various Concentrations of Magnesium
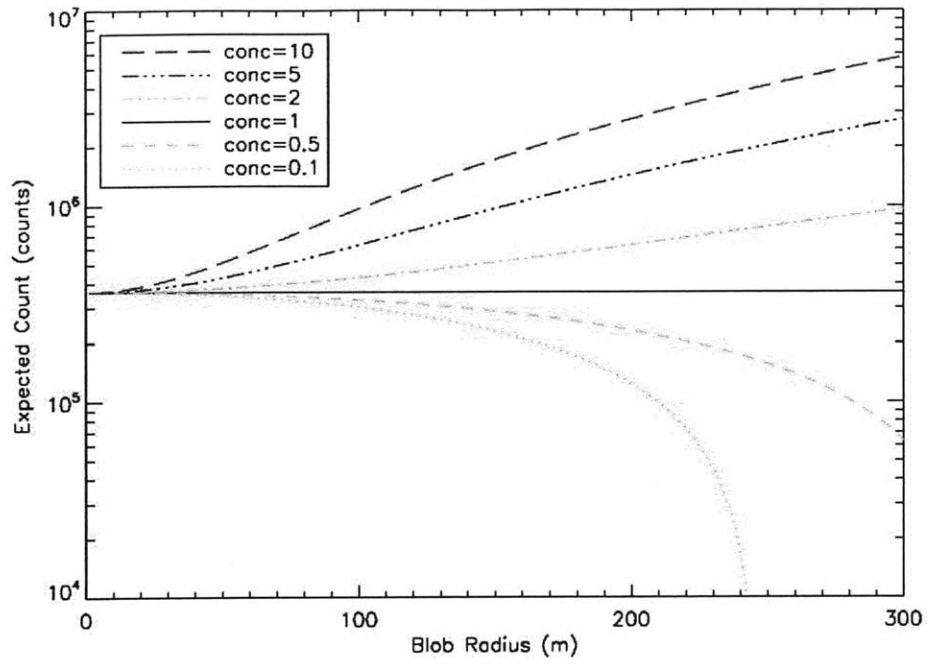
Figure H-5: Expected Number of Counts at Detector for Various Blob Sizes of Magnesium
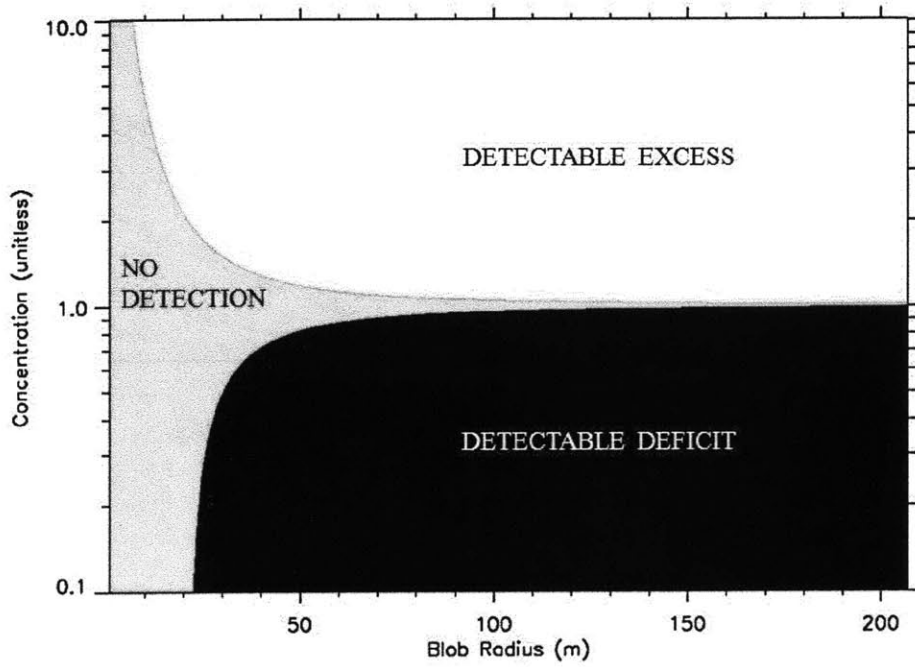

Figure H-6: Detection of Magnesium at 5σ Confidence

148

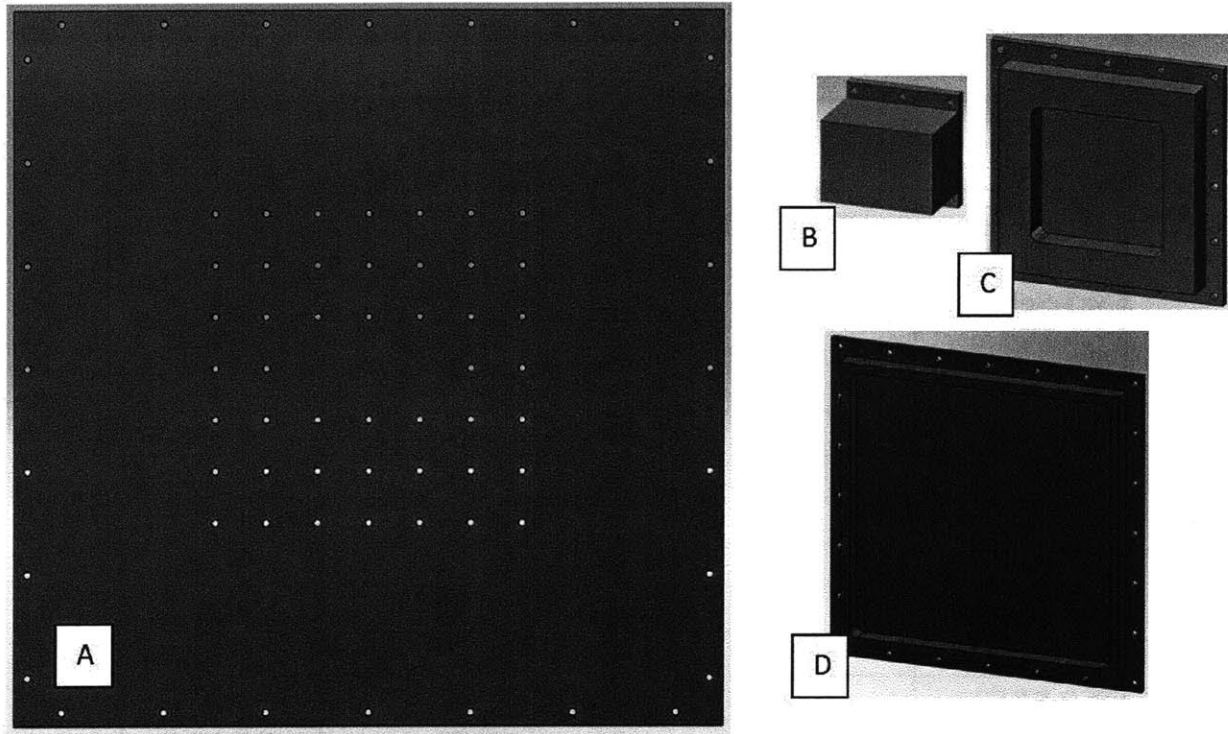# Appendix I - Panel and Box CAD

Figure I-1: Panel and Boxes- (A) 20in x 20in panel, (B) 3in x 3in box, (C) 6in x 6in box, (D) 9in x 9in Box

Appendix J - Model Verification Results

Table J-1: SPC Check Results

Model	Actual Weight (lb)	Model Weight (lb)	% Diff (%)
Panel	5.033	5.007	0.52
Smeared	7.485	7.459	0.35
CONM	7.485	7.459	0.35
3x3-RBE2	7.358	7.332	0.35
3x3-RBE3	7.358	7.332	0.35
3x3-Solid	7.358	7.332	0.35
3x3-CBUSH	7.358	7.332	0.35
3x3-Extrude	7.358	7.332	0.35
6x6-RBE2	7.485	7.457	0.37
6x6-RBE3	7.485	7.457	0.37
6x6-Solid	7.485	7.457	0.37
6x6-CBUSH	7.485	7.457	0.37
6x6-Extrude	7.485	7.457	0.37
9x9-RBE2	7.610	7.582	0.37
9x9-RBE3	7.610	7.582	0.37
9x9-Solid	7.610	7.591	0.25
9x9-CBUSH	7.610	7.591	0.25
9x9-Extrude	7.610	7.582	0.37

Conclusion: Since the difference between the actual and model weights is less than 1%, the SPC check is satisfied for all cases.

Appendix K - Comparison between Analytical and Numerical FNF Predictions

This appendix illustrates the application of analytical solution techniques to calculate panel FNF, and compares the analytical results to numerical results for model verification.

Simply Supported Panel:

$$f_n(c,d) = \frac{\pi}{2}\left[\left(\frac{c}{a}\right)^2 + \left(\frac{d}{b}\right)^2\right]\sqrt{\frac{D}{\gamma}}$$

$$c = d = 1$$

$$a = b = 20in$$

$$D = \frac{Et^3}{12(1-v^2)} = 1521\ lb * in$$

$$E = 9.9E6\ psi$$

$$t = 0.118\ in$$

$$v = 0.33$$

$$\gamma = \gamma_{Panel} = \frac{5.033lb}{\left(386.1\frac{in}{s^2}\right)(20.8in \times 20.8in)} = 3.01E - 5\frac{lb*s^2}{in^3}$$

$$f_n(c,d) = 55.8\ Hz$$

Note: a=b=20in is used to define the boundary condition formed by the perimeter of fasteners. When calculating the panel mass per unit area, the panel mass is divided over the actual 20.8in x 20.8in panel.

Simply Supported Panel with Smeared Mass for 6in x 6in Box

$$f_n(c,d) = \frac{\pi}{2}\left[\left(\frac{c}{a}\right)^2 + \left(\frac{d}{b}\right)^2\right]\sqrt{\frac{D}{\gamma}}$$

Inputs same as Simply Supported except:

$$\gamma = \gamma_{Total} = \gamma_{Panel} + \gamma_{Component}$$

$$\gamma = \frac{5.033lb}{\left(386.1\frac{in}{s^2}\right)(20.8in \times 20.8in)} + \frac{2.452lb}{\left(386.1\frac{in}{s^2}\right)(20in \times 20in)} = 4.60E - 5\frac{lb*s^2}{in^3}$$

$$f_n(c,d) = 45.8\ Hz$$

Clamped Panel

$$f_n(c,d) = \frac{\lambda_{cd}^2}{2\pi a^2}\sqrt{\frac{D}{\gamma}}$$

Inputs same as Simply Supported

$$\lambda_{cd}^2 = 35.99\ for\ \frac{a}{b} = 1$$

$$f_n(c,d) = 102\ Hz$$

Table K-1: Comparison of Analytical and Numerical Solutions

Boundary Condition	Analytical FNF (Hz)	Numerical FNF (Hz)	% Diff (%)
Simp Sup Panel	55.8	57.4	2.9
Simp Sup Panel, 3in x 3in Box Smeared	45.6	47.4	3.9
Simp Sup Panel, 6in x 6in Box Smeared	45.2	47.0	4.0
Simp Sup Panel, 9in x 9in Box Smeared	44.8	46.6	4.0
Clamped Panel	102	102	0.0
Clamped Panel, 3in x 3in Box Smeared	83.1	84.4	1.6
Clamped Panel, 6in x 6in Box Smeared	82.3	83.7	1.7
Clamped Panel, 9in x 9in Box Smeared	81.6	83.0	1.7

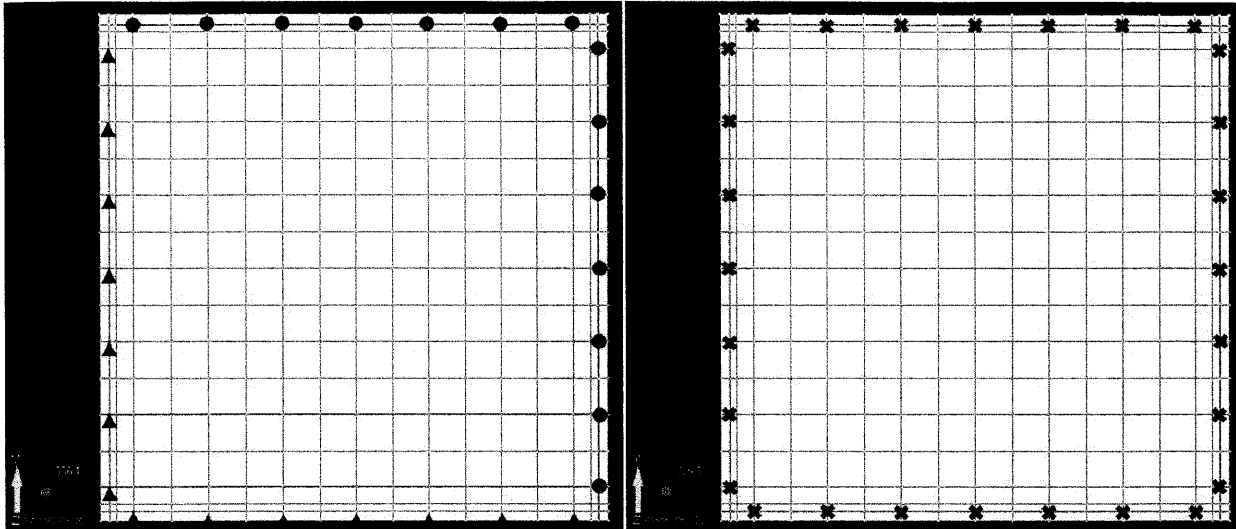# Appendix L - Trade Study Boundary Conditions

Figure L-1: Fastener Boundary Conditions. LEFT: Simply Supported Fasteners. The simply-supported boundary condition is formed using pins (red triangles) and rollers (red circles) at fastener locations along the perimeter of the panel. The pins along the Y-axis constrain translation in the X- and Z-directions. The pins along the X-axis constrain translation in the Y- and Z-directions. The rollers constrain translation in the Z-direction. RIGHT: Clamped Fasteners. The clamped boundary condition is by constraining translation and rotation the nodes at fastener locations in translation and rotation in the X-, Y-, and Z-directions (red X's).
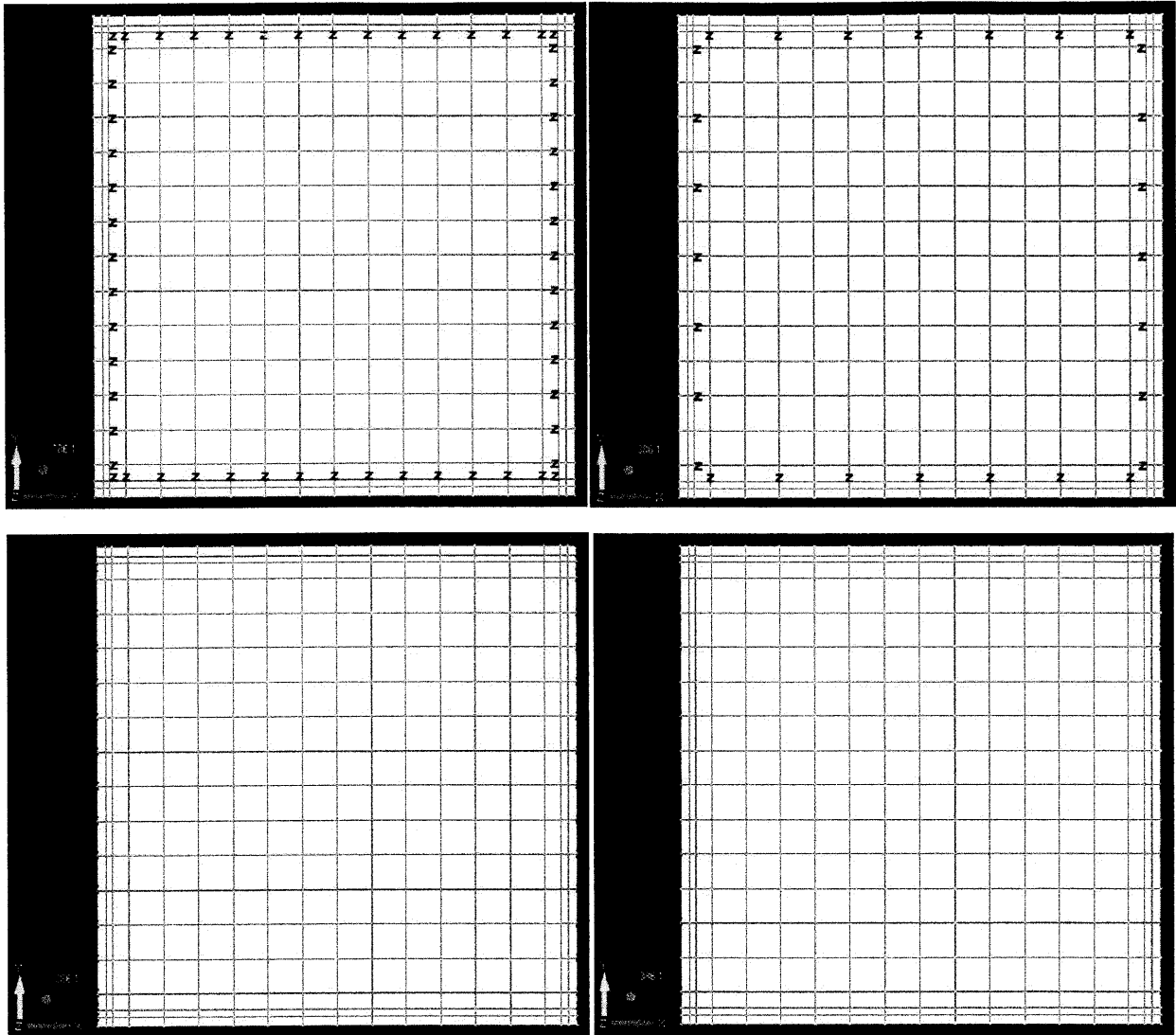
Figure L-2: Boundary Conditions applied along the Inner- and Outer-Perimeter of the Test Frame. These boundary conditions are imposed to account for interactions between the panel and test frame. TOP: Translation along the Z-axis (red Z's) is constrained at *all* nodes (LEFT) and at *alternating* nodes adjacent to fasteners (RIGHT) along the test frame's inner-perimeter. BOTTOM: Translation along the Z-axis (red Z's) is constrained at *all* nodes (LEFT) and at *alternating* nodes adjacent to fasteners (RIGHT) along the test frame's outer-perimeter.